Title
Leveraging variation in genetically diverse mouse strains to study Metabolic Syndrome phenotypes

Author
Swichkow, Chantle Reiko Alvarado

Publication Date
2021

Peer reviewed|Thesis/dissertation

UNIVERSITY OF CALIFORNIA

Los Angeles

Leveraging variation in genetically diverse mouse strains to study Metabolic Syndrome phenotypes: genetic and genomic analyses in the Hybrid Mouse Diversity Panel

A dissertation submitted in partial satisfaction of the

requirements for the degree Doctor of Philosophy

in Human Genetics

by

Chantle Reiko Alvarado Swichkow

2021

ABSTRACT OF THE DISSERTATION

Leveraging variation in genetically diverse mouse strains to study Metabolic Syndrome phenotypes: genetic and genomic analyses in the Hybrid Mouse Diversity Panel

by

Chantle Reiko Alvarado Swichkow

Doctor of Philosophy in Human Genetics

University of California, Los Angeles, 2021

Professor Aldons Jake Lusis, Co-Chair

Professor Matteo Pellegrini, Co-Chair

The Hybrid Mouse Diversity Panel (HMDP) is a systems genetic resource of over one hundred different mouse strains. The genetic variation and subsequent phenotypic variation between strains in the HMDP encompass a spectrum of metabolic phenotypes from weight gain following a high-fat diet to susceptibility to heart and liver disease. My dissertation research focuses on the analysis of genetic and genomic data originating from multiple HMDP studies for Metabolic Syndrome phenotypes. Firstly, I identified DNA methylation patterns associated with diet-induced obesity that were observed across diverse genetic backgrounds. I then asked whether these epigenetic changes were maintained following weight loss in a subset of strains. Secondly, I characterized novel genes for atherosclerosis, *Nnmt*, *Csf1,* and *Zhx2*. Lastly, I used transcriptional approaches with genetically diverse mouse strains to identify susceptibility mechanisms involved in the development of progressive liver disease phenotypes. Taken

together, this body of research encompasses genetic, cell-type, gene expression, and epigenetic approaches to investigate mechanisms involved in obesity, heart, and liver disease.

The dissertation of Chantle Reiko Alvarado Swichkow is approved.

Jeanette Christine Papp

Karen Reue

Aldons Jake Lusis, Committee Co-Chair

Matteo Pellegrini, Committee Co-Chair

University of California, Los Angeles

2021

DEDICATION

To my inner child and my future self.

TABLE OF CONTENTS

LIST OF FIGURES

LIST OF TABLES

ACKNOWLEDGEMENTS

First, I want to thank my personal support team: my PhD sisters Malika Freund and Jazlyn Mooney; my dear friends John Paul Peralta, Emily Hsu, Rob Brekelmans, Jennifer Lang, Jessica Ong, Ellie Taus, Christina Ritchey, James Ward, Taylor Brown; my family Rico Edillor, Bennice Edillor, Jared Edillor, Nicetas Alvarado, Ron Swichkow, Leslie Swichkow, Erin Cooper, Seth Cooper, Ellie Cooper, Avery Cooper, Alvin Hodes; my community, Fermenters Anonymous, Reddit. This work would not have been possible, or meaningful, if not for you.

Next, I would like to acknowledge my advisors Matteo Pellegrini and Jake Lusis, whose support, patient teaching, encouragement, and faith in me has pushed me forward every year, thank you. I would also like to thank Evan Muse and Chris Glass, my mentors who dedicated the time and to prepare me for the rigors of graduate school. The other members of my committee Karen Reue and Jeanette Papp who have given me their insightful feedback and words of support. I next wish to acknowledge my collaborators, lab mates, and colleagues who have helped guide me through my research and this PhD. In particular, from the Lusis and Pellegrini Labs past and present: Tim Moore, Milagros Romay, Simon Hui, Sunny Chang, Jessica Rahman, Karthick Chella Krishnan, Marco Morselli, Dorota Kaminska, Calvin Pan, Margarete Mehrabian, Jennifer Lang, William Barrington, Sarada Charugundla, Diana Shih, Brie Fuqua, Nam Che, Frode Norheim, Marcus Seldin, Mete Civelek, Brian Parks, Casey Romanoski; from UCLA:, Kelsey Jarrett, Xia Yang, Simon Beaven, Luisa Aurela Irispe, Julia Mack. Last, but not least, I want to acknowledge my husband, Brian Swichkow. Thank you for making space for me to do the work and joyfully explore.

VITA

EDUCATION

2021 PhD Candidate, Human Genetics
University of California, Los Angeles | Los Angeles, CA

2013 Bachelor of Science, Developmental and Cell Biology
University of California, Irvine | Irvine, CA

PEER-REVIEWED PUBLICATIONS

Edillor, C. R., Parks, B. W., Mehrabian, M., Lusis, A. J., & Pellegrini, M. (2019). DNA methylation changes more slowly than physiological states in response to weight loss in genetically diverse mouse strains. *Frontiers in endocrinology*, *10*, 882.

Sinha, S. K., Miikeda, A., Fouladian, Z., Mehrabian, M., **Edillor, C.**, Shih, D., ... & Lusis, A. J. (2021). Local M-CSF (macrophage colony-stimulating factor) expression regulates macrophage proliferation and apoptosis in atherosclerosis. *Arteriosclerosis, Thrombosis, and Vascular Biology*, *41*(1), 220-233.

Orozco, L. D., Farrell, C., Hale, C., Rubbi, L., Rinaldi, A., Civelek, M., Pan C., Lam L., Montoya D., **Edillor C**., ...& Pellegrini, M. (2018). Epigenome-wide association in adipose tissue from the METSIM cohort. *Human molecular genetics*, *27*(10), 1830-1846.

Chapter 1: Introduction

My dissertation research focused on analyzing genetic and genomic data from the Hybrid Mouse Diversity Panel (HMDP), a systems genetics resource of about one hundred diverse inbred mouse strains developed for the analysis of complex traits. The HMDP has been used for studies of a wide spectrum of cardiometabolic traits such as diet-induced obesity, non-alcoholic fatty liver disease, and atherosclerosis. The chapters of this dissertation include three related projects focused on understanding aspects of Metabolic Syndrome and pathologies associated with chronic metabolic dysregulation like atherosclerosis and non-alcoholic fatty liver disease. Metabolic Syndrome is a collection of multi-organ phenotypes originating from dysregulated metabolic processes. Metabolic Syndrome is defined by impaired glucose tolerance, insulin resistance, obesity, dyslipidemia, and hypertension, which can increase an individual's risk for cardiovascular disease. The basis for this dysregulation is both genetic and lifestyle/environmental. Within the last decades, genome-wide association studies (GWAS) in large-scale human populations have been conducted to identify the genetic basis of such metabolic susceptibility. Due to the variability in human lifestyles and diets, such studies often pose difficulties in identifying and testing causal mechanisms. In addition, the collection of relevant tissues for analysis, particularly for metabolic organs like the liver, can be difficult to obtain. The Lusis lab established the HMDP to leverage the conserved metabolic processes between mice and humans with the added benefit of greater accessibility to various tissues and the ability to collect biological replicates within genetically identical mice. The HMDP is a parallel approach of such studies using diverse mouse genetic variation while controlling for environmental factors like diet to identify genes involved in the susceptibility to Metabolic Syndrome phenotypes.

To induce metabolic dysregulation, the HMDP can be subjected to a dietary challenge over the course of 8 to 16 weeks, depending on the phenotype. To study obesity phenotypes, the HMDP was fed a high-fat, high-sucrose diet (32.5% fat, 25% sucrose) for 8 weeks (Parks et al, 2013;2015). This diet subsequently increased adiposity and reduced glucose tolerance traits to varying degrees across the panel of 100+ strains. To study cardiovascular disease and atherosclerosis, Bennett et al, (2015) bred the HMDP onto a humanized hyperlipidemic genetic background. Sixteen weeks of a high-fat, high-cholesterol diet (33% fat, 1% cholesterol) in conjunction with the hyperlipidemic transgene induced significant plaque development in the aorta. It was discovered that the conditions to induce atherosclerosis in the HMDP also led to the development of progressive liver disease phenotypes such as non-alcoholic steatohepatitis and fibrosis. From these studies my dissertation work investigates mechanisms in the liver from the obesity and atherosclerosis HMDP studies related to genetic and epigenetic susceptibility to metabolic dysregulation.

Responses to a high fat, high sucrose (HFHS) diet vary greatly among inbred strains of mice. In **Chapter Two,** I examined DNA methylation changes underlying these differences in diet-induced obesity and weight loss. Using reduced representation bisulfite sequencing, I surveyed CpG methylation from the livers of 45 HMDP strains fed either a low-fat chow diet (18% fat) or an obesifying high-fat, high-sucrose diet. I observed over a million CpGs, of which 83 candidate sites were significantly associated with obesity. Many CpGs correlated strongly with gene expression or clinical traits such as body fat percentage and plasma glucose. Five variable inbred strains were then studied in the context of weight loss to test for evidence of epigenetic "memory." The mice were first fed a HFHS diet for six weeks, followed by a low-fat chow diet for four weeks. Four of the five strains returned to initial body fat levels, while one

strain, A/J, retained almost 50% of the fat gained. A total of 36 HFHS-diet-responsive CpGs exhibited persistent epigenetic modifications following weight normalization, including CpGs near the genes *Scd1* and *Cdk1*. This research has showed that DNA methylation marks responsive to a HFHS diet change more slowly than overall body fat percentage in weight loss, providing evidence for epigenetic mediated "memory." A version of this work has been published in Frontiers in Endocrinology as:

Edillor, C. R., Parks, B. W., Mehrabian, M., Lusis, A. J., & Pellegrini, M. (2019). DNA methylation changes more slowly than physiological states in response to weight loss in genetically diverse mouse strains. *Frontiers in endocrinology*, *10*, 882.

Our lab has also used the HMDP to study atherosclerosis. A GWAS analysis of the HMDP identified N-nicotinamide methyltransferase, *Nnmt*, as a potential candidate gene for atherosclerosis. **Chapter Three** focuses on the validation of *Nnmt* as a casual gene and analysis of the molecular mechanisms underlying its effect on atherosclerosis. NNMT is a methyltransferase with known effects on lipid metabolism and diet-induced obesity. Our studies showed that whole-body knockdown of *Nnmt* expression by an antisense oligonucleotide (ASO) reduced atherosclerosis lesion area 10-fold in mice on a hyperlipidemic background. *Nnmt* is most highly expressed in metabolic tissues such as adipose and liver, but AAV-mediated tissue-specific knockdown in either tissue was not causal for atherosclerosis nor did result in the dramatic reduction in lesion area. My recent studies suggest that the effects of *Nnmt* knockdown are systemic, influencing not only the circulating levels of lipids and metabolites but also local metabolism in cells and tissues relevant to atherosclerosis.

In **Chapter Four**, I used genetically susceptible and resistant inbred mouse strains of nonalcoholic fatty liver disease (NAFLD) to identify genetic and cell-type composition changes

associated with disease progression. NAFLD is the most common chronic liver disorder in humans, characterized by an accumulation of fat in the liver, hepatocyte ballooning, cell death, scarring, and inflammation. The pathology of NAFLD is heterogenous and highly influenced by environmental factors, particularly diet. In this study I used bulk- and single-cell RNA sequencing to identify differentially regulated gene expression pathways and progressive cellular changes associated with inflammatory and fibrotic liver phenotypes.

In **Chapter Five**, I will summarize my results, highlight key understandings, and discuss the implications of my work in the context of human health.

Chapter 2: DNA Methylation Changes More Slowly Than Physiological States in Response to Weight Loss in Genetically Diverse Mouse Strains

Introduction

Epigenetic regulation, such as DNA methylation, was hypothesized and recently confirmed to play a role in the development of obesity in humans and rodents [1]. The interactions between diet, genetic background, and epigenetic regulation are becoming better understood, with evidence suggesting that DNA methylation can be a causal factor in obesity [2]. In rodents (where the effect of environment is more controlled), studies have identified specific DNA methylation changes in the liver at genes involved in metabolism (*Scd1*, *GK/glycerol kinase*, *L-PK/L-pyruvate kinase*, *Mttp*) as well as cell-cycle regulation (*Cdkn1a)* [3-6]. Additional evidence suggests that human DNA methylation changed by obesity can be remodeled by interventions like bariatric surgery by improving metabolic parameters such as hepatic insulin resistance. Caloric restriction in humans and mice protects against aging associated pathologies like type 2 diabetes, heart disease, and hepatocellular carcinoma, while obesity increases this susceptibility [7-9]. These changes are known to be mediated in part by DNA methylation, a biomarker reproducibly associated with chronological aging. These variable epigenetic loci are often used to fit tissue-specific biological clocks of "epigenetic aging" in association with biometrics like body mass index (BMI) [10]. Obesity-associated DNA methylation changes have also been observed to accelerate "epigenetic aging" in the liver and are not acutely reversible by interventions like bariatric surgery [10-12].

A clinically relevant aspect of such studies relates to the context of weight loss and whether the effects of dietary challenge and obesity remain. In human surveys of DNA

methylation during weight loss, it was observed that modest but widespread changes to DNA methylation were found near known obesity and diabetes genes in liver and adipose [13]. Other studies identified DNA methylation differences near known obesity genes predicting high or low responses to therapies like caloric restriction, exercise, or surgical interventions [14-21]. It has been hypothesized that these methylation changes may be involved in a "memory" mechanism of weight-regain or persistent accelerated epigenetic aging after weight loss [22]. Studying chromatin accessibility using FAIRE-seq in a mouse model of diet-induced obesity, Leung and colleagues observed strain specific evidence for "memory" using a weight loss study design [23]. On the other hand, Siersbaek and colleagues found no evidence for epigenetic memory following 8 weeks of weight loss as assessed by H3K27Ac marks [24].

Here, we surveyed a large panel of genetically diverse inbred strains of mice previously shown to vary in response to a high-fat, high-sucrose (HFHS) diet using reduced-representation bisulfite sequencing (RRBS). We previously profiled the methylomes of over 100 strains on a chow diet to identify genetic variation influencing liver DNA methylation [25]. To study the effect of diet on liver methylation patterns, we performed RRBS in a subset of strains after 8 weeks of obesity. The liver is a relevant tissue in obesity studies as it coordinates with adipose tissue to regulate glucose, insulin, and lipid levels. In human studies of epigenetic aging across various tissues, only the liver showed a significant correlation between accelerated epigenetic aging and BMI [10]. Our analysis resulted in the identification of 83 CpGs corresponding to 62 loci exhibiting significant changes in methylation in a majority of strains in response to diet. We then asked how these sites respond to a reversion to a low fat chow diet and whether they maintain the "memory" of the HFHS diet state despite weight loss.

Materials and Methods

Animals and experimental design

A genetic study of diet-induced obesity was previously reported, where 100 diverse inbred mouse strains of both sexes were fed a high-fat (32.5% kcal from corn oil and butter), high-sucrose (25% kcal) diet for 8 weeks [26]. We refer to this collection of strains as the Hybrid Mouse Diversity Panel (HMDP). A subset of 45 strains from this study were selected based on the availability of age-matched males of the same strain fed a chow-only (18% kcal from fats) diet for 8 weeks. All mice were obtained from the Jackson Laboratory and the animal protocol for the study was approved by the Institutional Care and Use Committee (IACUC) at University of California, Los Angeles. The HFHS diet was purchased from Research Diets (D12266B).
A subset of 5 HMDP strains (A/J, BALB/cJ, C3H/HeJ, C57BL/6J, and DBA/2J) was used as a validation and weight loss discovery cohort. These strains were selected in order to study the variability in weight loss phenotypes based on their body fat responses to HFHS diet. BALB/cJ was found to be a low responding strain in terms of body fat gain, A/J, C57BL/6J, and C3H/HeJ responding moderately, and DBA/2J animals with the greatest response to 8 weeks of HFHS diet [26]. Animals from all 5 strains were fed either HFHS (n = 16/strain) or chow (n= 8/strain) diets for 6 weeks. Half of the HFHS group was then returned to chow for 4 weeks and treated as a weight loss phenotype (n = 8/strain), while the remaining animals remained on chow- or HFHS-only diets. In both the obesity and weight loss studies, body composition was measured bi-weekly throughout the course of the diet via NMR. At the time of sacrifice, metabolic phenotypes such as glucose tolerance, serum insulin, and lipids were measured. The log-value of these clinical measurements were used for correlation analyses with methylation changes.

Liver methylome profiling and differential methylation analysis

We isolated genomic DNA from 30-50mg of whole liver from 16-week old animals fed chow or HFHS diet. For each of the 45 strains, DNA from 2-3 males per strain was pooled for library preparation, producing epigenetic profiles that represent the aggregate methylation profiles for a strain. Genomic DNA was isolated using the Qiagen AllPrep DNA/RNA Mini Kit. When anatomy of the frozen tissue was discernible, 30-50mg samples were cut from the middle of the left caudate lobe. Tissues were homogenized in RLT Plus Buffer in a Qiagen TissueLyser at 50Hz for 2 minutes. DNA concentrations were measured using the Qubit fluorometer with the DS DNA kit. RRBS libraries were prepared according to previously published protocols [8]. We initially combined and sequenced the genomic DNA of 2-3 animals for the initial set of 45 HMDP libraries and sequenced 3 individual animals per diet in the weight loss cohort. One-hundred ng of genomic DNA was digested with the methylation-insensitive restriction enzyme MspI, and fragments of length from 50 to 400bp were selected. We sequenced each library to an average depth of 20 million reads per sample on the Illumina HiSeq4000 platform. Sequencing reads were mapped to mouse genome build mm10 using an RRBS specific aligner, BSSeeker2 [27]. We observed 45% mappability across all samples. CpGs on opposite strands were not merged and maintained as separate sites. We filtered the cytosines based on CG context, coverage, and representation across all samples. This yielded > 1 million CpGs with 10x coverage across at least 70% of samples. CG-SNPs, where one allele of a genetic variant is also a CpG site, were removed. CG-SNPs were identified by cross referencing profiled CpGs with HMDP SNPs imputed by Bennett et al. [28]. For each remaining CpG site with 10x or greater coverage, the methylation level was calculated by computing the ratio of methylated to unmethylated reads at each site. This proportion represents the percentage of cells in the sampled

tissue with a methylated cytosine. We removed CpGs with low variance (row variance < 0.01) across all strains and diets. For each CpG site in the dataset we first calculated the intra-strain change in methylation between HFHS and chow diets. We compared the means at each site between diets using a two-tailed paired T-test. To account for multiple comparisons, we calculated a Benjamini-Hochberg corrected FDR-adjusted p-value. FDR-significant sites had a differential FDR $\leq$ 0.1 which corresponded to an unadjusted p-value of 5E-5. We permuted the diet labels and performed 1000 permutations at every analyzed CpG.

Genomic and Functional Annotation

Significant CpGs were annotated to nearby genes using GREAT [29]. Annotated regions correspond to 1000kb surrounding a gene's TSS. Once annotated, GREAT performs pathway enrichment using GO and KEGG terms. A set of 100,000 randomly selected CpGs were selected from the data as background for enrichment.

Statistical Analyses

All statistical analyses were performed using the Python 3.0 packages Pandas and NumPy for processing DataFrames , and Scipy Stats for statistical test functions like t-tests, FDR corrections, permutation, and calculating correlation coefficients. values reported are Pearson's coefficient. Phenotypes are log-normalized.

Results

Diet-responsive methylation changes in a subset of the HMDP

We first identified CpGs that change methylation levels in response to a high-fat, high-sucrose (HFHS) diet. The obesogenic response is highly variable among the subset of strains selected, with some strains responding with low percentage of body fat gain and some high (Figure 2.1A). We performed reduced representation bisulfite sequencing (RRBS) on DNA isolated from liver and observed a total of 1,045,665 CpGs with 10x coverage across at least 70% of samples. A majority of CpGs measured did not vary between strains, as they tended to be ubiquitously unmethylated in all samples and were excluded from the analysis. We performed paired sample t-tests on the methylation levels at 161,742 variable CpGs between chow and HFHS groups composed of 45 HMDP strains (Figure 2.1B). This analysis identified 83 CpGs that significantly change in response to HFHS diet group with an FDR $\leq$ 10% (Table 1 and Figure 2.5). There were 32 CpGs with decreased methylation levels in the HFHS group (-7 to -25.5%) and 51 CpGs that increased in methylation (+5 to +19%) in the HFHS group. We ran 1000 permutations of the t-test by randomizing the diet label to identify the false positive rate. The average number of CpGs where the permutation p-value was less than the FDR cut-off, $\leq$ 5E-5, was 25.22 (95%CI = 24.81-25.64), suggesting that the inferred FDR rate may be closer to 30%.

DNA methylation regulates gene expression at the promoters of genes but also at more distal enhancers, so we used the annotation tool GREAT, which assigns non-coding regulatory regions to nearby genes within 1Mbp. This annotation identified 118 genes associated with the 83 HFHS diet-responsive CpGs. GO Term analysis of the annotated genes revealed significant enrichment for genes involved lipid metabolism and cellular replication (Figure 2.1C). Among lipid

metabolism genes that were near the differentially methylated CpGs were *Ldlr, Elovl6, Fasn, Ppara,* and *Scd1*. Several of the 83 CpGs are proximal to the same genes, including *Cdk1*, cyclin dependent kinase 1, a mitosis checkpoint gene, and *Scd1*, a fatty acid biosynthesis gene.

Global liver gene expression from the obesity HMDP was previously quantified using Affymetrix HT_MG430A arrays [26]. Expression values represent the average normalized probe intensity of 1-2 mice per strain, but not necessarily from the same animals pooled for RRBS. Thirty seven of the 45 HMDP strains had previously measured liver expression on both diets. Of the genes present on the array that were annotated to one of the 83 diet-responsive CpGs, 83 CpG methylation-transcript level correlations were significant with a p-value $\leq$ 0.05 (Table 2). This suggests that the diet-responsive methylation changes are likely associated with changes in nearby gene expression. Sixteen CpGs out of the 83 significant CpG-transcript correlations fell within $\leq$ 10kbp of the gene's TSS and 53 of 85 CpGs were located within 50kbp. In addition to gene expression, many CpGs correlate with clinical traits. Average methylation of the 5 CpGs annotated to *Scd1* inversely correlated with *Scd1* expression, body fat percentage, plasma glucose, and plasma HDL levels (Figure 2.2).

Diet-responsive methylation changes in a 5 strain model of weight loss

These 83 diet-responsive CpGs were further examined in a 5-strain study of diet-induced obesity followed by weight loss. The inbred strains were selected based on the variable responses to HFHS identified by Parks et al [26]. We fed mice HFHS for 6 weeks, then placed a subset back to chow for a diet-induced weight loss arm for an additional 4 weeks. At the end of 10 weeks, animals were sacrificed, and tissues collected for methylation profiling.

We observed strain specific changes in adiposity after 6 weeks of HFHS feeding, with BALB/cJ gaining the least and DBA/2J the most (Figure 2.3A). After reversion to weight loss diet for 4 weeks, four strains, A/J, C3H/HeJ, C57BL/6J, and DBA/2J, reverted to their chow adiposities and no longer had significantly more body fat than animals fed chow diet-only for 10 weeks (Figure 2.3B). When we examined DNA methylation changes by HFHS diet exposure, we confirmed that the diet-induced changes were robust across experiments. Three strains, BALB/cJ, C57BL/6J and DBA/2J, were present in both studies. We calculated the average change in methylation within each of the strains after HFHS diet in both studies then correlated the effects. The direction and magnitude of change in DNA methylation at HFHS-variable sites was highly reproducible between experiments (Supplementary Figure 6B). When correlated with body fat in each diet group, methylation specifically at the *Scd1* locus correlated the least with body fat in weight loss compared to chow or HFHS-only. (Supplementary Figure 2.6B).

We performed a two-way ANOVA on methylation levels at 81 of the diet-responsive CpGs between diet groups and strain variables. We identified 44 CpGs with a p-value $\leq$ 0.05 for the diet term. When we performed differential analysis by t-test in the weight loss group compared to chow-only animals, many of the diet-induced changes were nonsignificant, but a fraction of the sites remained differentially methylated ($p \leq 0.05$) (Figure 2.4). Thirty-six of 81 diet-induced CpGs examined in the second cohort did not revert to chow-only levels of methylation across all strains. Although significantly differentially methylated after 6 weeks, it should be noted that most of methylation differences in the weight loss group began to revert to chow-only levels. There were 14 persistently hypermethylated and 22 hypomethylated CpGs. All persistent hypomethylated CpGs were also significant by ANOVA ($p \leq 0.05$) across all 3 diet groups, and 11 of 14 persistently hypermethylated CpGs were significant. The genes associated

with weight loss-persistent CpGs are listed in Table 3. CpGs associated with *Scd1* and *Cdk1* remain significantly hypomethylated following 4 weeks of weight loss.

Discussion

In this study we asked a fundamental question regarding the epigenetic responses to different diets: what happens to DNA methylation changes in liver in response to a HFHS diet challenge and are these changes reversible when mice are fed a low-fat, weight loss diet? By identifying epigenetic changes and profiling weight loss phenotypes in a panel of genetically diverse mouse strains, we were able to evaluate this question in the context of variable gene-by-environment responses. Mouse studies of obesity often overlook genetic and phenotypic variability when discovering epigenetic mechanisms. By identifying diet-responsive CpGs across 45 strains, we were able to identify candidate methylation changes associated with a common response to overnutrition in liver. These changes could be used as a future metric for HFHS exposure agnostic of genetic background. The genes regulated by diet-responsive CpGs in this study are known to be involved in energy homeostasis. Once identified, we investigated the status of these diet-responsive CpGs in the livers of animals that were exposed to HFHS but returned to chow-diet and subsequently reduced their adiposity. We observed a strain-specific phenotype in weight loss, as only one strain of the five, A/J, did not return to chow-only levels of body fat after 4 weeks. And although most strains successfully lost enough body fat to be comparable to age matched, chow-only controls, a large fraction of diet-induced methylation changes remained significantly differentially methylated. This suggests that epigenetic changes revert more slowly than physiological changes, like adiposity.

One of the genes associated with the greatest number of diet-responsive CpGs and persistently differentially methylated after weight loss was *Cdk1*. The CpGs at the Chr10 region annotated only to *Cdk1* and no other nearby gene. Methylation at this locus was also significantly correlated with *Cdk1* expression. *Cdk1* is a gene for a kinase involved in cell entry into mitosis.

Cdk1 inhibition was recently discovered to enhance glucose sensing in pancreatic beta cells by regulating mitochondrial bioenergetics [30]. Epigenetic regulation of *Cdk1* has not previously been implicated in a hepatic response to overnutrition and increased adiposity. Another prominent gene near diet-responsive CpGs was *Scd1*. *Scd1* is a well-studied gene involved in the biosynthesis of monounsaturated fatty acids, critical signaling molecules in energy homeostasis [3]. A clinical study examining methylation at the promoter of *SCD1* in humans identified hypomethylation in obese individuals but an increase in methylation levels following Roux-en-Y Gastric Bypass surgery[31]. The delayed reversal of obesity-induced methylation at *Scd1* in mice could be either due to the length of weight loss time observed in this study or an effect of rapid weight loss due to surgery in humans.

In this study, four weeks of chow diet reversal was sufficient to significantly restore body fat to previous levels in 4 of 5 strains studied. To date, there are few published weight loss studies in mice that use greater than 2 genetically diverse strains to interrogate this phenotype. Leung et al., compared the hepatic chromatin states of C57BL/6J and A/J in the context of diet-induced obesity and weight loss for 16 weeks [23]. The authors identified an obesity resistant and easily reverted phenotype in A/J compared to C57BL/6J animals fed the same obesogenic diet used in these studies. In alignment with this resistant phenotype, the authors identified less persistently accessible regions in A/J compared to C57BL/6J. We did not observe this pattern of epigenetic and body composition plasticity in the A/J strain over the course of our 10 week study, as the A/J strain behaved more similarly to the C57BL/6J cohort from Leung et al. Weight loss studies performed in C57BL/6J animals have also been inconclusive with regard to the reversibility of obesity induced changes, suggesting subtle differences in environment and experimental design may affect the reversion phenotype [24, 32].

In our study we observed that weight loss occurs more rapidly than DNA methylation changes. It is possible that some sites may eventually revert back to their chow state, but the time scale for this can be significantly longer than those for weight loss itself. With respect to the kinetics of epigenetic change, DNA methylation is considered to be the most stable epigenetic mark. Compared to chromatin remodeling mechanisms such as histone deacetylases and demethylases, *DNMT3A* the de novo DNA methylation enzyme, confers more persistent epigenetic changes by silencing gene expression with the slowest kinetics [33]. This suggests that changes to DNA methylation during weight loss are less likely to be reversed within the same period of time as histone modifications or DNA accessibility. As a whole, most strains examined in this study efficiently reversed the obesity phenotype following reversion to a chow diet. However, methylation changes induced by the initial state of obesity are not quickly reversed at loci involved in energy homeostasis, even after adiposity is reversed.

The discordant dynamic between physiological and epigenetic plasticity observed in our study is reminiscent of persistent epigenetic aging acceleration in human obesity. The "epigenetic clock" model, developed by Horvath et al., associates the level of DNA methylation at dozens of CpGs with chronological age [10]. This clock is often used to evaluate the effect of disease states and environmental exposures on tissue physiology by observing the changes in epigenetic age acceleration. Epigenetic age acceleration is a biomarker that is hypothesized to represent age-associated decline in tissue function [34]. Obesity increases the acceleration of epigenetic aging in the liver, and this acceleration is not reversed following bariatric surgery [10]. The accelerated clock markers in humans were enriched for CpGs in close proximity to genes involved in mitochondrial function and oxidative stress. These physiological processes are involved in insulin resistance, a prevalent phenotype in aged individuals that may play a role in

the prolonged physiological reversal of obesity [35]. Studies of diet induced obesity in mice identified persistent insulin resistance following short-term weight loss [22, 38, 39]. Persistent epigenetic alterations have also previously been proposed as a "molecular memory" mechanism in gluconormalized diabetics with an increased risk for retinopathy and additional microvascular complications [36, 37]. Taken together, these studies and our present work suggest that obesity-induced changes to DNA methylation at loci associated with energy homeostasis may be involved in unresolved metabolic adaptation, or epigenetic "memory" following weight loss. This adaptation has potential implications for predicting the success of weight loss, and subsequent risk of future weight regain.

Figures

Figure 2.1. Differential methylation of CpGs in response to HFHS diet.

Forty-five genetically diverse mouse strains were fed an obesifying high-fat, high-sucrose (HFHS) or chow diet for 8 weeks. (A) Shows the strain-specific body fat changes after 6 weeks of diet. Such strains such as DBA/2J and C57BL/6J are high responders to HFHS diet and increase adiposity 15% after 6 weeks compared to chow diet, while other stains like BALB/cJ gain much less. Data shown are mean ± SD (n = 2–3 mice/strain and diet). (B) Differential analysis identifies 83 significant (10% FDR) CpGs out of 161,742 variable CpGs. Out of 1,045,665 CpGs identified by RRBS, only a subset varied between samples. (C) Annotation of significant CpGs to nearby genets and GO Term Pathway enrichment, x axis values represent -log10(FDR) values of term enrichment.

A

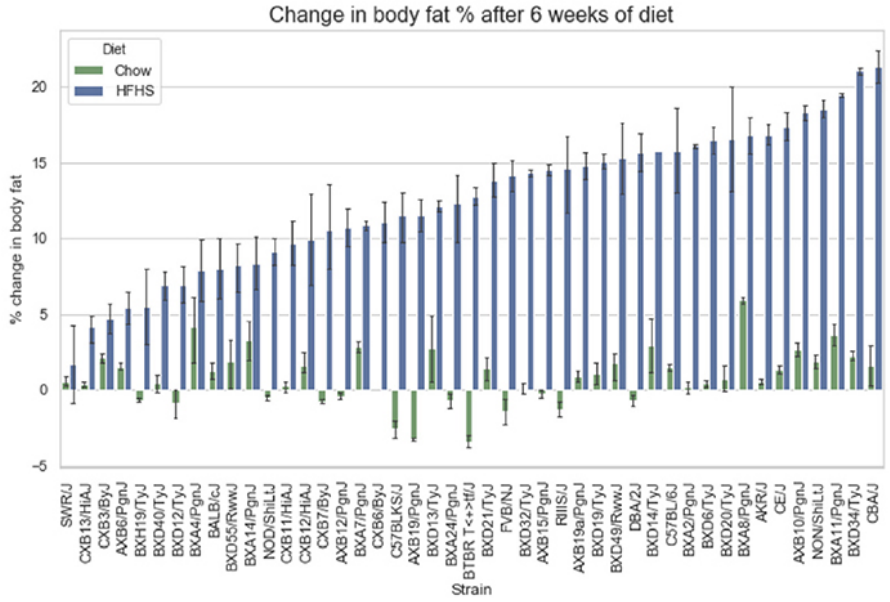
Change in body fat % after 6 weeks of diet
Diet
Chow
HFHS
% change in body fat
Strain

B

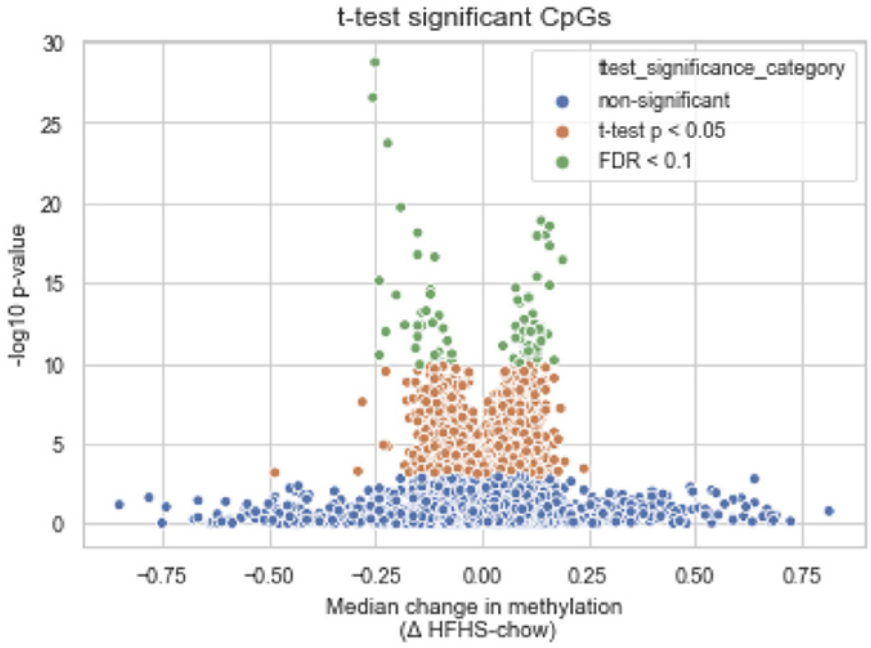
t-test significant CpGs
test_significance_category
non-significant
t-test p < 0.05
FDR < 0.1
-log10 p-value
Median change in methylation
(Δ HFHS-chow)

C

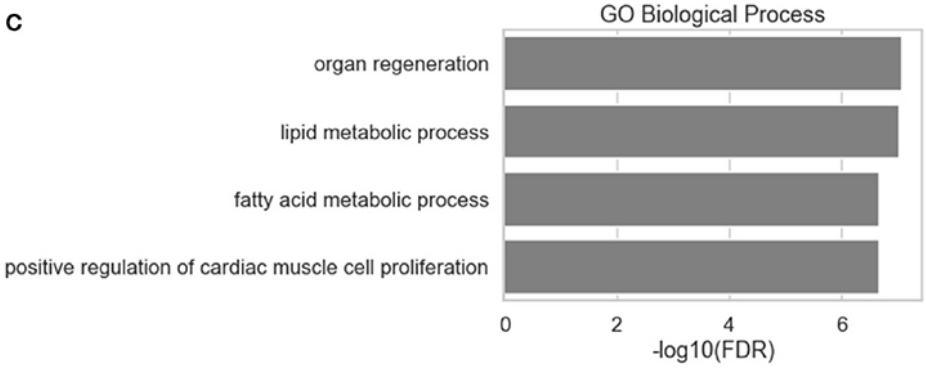
GO Biological Process
organ regeneration
lipid metabolic process
fatty acid metabolic process
positive regulation of cardiac muscle cell proliferation
-log10(FDR)

Figure 2.2 Diet-induced changes in methylation correlate with cis-regulated gene expression and clinical traits.

Correlation plots between the average methylation levels of 5 correlated CpGs on chr19 and microarray transcript levels (A), body fat measured by NMR (B), and plasma glucose (C) and HDL (D) in 37 strains from the obesity HMDP. The blue dots represent the average methylation and trait measurements of a strain fed chow diet, and the orange crosses show data from the same strains fed HFHS diet.

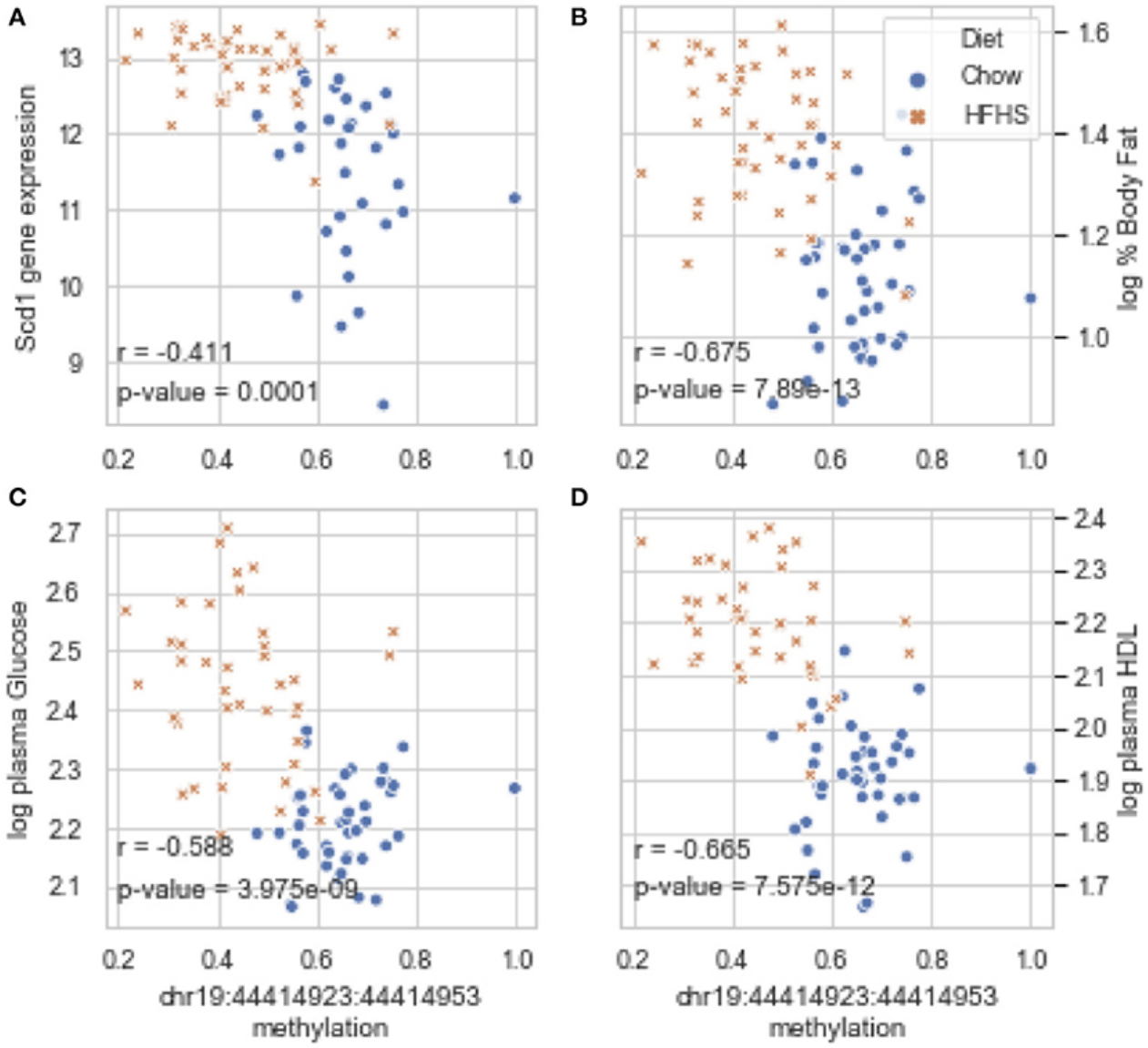
A
Scd1 gene expression
r = -0.411
p-value = 0.0001
B
log % Body Fat
Diet
Chow
HFHS
r = -0.675
p-value = 7.89e-13
C
log plasma Glucose
r = -0.588
p-value = 3.975e-09
chr19:44414923:44414953
methylation
D
log plasma HDL
r = -0.665
p-value = 7.575e-12
chr19:44414923:44414953
methylation

Figure 2.3 Weight loss and replication study.

Five classical inbred strains (A/J, BALB/cJ, C3H/HeJ, C57BL/6J, and DBA/2J) were chosen based on a variable response to HFHS diet in previous studies. Twenty four 8 week old male mice were placed on HFHS (n = 16) or chow (n = 8) for 6 weeks, after which, a subset of 8 mice were placed back to chow (weight loss) for 4 weeks. Body fat percentage measured by NMR is shown over the course of 10 weeks in (A). Data is mean ± SD. T-test comparisons of body weight and total adiposity at the end of the 10 week study show that only the A/J strain has not resolved diet-induced obesity after 4 weeks of diet (B).

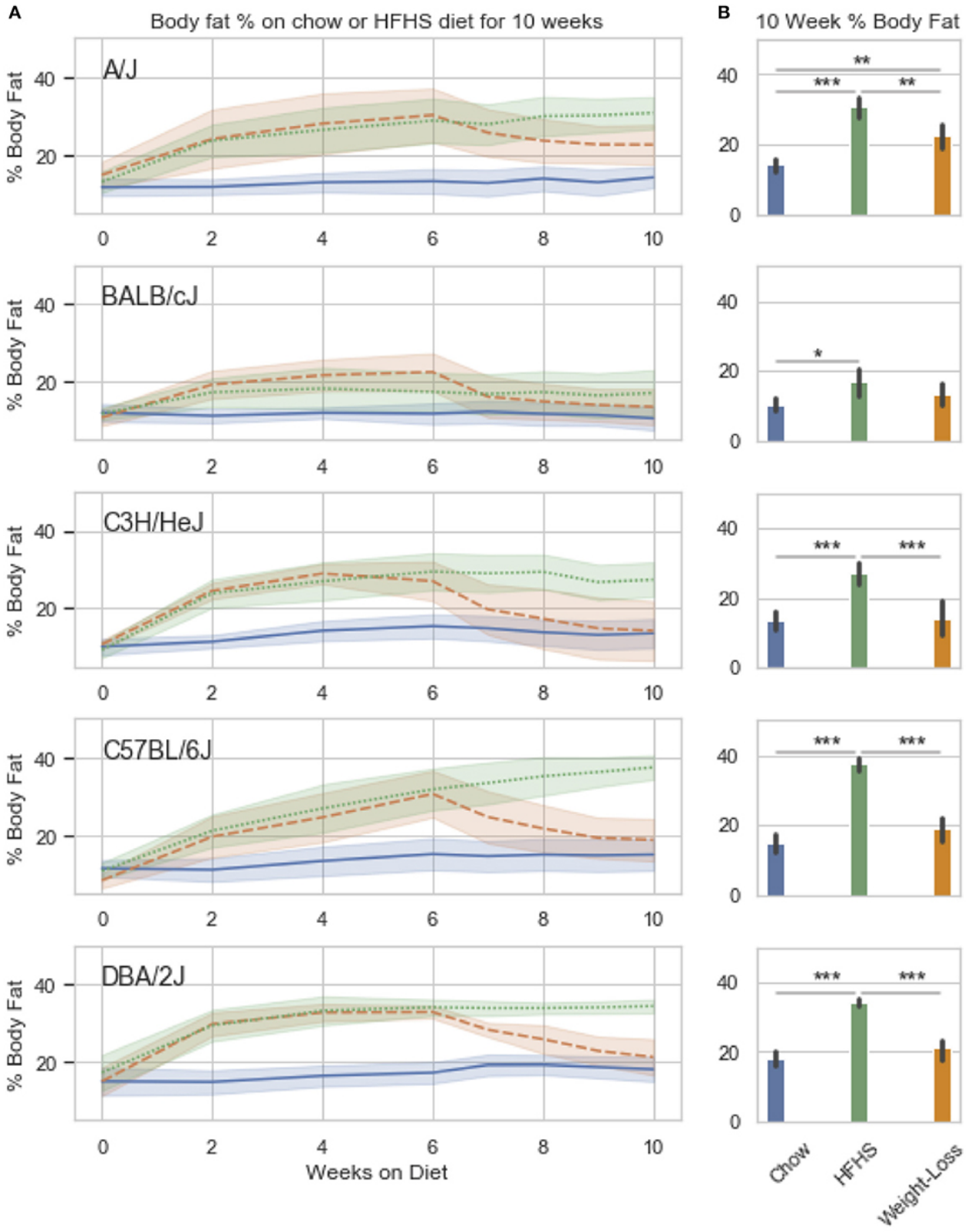
A
Body fat % on chow or HFHS diet for 10 weeks
A/J
BALB/cJ
C3H/HeJ
C57BL/6J
DBA/2J
% Body Fat
Weeks on Diet
B
10 Week % Body Fat
Chow
HFHS
Weight-Loss

Figure 2.4 Persistently differentially methylated CpGs after weight loss.

Thirty-six of 81 diet-responsive CpGs maintained a significant difference in methylation following 6 weeks of weight loss. Colored lines represent the average scaled methylation values of all 5 strains at singular diet-responsive CpGs (n = 15). Y-axis values are min-max scaled, which represents the absolute methylation percentage determined by RRBS relatively scaled to the minimum and maximum measurements of the same CpG across all strains and diets. (Measured methylation-minimum)/(maximum – minimum). (A) Shows examples of 14 persistently hypermethylated CpGs, and (B) shows examples of 22 hypomethylated CpGs.

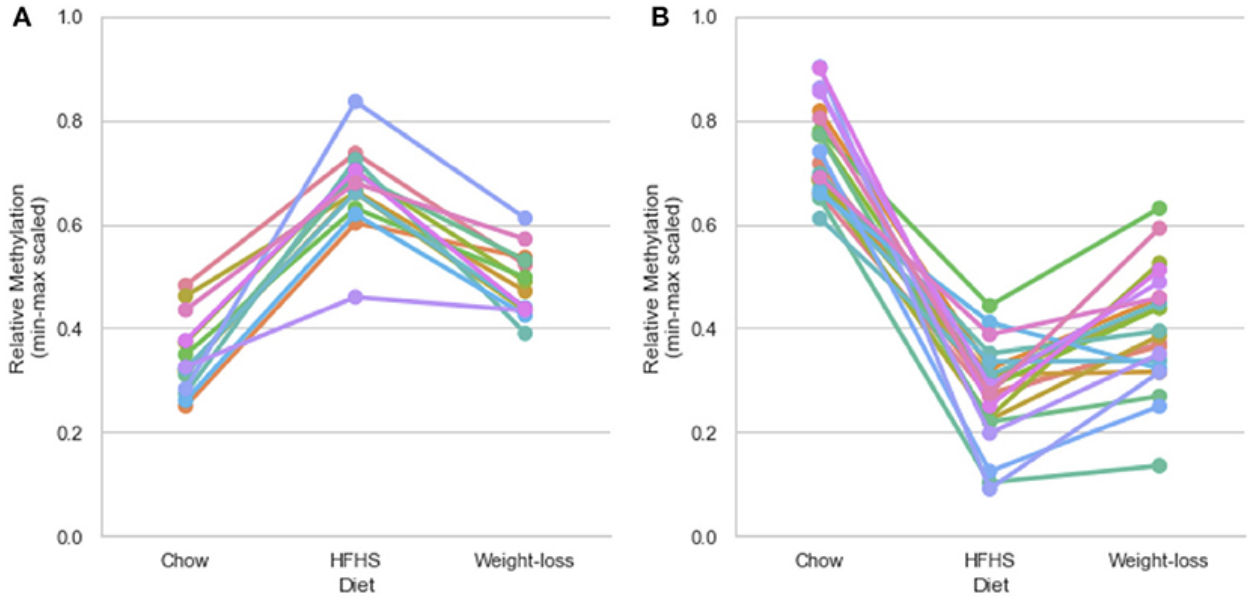

Figure 2.5 Examples of diet-induced methylation changes in all 45 HMDP strains at individual CpGs.

N = 45. Each line represents the change in methylation by HFHS within a single strain. The CpGs on chromosome 15 and 19 are examples of a CpGs that trend toward hypomethylation after HFHS.

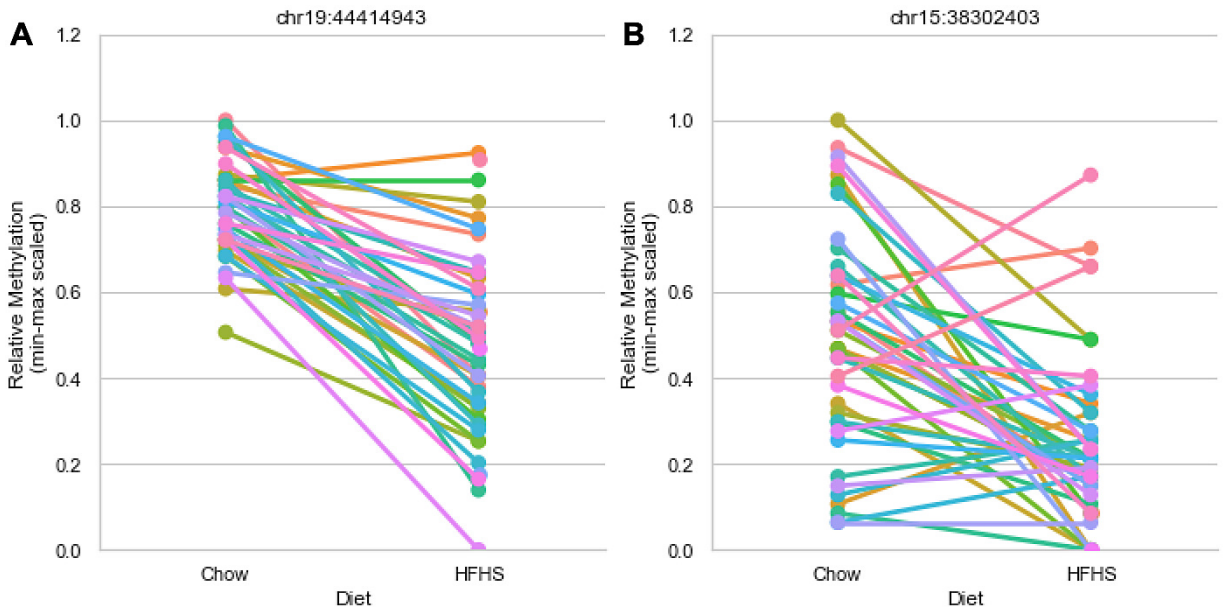

Figure 2.6 The correlation of HFHS diet-induced changes between replicate experiments. (A) Three strains, BALB/cJ, C57BL/6J, and DBA/2J were included in both analyses of HFHS diet-induced methylation changes. Data shown are 81 HFHS-responsive CpGs (as identified in the 45 strain study) shared across both studies in all 3 strains. X axis values represent the delta methylation by HFHS in the 45 strain cohort (exp. 1) and the Y axis values represent the delta methylation between strain averages in the 5 strain cohort (exp. 2). (B) Shows the correlation of Scd1 fragment methylation with body fat across each diet group in weight loss cohort. Pearson correlation coefficients between log body fat percentage and methylation level at chromosome 19 locus identifies a decrease in the fraction of body-fat variation explained by methylation after weight loss.

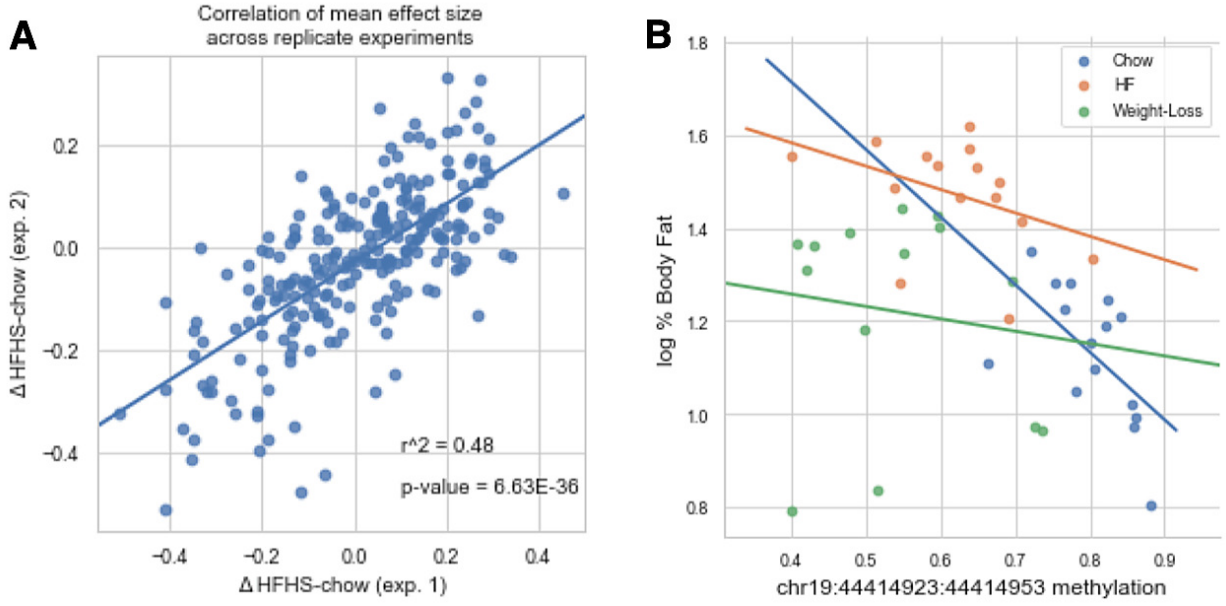

Table 2.1 FDR significant CpGs changed by HFHS diet in 45 strains of mice.

Chr	BP	Median change by HFHS	*t*-test *p*-value	FDR	Annotated gene 1	Distance to TSS	Annotated gene 2	Distance to TSS
1	73957398	0.14	6.28E-09	2.03E-04	Tns1	167049	Tnp1	−941500
1	89466797	0.1	1.46E-05	4.26E-02	Agap1	11987	D130058E05Rik	−463437
1	90962615	0.125	4.50E-05	9.11E-02	Rab17	7046	Prlh	9508
1	133264749	0.105	5.94E-06	2.28E-02	Plekha6	18653	Golt1a	−45074
1	151244113	−0.12	4.65E-07	4.18E-03	Ivns1abp	−100385	Hmcn1	−251063
10	63583522	0.05	1.53E-05	4.26E-02	Ctnna3	126013	Gm10118	343912
10	69248814	−0.1	3.79E-05	8.28E-02	Rhobtb1	35621	Cdk1	104124
10	69248832	−0.18	4.21E-06	2.03E-02	Rhobtb1	35639	Cdk1	104106
10	69248838	−0.15	4.53E-06	2.03E-02	Rhobtb1	35645	Cdk1	104100
10	69248844	−0.19	2.69E-09	1.09E-04	Rhobtb1	35651	Cdk1	104094
10	69248850	−0.2	6.51E-07	5.26E-03	Rhobtb1	35657	Cdk1	104088
10	69248853	−0.14	4.36E-06	2.03E-02	Rhobtb1	35660	Cdk1	104085
10	69248866	−0.15	8.52E-06	2.87E-02	Rhobtb1	35673	Cdk1	104072
11	51785947	0.115	4.89E-06	2.13E-02	Sar1b	22261	Phf15	71706
11	98877224	0.12	4.14E-05	8.82E-02	Wipf2	13587	Cdc6	−30927
11	106818615	0.105	1.44E-05	4.26E-02	Cep95	29341	Smurf2	101855
11	107265371	0.14	5.06E-06	2.13E-02	Nol11	−75991	Pitpnc1	205328
11	117233894	−0.15	4.34E-06	2.03E-02	43717	34234	Gm11733	−250474
11	117820356	0.11	7.08E-07	5.45E-03	Afmid	−5568	Syngr2	10689
11	117820370	0.15	1.51E-08	2.92E-04	Afmid	−5554	Syngr2	10703
11	120821045	−0.1	2.32E-06	1.34E-02	Fasn	3133	Dus1l	−24651
12	73838480	−0.225	6.33E-06	2.28E-02	Hif1a	−69424	Prkch	253684
12	73838512	−0.24	2.73E-05	6.61E-02	Hif1a	−69392	Prkch	253716
12	82399195	0.105	1.51E-05	4.26E-02	Sipa1l1	87847	Gm5435	97342
12	84769968	0.13	1.62E-08	2.92E-04	Npc2	3144	Isca2	−3302
12	85754916	0.08	4.16E-07	3.96E-03	Mfsd7c	8378	0610007P14Rik	69606
12	85975275	0.12	2.12E-06	1.27E-02	Tgfb3	103766	Ttll5	150566
13	46615383	0.1	2.96E-06	1.65E-02	C78339	−54139	Cap2	113536
14	63202824	0.155	7.48E-06	2.57E-02	Neil2	−9284	Gata4	42424
15	7187724	0.16	3.01E-08	4.86E-04	Lifr	33372	Egflam	210580
15	38302403	−0.14	1.94E-06	1.20E-02	Klf10	−1697		
15	38302475	−0.12	6.14E-07	5.23E-03	Klf10	−1769		
15	38302543	−0.07	3.57E-05	8.02E-02	Klf10	−1837		
15	57936054	−0.13	1.74E-06	1.13E-02	Wdr67	23856	Fam83a	−49365
15	85745965	0.08	4.49E-06	2.03E-02	Ppara	10190	Cdpf1	65731
15	85745974	0.09	1.05E-06	7.08E-03	Ppara	10199	Cdpf1	65722
15	85745987	0.13	2.04E-07	2.36E-03	Ppara	10212	Cdpf1	65709
16	24391817	0.09	4.27E-05	8.98E-02	Lpp	−1533		
16	34113282	0.1	2.51E-05	6.25E-02	Umps	−146245	Kalrn	400766
16	38432088	0.08	9.93E-06	3.15E-02	Pla1a	1057	Popdc2	69880
17	28065710	−0.07	2.51E-05	6.25E-02	Tcp11	14874	Anks1	156371
17	28065873	−0.15	5.21E-08	7.67E-04	Tcp11	14711	Anks1	156534
17	28065883	−0.09	5.14E-06	2.13E-02	Tcp11	14701	Anks1	156544
17	47442447	0.125	4.62E-05	9.23E-02	1700001C19Rik	−5073	Taf8	59840
19	44414923	−0.22	5.01E-11	2.70E-06	Scd1	−7215	Wnt8b	−78549
19	44414943	−0.25	3.18E-13	5.15E-08	Scd1	−7235	Wnt8b	−78529
19	44414944	−0.255	2.87E-12	2.32E-07	Scd1	−7236	Wnt8b	−78528
19	44414952	−0.15	1.33E-08	2.92E-04	Scd1	−7244	Wnt8b	−78520
19	44414953	−0.11	6.00E-08	8.09E-04	Scd1	−7245	Wnt8b	−78519
19	53610483	0.14	6.18E-06	2.28E-02	Smc3	10086	Rbm20	−66823
2	4891640	0.105	2.82E-05	6.72E-02	Sephs1	10077	Phyh	−27379
2	31488626	0.11	1.48E-05	4.26E-02	Ass1	18420	Fubp3	−84099
2	31511721	0.13	3.36E-05	7.73E-02	Ass1	41515	Fubp3	−61004
2	32417288	0.085	3.97E-05	8.56E-02	Ptges2	21393	Naif1	−33169
2	32417292	0.09	9.93E-06	3.15E-02	Ptges2	21397	Naif1	−33165
2	32928045	−0.24	2.66E-07	2.87E-03	Rpl12	−33514	Fam129b	51932
2	155185551	0.09	4.36E-05	9.03E-02	Dynlrb1	−50984	Itch	51993
2	160741022	0.075	3.39E-05	7.73E-02	Plcg1	9713	Zhx3	118609
2	174858446	−0.08	1.12E-05	3.47E-02	Edn3	97828	Gm14444	−151873
3	88568840	0.19	7.19E-08	8.94E-04	Ssr2	−10831	Ubqln4	15125
3	129421906	−0.115	3.68E-06	1.98E-02	Enpep	−89187	Elovl6	−110480
3	138224032	0.17	3.77E-05	8.28E-02	Adh7	6210	Adh1	−53462
4	8748959	0.13	2.21E-05	5.72E-02	Chd7	57595	Clvs1	−520358
4	41371302	0.125	3.96E-06	2.03E-02	Ubap1	22307	Kif24	93538
5	92365051	−0.1	2.23E-05	5.72E-02	Cxcl10	−16170	Nup54	70168
5	120483727	0.13	1.71E-05	4.68E-02	Sds	7197	Plbd2	19898
5	123029761	0.085	8.85E-07	6.23E-03	Orai1	14688	Morn3	17255
5	125147678	−0.11	3.21E-05	7.53E-02	Ncor2	31375	Fam101a	144232
5	125463847	0.1	4.73E-05	9.33E-02	Aacs	−11967	Bri3bp	22280
5	142593387	0.16	8.76E-09	2.36E-04	Mmd2	15413	Radil	−42290
5	142593399	0.08	9.27E-06	3.06E-02	Mmd2	15401	Radil	−42302
5	145871583	0.11	7.65E-07	5.62E-03	Cyp3a11	8381	Cyp3a44	−65710
5	146005723	0.16	3.51E-07	3.54E-03	Cyp3a25	3894	Cyp3a11	−125760
5	146005929	0.12	6.54E-06	2.30E-02	Cyp3a25	3688	Cyp3a11	−125966
5	149008580	−0.145	4.98E-05	9.70E-02	Hmgb1	44460	Gm15409	49303
7	80219975	0.1	6.03E-06	2.28E-02	Cib1	12838	Sema4b	33135
7	98352904	0.09	4.46E-05	9.11E-02	Tsku	8384	Acer3	−43367
8	119442446	0.14	1.14E-05	3.47E-02	Necab2	−4273		
8	122231359	0.135	5.38E-06	2.17E-02	Banp	280816	Gm22	−38210
9	21632184	−0.155	1.78E-05	4.80E-02	Smarca4	16016	Ldlr	−91392
9	42461997	0.115	6.25E-06	2.28E-02	Tbcel	10261	Tecta	−62069
9	46243778	−0.11	2.74E-05	6.61E-02	Apoa4	3083	Apoa5	−24855
9	108378240	0.11	2.13E-05	5.66E-02	1700102P08Rik	−14594	Usp4	30410

Table 2.2 Correlation of diet responsive CpG methylation levels with expression of nearby genes.

CpG	Gene 1	R	*p*-value	CpG	Gene 2	R	*p*-value
METHYLATION-EXPRESSION CORRELATIONS WITH ANNOTATED GENES							
chr1:73957398	Tns1	0.06	6.05E-01	chr1:73957398	Tnp1	0.14	2.51E-01
chr1:89466797	Agap1	0.31	9.50E-03				
chr1:90962615	Rab17	0.15	2.04E-01				
chr1:133264749	Golt1a	0.24	4.29E-02	chr1:133264749	Plekha6	0.42	2.47E-04
chr1:151244113	Ivns1abp	−0.34	5.72E−03				
chr10:69248814	Cdk1	−0.37	1.74E-03				
chr10:69248832	Cdk1	−0.46	8.75E-05				
chr10:69248838	Cdk1	−0.42	3.49E-04				
chr10:69248844	Cdk1	−0.55	1.14E-06				
chr10:69248850	Cdk1	−0.48	2.84E-05				
chr10:69248853	Cdk1	−0.42	3.06E-04				
chr10:69248866	Cdk1	−0.43	2.61E-04				
chr11:51785947	Sar1b	0.41	6.51E-04				
chr11:98877224	Cdc6	0.32	7.62E-03				
chr11:107265371	Nol11	0.16	1.74E-01	chr11:107265371	Pitpnc1	0.42	3.00E-04
chr11:117820356	Syngr2	−0.02	8.64E-01				
chr11:120821045	Dus1l	−0.34	5.45E-03	chr11:120821045	Fasn	−0.34	5.81E-03
chr11:117820370	Syngr2	−0.03	8.24E-01				
chr12:73838480	Hif1a	−0.04	7.63E-01	chr12:73838480	Prkch	−0.40	5.06E-03
chr12:73838512	Hif1a	0.02	8.86E-01	chr12:73838512	Prkch	−0.27	6.34E-02
chr12:84769968	Isca2	0.25	4.29E-02	chr12:84769968	Npc2	0.20	9.68E-02
chr12:85754916	Mfsd7c	−0.16	1.89E-01	chr12:85754916	0610007P14Rik	0.39	1.03E-03
chr12:85975275	Tgfb3	0.50	6.21E-06				
chr13:46615383	Cap2	0.45	1.39E-04				
chr14:63202824	Gata4	0.15	2.33E-01				
chr15:7187724	Lifr	0.53	1.55E-06				
chr15:38302403	Klf10	−0.41	4.35E-04				
chr15:38302475	Klf10	−0.33	4.42E-03				
chr15:38302543	Klf10	−0.28	1.76E-02				
chr15:85745965	Ppara	0.50	1.18E-05	chr15:85745965	Cdpf1	0.26	3.22E-02
chr15:85745974	Ppara	0.57	3.08E-07	chr15:85745974	Cdpf1	0.36	2.66E-03
chr15:85745987	Ppara	0.56	7.43E-07	chr15:85745987	Cdpf1	0.35	2.78E-03
chr16:24391817	Lpp	0.45	1.02E-04				
chr16:34113282	Umps	0.37	1.42E-03	chr16:34113282	Kalrn	0.03	8.30E-01
chr16:38432088	Pla1a	−0.41	3.47E-04	chr16:38432088	Popdc2	0.31	9.47E-03
chr17:28065710	Tcp11	−0.35	2.96E-03	chr17:28065710	Anks1	−0.38	1.20E-03
chr17:28065873	Tcp11	−0.38	1.20E-03	chr17:28065873	Anks1	−0.48	2.15E-05
chr17:28065883	Tcp11	−0.31	8.45E-03	chr17:28065883	Anks1	−0.41	4.28E-04
chr17:47442447	1700001C19Rik	0.23	6.07E-02	chr17:47442447	Taf8	0.43	2.73E-04
chr19:44414923	Wnt8b	−0.41	4.90E-04	chr19:44414923	Scd1	−0.59	1.13E-07
chr19:44414943	Wnt8b	−0.51	8.16E-06	chr19:44414943	Scd1	−0.54	2.09E-06
chr19:44414944	Wnt8b	−0.49	1.82E-05	chr19:44414944	Scd1	−0.54	1.76E-06
chr19:44414952	Wnt8b	−0.46	7.50E-05	chr19:44414952	Scd1	−0.49	2.28E-05
chr19:44414953	Wnt8b	−0.36	2.29E-03	chr19:44414953	Scd1	−0.49	1.64E-05
chr19:53610483	Smc3	0.40	6.23E-04				
chr2:4891640	Phyh	0.40	6.42E-04	chr2:4891640	Sephs1	0.37	1.71E-03
chr2:32417288	Ptges2	0.36	2.33E-03				
chr2:32417292	Ptges2	0.39	8.89E-04				
chr2:32928045	Fam129b	−0.48	5.13E-05				
chr2:155185551	Dynlrb1	0.45	7.10E-05	chr2:155185551	Itch	0.40	5.33E-04
chr2:174858446	Edn3	−0.11	3.63E-01				
chr3:88568840	Ssr2	0.62	7.50E-08	chr3:88568840	Ubqln4	−0.16	2.06E-01
chr3:129421906	Elovl6	−0.55	1.27E-06	chr3:129421906	Enpep	−0.50	1.34E-05
chr3:138224032	Adh1	0.20	1.13E-01	chr3:138224032	Adh7	0.20	1.12E-01
chr4:8748959	Clvs1	0.50	9.84E-05	chr4:8748959	Chd7	0.56	6.31E-06
chr4:41371302	Ubap1	0.36	2.25E-03				
chr5:92365051	Cxcl10	−0.20	8.92E-02	chr5:92365051	Nup54	−0.38	1.08E-03
chr5:120483727	Sds	−0.22	9.46E-02	chr5:120483727	Plbd2	−0.33	8.74E-03
chr5:123029761	Orai1	0.03	8.37E-01	chr5:123029761	Morn3	0.40	8.75E-04
chr5:125147678	Ncor2	−0.01	9.27E-01				
chr5:125463847	Aacs	0.29	1.68E-02				
chr5:142593387	Mmd2	0.17	1.55E-01				
chr5:142593399	Mmd2	0.17	1.68E-01				
chr5:145871583	Cyp3a44	0.48	3.12E-05	chr5:145871583	Cyp3a11	0.05	7.12E-01
chr5:146005723	Cyp3a11	−0.16	1.78E-01	chr5:146005723	Cyp3a25	0.19	1.20E-01
chr5:146005929	Cyp3a11	−0.13	3.08E-01	chr5:146005929	Cyp3a25	0.28	2.64E-02
chr5:149008580	Hmgb1	−0.37	1.99E-03				
chr7:80219975	Cib1	0.11	3.68E-01	chr7:80219975	Sema4b	0.39	9.49E-04
chr7:98352904	Tsku	−0.22	7.75E-02				
chr8:119442446	Necab2	0.42	4.30E-04				
chr8:122231359	Banp	−0.13	3.00E-01				
chr9:21632184	Ldlr	0.03	7.98E-01	chr9:21632184	Smarca4	−0.45	1.11E-04
chr9:42461997	Tecta	0.02	8.73E-01	chr9:42461997	Tbcel	0.42	2.67E-04
chr9:46243778	Apoa5	−0.25	4.03E-02	chr9:46243778	Apoa4	−0.07	5.65E-01
chr9:108378240	1700102P08Rik	0.33	5.03E-03	chr9:108378240	Usp4	0.36	2.44E-03

Table 2.3 Diet responsive CpGs with incomplete methylation reversal following 4 weeks of weight loss.

CpG	Gene 1	Gene 2	Median Chow methylation	Median HFHS methylation	Median Weight loss methylation
PERSISTENTLY HYPERMETHYLATED SITES					
chr1:73957398	Tns1	Tnp1	0.75	0.84	0.73
chr11:106818615	Cep95	Smurf2	0.33	0.42	0.48
chr11:107265371	Nol11	Pitpnc1	0.40	0.52	0.44
chr12:85754916	Mfsd7c	0610007P14Rik	0.66	0.72	0.69
chr15:7187724	Lifr	Egflam	0.44	0.53	0.44
chr16:34113282	Umps	Kalrn	0.75	0.83	0.78
chr2:31488626	Fubp3	Ass1	0.46	0.62	0.53
chr2:31511721	Fubp3	Ass1	0.64	0.75	0.65
chr2:160741022	Plcg1	Zhx3	0.30	0.47	0.30
chr3:138224032	Adh1	Adh7	0.48	0.62	0.52
chr4:41371302	Ubap1	Kif24	0.65	0.77	0.74
chr5:123029761	Orai1	Morn3	0.18	0.23	0.20
chr5:125463847	Aacs	Bri3bp	0.46	0.50	0.40
chr5:145871583	Cyp3a44	Cyp3a11	0.74	0.86	0.79
PERSISTENTLY HYPOMETHYLATED SITES					
chr10:69248814	Rhobtb1	Cdk1	0.55	0.47	0.47
chr10:69248832	Rhobtb1	Cdk1	0.68	0.61	0.59
chr10:69248838	Rhobtb1	Cdk1	0.53	0.52	0.46
chr10:69248844	Rhobtb1	Cdk1	0.67	0.58	0.55
chr10:69248850	Rhobtb1	Cdk1	0.61	0.44	0.43
chr10:69248853	Rhobtb1	Cdk1	0.54	0.44	0.42
chr10:69248866	Rhobtb1	Cdk1	0.79	0.71	0.67
chr11:117233894	Gm11733	43717	0.93	0.89	0.89
chr11:120821045	Dus1l	Fasn	0.76	0.76	0.73
chr15:38302403	Klf10		0.22	0.20	0.18
chr15:38302475	Klf10		0.24	0.19	0.16
chr15:38302543	Klf10		0.15	0.15	0.14
chr17:28065710	Tcp11	Anks1	0.31	0.25	0.25
chr17:28065873	Tcp11	Anks1	0.44	0.43	0.44
chr17:28065883	Tcp11	Anks1	0.40	0.40	0.33
chr19:44414923	Wnt8b	Scd1	0.54	0.46	0.42
chr19:44414943	Wnt8b	Scd1	0.81	0.77	0.66
chr19:44414944	Wnt8b	Scd1	0.83	0.72	0.72
chr19:44414952	Wnt8b	Scd1	0.94	0.93	0.93
chr19:44414953	Wnt8b	Scd1	0.96	0.95	0.94
chr5:149008580	Hmgb1	Gm15409	0.63	0.63	0.58
chr9:21632184	Ldlr	Smarca4	0.75	0.70	0.68

References

1. Xu, X., et al., *A genome-wide methylation study on obesity: differential variability and differential methylation.* Epigenetics, 2013. **8**(5): p. 522-533.
2. Wahl, S., et al., *Epigenome-wide association study of body mass index, and the adverse outcomes of adiposity.* Nature, 2017. **541**(7635): p. 81-+.
3. Schwenk, R.W., et al., *Diet-dependent Alterations of Hepatic Scd1 Expression are Accompanied by Differences in Promoter Methylation.* Hormone and Metabolic Research, 2013. **45**(11): p. 786-794.
4. Jiang, M.H., et al., *Hypermethylation of Hepatic Glucokinase and L-Type Pyruvate Kinase Promoters in High-Fat Diet-Induced Obese Rats.* Endocrinology, 2011. **152**(4): p. 1284-1289.
5. Chang, X., et al., *Berberine reduces methylation of the MTTP promoter and alleviates fatty liver induced by a high-fat diet in rats.* Journal of lipid research, 2010. **51**(9): p. 2504-2515.
6. Dudley, K.J., et al., *Offspring of mothers fed a high fat diet display hepatic cell cycle inhibition and associated changes in gene expression and DNA methylation.* PloS one, 2011. **6**(7): p. e21662.
7. Fontana, L., L. Partridge, and V.D. Longo, *Extending healthy life span—from yeast to humans.* science, 2010. **328**(5976): p. 321-326.
8. Feng, W.X., et al., *Analysis method of epigenetic DNA methylation to dynamically investigate the functional activity of transcription factors in gene expression.* Bmc Genomics, 2012. **13**.

9. Cole, J.J., et al., *Diverse interventions that extend mouse lifespan suppress shared age-associated epigenetic changes at critical gene regulatory regions.* Genome Biology, 2017. **18**.

10. Horvath, S., et al., *Obesity accelerates epigenetic aging of human liver.* Proceedings of the National Academy of Sciences of the United States of America, 2014. **111**(43): p. 15538-15543.

11. Barres, R., et al., *Weight loss after gastric bypass surgery in human obesity remodels promoter methylation.* Cell reports, 2013. **3**(4): p. 1020-1027.

12. Stubbs, T.M., et al., *Multi-tissue DNA methylation age predictor in mouse.* Genome biology, 2017. **18**(1): p. 68.

13. Aronica, L., et al., *A systematic review of studies of DNA methylation in the context of a weight loss intervention.* Epigenomics, 2017. **9**(5): p. 769-787.

14. Cordero, P., et al., *Leptin and TNF-alpha promoter methylation levels measured by MSP could predict the response to a low-calorie diet.* Journal of physiology and biochemistry, 2011. **67**(3): p. 463-470.

15. Crujeiras, A.B., et al., *Association of weight regain with specific methylation levels in the NPY and POMC promoters in leukocytes of obese men: a translational study.* Regulatory peptides, 2013. **186**: p. 1-6.

16. Lopez-Legarrea, P., et al., *SERPINE1, PAI-1 protein coding gene, methylation levels and epigenetic relationships with adiposity changes in obese subjects with metabolic syndrome features under dietary restriction.* Journal of clinical biochemistry and nutrition, 2013. **53**(3): p. 139-144.

17. Milagro, F.I., et al., *A dual epigenomic approach for the search of obesity biomarkers: DNA methylation in relation to diet-induced weight loss.* Faseb Journal, 2011. **25**(4): p. 1378-1389.

18. Perez-Cornago, A., et al., *DNA hypermethylation of the serotonin receptor type-2A gene is associated with a worse response to a weight loss intervention in subjects with metabolic syndrome.* Nutrients, 2014. **6**(6): p. 2387-2403.

19. Nicoletti, C.F., et al., *DNA methylation and hydroxymethylation levels in relation to two weight loss strategies: energy-restricted diet or bariatric surgery.* Obesity surgery, 2016. **26**(3): p. 603-611.

20. Bouchard, L., et al., *Differential epigenomic and transcriptomic responses in subcutaneous adipose tissue between low and high responders to caloric restriction.* The American journal of clinical nutrition, 2009. **91**(2): p. 309-320.

21. Moleres, A., et al., *Differential DNA methylation patterns between high and low responders to a weight loss intervention in overweight or obese adolescents: the EVASYON study.* The FASEB Journal, 2013. **27**(6): p. 2504-2512.

22. Schmitz, J., et al., *Obesogenic memory can confer long-term increases in adipose tissue but not liver inflammation and insulin resistance after weight loss.* Molecular Metabolism, 2016. **5**(5): p. 328-339.

23. Leung, A., et al., *Persistent Chromatin Modifications Induced by High Fat Diet.* Journal of Biological Chemistry, 2016. **291**(20): p. 10446-10455.

24. Siersbaek, M., et al., *High fat diet-induced changes of mouse hepatic transcription and enhancer activity can be reversed by subsequent weight loss.* Scientific Reports, 2017. **7**.

25. Orozco, L.D., et al., *Epigenome-Wide Association of Liver Methylation Patterns and Complex Metabolic Traits in Mice.* Cell Metabolism, 2015. **21**(6): p. 905-917.

26. Parks, B.W., et al., *Genetic Control of Obesity and Gut Microbiota Composition in Response to High-Fat, High-Sucrose Diet in Mice.* Cell Metabolism, 2013. **17**(1): p. 141-152.

27. Guo, W., et al., *BS-Seeker2: a versatile aligning pipeline for bisulfite sequencing data.* Bmc Genomics, 2013. **14**.

28. Bennett, B.J., et al., *A high-resolution association mapping panel for the dissection of complex traits in mice.* Genome research, 2010. **20**(2): p. 281-290.

29. McLean, C.Y., et al., *GREAT improves functional interpretation of cis-regulatory regions.* Nature Biotechnology, 2010. **28**(5): p. 495-U155.

30. Gregg, T., et al., *Obesity-dependent CDK1 signaling stimulates mitochondrial respiration at complex I in pancreatic β-cells.* Journal of Biological Chemistry, 2019. **294**(12): p. 4656-4666.

31. Morcillo, S., et al., *Changes in SCD gene DNA methylation after bariatric surgery in morbidly obese patients are associated with free fatty acids.* Scientific Reports, 2017. **7**.

32. Guo, J., et al., *Persistent Diet-Induced Obesity in Male C57BL/6 Mice Resulting from Temporary Obesigenic Diets.* Plos One, 2009. **4**(4).

33. Bintu, L., et al., *Dynamics of epigenetic regulation at the single-cell level.* Science, 2016. **351**(6274): p. 720-724.

34. Horvath, S., *DNA methylation age of human tissues and cell types.* Genome Biology, 2013. **14**(10).

35. Short, K.R., et al., *Decline in skeletal muscle mitochondrial function with aging in humans.* Proceedings of the National Academy of Sciences, 2005. **102**(15): p. 5618-5623.

36. Reddy, M.A., E.L. Zhang, and R. Natarajan, *Epigenetic mechanisms in diabetic complications and metabolic memory.* Diabetologia, 2015. **58**(3): p. 443-455.

37. Rosen, E.D., et al., *Epigenetics and epigenomics: implications for diabetes and obesity.* Diabetes, 2018. **67**(10): p. 1923-1931.

38. Miao, F., et al., *Evaluating the role of epigenetic histone modifications in the metabolic memory of type 1 diabetes.* Diabetes, 2014. **63**(5): p. 1748-1762.

39. Chen, Z., et al., *Epigenomic profiling reveals an association between persistence of DNA methylation and metabolic memory in the DCCT/EDIC type 1 diabetes cohort.* Proceedings of the National Academy of Sciences, 2016. **113**(21): p. E3002-E3011.

Chapter 3: The characterizing the role of Nicotinamide N-methyl transferase in mouse models of atherosclerosis

Introduction

We previously carried out a GWAS for atherosclerotic lesion area and related traits in the Hybrid Mouse Diversity Panel (HMDP), a panel of about 100 different inbred strains of mice [6]. We refer to this panel as the Atherosclerosis HMDP. We observed extensive (several hundred-fold) variation in atherosclerosis susceptibility and identified several loci for lesion size and atherosclerosis risk factors. For example, we recently reported the identification of genetic variation of the ZHX2 transcription factor as causal for the atherosclerosis resistance of strain BALB/cJ [7]. We now report analysis of a candidate gene (*Nnmt*) encoding nicotinamide N-methyltransferase (NNMT) that resides in a locus on chromosome 9 associated with atherosclerosis in both male and female mice.

NNMT has previously been studied in the context of metabolism and obesity [8,9]. It serves to methylate its substrate, nicotinamide (NAM), the amide of vitamin B3 or niacin, producing N-methyl nicotinamide (MNAM). MNAM levels are associated with hyperlipidemia in genetic mouse models and are elevated in patients with coronary artery disease [10,11]. NNMT uses s-adenosyl methionine (SAM) as a methyl donor and releases s-adenosyl homocysteine (SAH). S-adenosyl homocysteine is a precursor to homocysteine, a metabolite associated with an increased risk of adverse cardiovascular events [12]. The substrate of NNMT, nicotinamide, can also be incorporated into nicotinamide adenine dinucleotide (NAD) and nicotinamide adenine dinucleotide phosphate (NADP), which, in their reduced state (NAD+ and NADP+) act as coenzymes in a large spectrum of oxidation-reduction reactions, notably the electron transport chain in mitochondria. As such, NNMT may compete for substrate with pathways that require

SAM or NAD. For example, SAM serves as a precursor in the synthesis of polyamines, and the reduction in SAM pools by NNMT likely leads to a corresponding reduction in energy waste associated with polyamine flux [9]. Thus, NNMT stands at the confluence of several major pathways that are vital to overall energy homeostasis, such as glucose and cholesterol metabolism [13].

Kraus and colleagues previously used an antisense oligonucleotide (ASO) to suppress *Nnmt* expression in liver and adipose [9]. They observed that mice treated with the ASO were protected from diet-induced obesity and exhibited increased energy expenditure. These effects were mediated in part by elevated SAM levels in adipose tissue and a subsequent increase in energy wastage through the production of polyamines leading to energy wastage. In contrast, SAM levels in the liver did not change by the ASO treatment [9]. Another study by Hong et al. suppressed *Nnmt* in mouse liver using an adenoviral vector expressing an shRNA[8]. In mice fed a chow diet, they observed an increase in plasma cholesterol and showed that this was mediated at least in part by an increase in the enzymatic product N-methylnicotinamide (MNAM) which, in turn, stabilized the NAD+ dependent acetylase Sirtuin 1[8]. We now extend the analysis of the effects of *Nnmt* suppression to hyperlipidemic mouse models of atherosclerosis. We find that knockdown by the same ASO used by Kraus and colleagues results in dramatic protection against atherosclerosis, approximately 10-fold. Our results indicate that circulating levels of NAM or MNAM are not responsible for the protection against atherosclerosis and suggest that NNMT action in a cell type(s) directly relevant to atherosclerosis is responsible.

Methods

Mice and Diets. The *Apoe*-Leiden, human CETP transgenic mice and diets were as previously described [6]. All other mice were purchased from The Jackson Laboratory.

Antisense oligo experiments. To test the impact of *Nnmt* ASO on lesion area and related lipid parameters, mice carrying transgenes for human cholesterol ester transfer protein (CETP) and ApoE Leiden on a C57BL/6 genetic background received weekly injections of *Nnmt* antisense oligo (Ionis Pharmaceuticals oligo number 407074 or 407019) or control oligo (Ionis Pharmaceuticals oligo number 141923) as previously described. Oligos (50mg/kg/week) were administered by I.P. injection beginning at 5 weeks of age. At 8 weeks of age, animals were transferred to a "Western Style" synthetic high fat diet (33 kcal % fat from cocoa butter) supplemented with 1% cholesterol (Research Diets D10042101). After 16 weeks on diet, animals were euthanized for the collection of tissue. Animals were maintained on a 12hr light-dark cycle, 6AM-6PM with ad libitum access to water and chow or experimental diet. Euthanasia of all mice was carried out using deep anesthesia with isoflurane vapor followed by cervical dislocation, a procedure consistent with recommendations of the A.V.A.

MNAM diet experiments. To test the impact of dietary methyl-nicotinamide (MNAM), male *Ldlr-/-* animals (The Jackson Laboratory, Strain number 2207) were fed a control Western diet (Research Diets D10042101) or an identical formulation supplemented with 1% (wt/wt) MNAM (Research Diets D16091501) (MNAM was from Combi-Blocks, San Diego, CA, Catalog number QD-2369) . The Western diet was fed beginning at 8 weeks of age and animals were euthanized for tissue collection after 16 weeks.

NAM drinking water experiments. Eight-week-old male and female *Ldlr-/-* mice were acquired from JAX (The Jackson Laboratory, Strain number 2207) and monitored for average daily drinking water volume. After one week of monitoring, nicotinamide (NAM from Sigma N0636) or beta-nicotinamide mononucleotide (AABlocks AA003858) were added to drinking water at a dose of 500mg/kg/day. The mice were exposed to the treated drinking water for two weeks before starting the 12-week Western diet regimen.

Plasma Phenotypes. Plasma was collected from the retro orbital plexus under isoflurane vapor anesthesia at the time of euthanasia at approximately 24 weeks of age. Animals were fasted for 4h beginning at 6AM. Blood was collected using heparinized glass capillary tubes into plasma collection tubes with EDTA (Becton Dickerson). Blood was kept on ice until centrifuged and the separated plasmas were frozen at -80°C in aliquots for subsequent analyses. Plasma lipid profiles were measured by colorimetric analysis as previously described [39,40].

Atherosclerotic lesions. Lesion area in the proximal aorta was quantitated as previously described. Briefly, the aorta was flushed with PBS and embedded in OCT. Frozen sections (10 μm) were stained with Oil Red O and lesion areas quantified in every 3rd section through the proximal aorta. Immuno-histochemical staining α-smooth muscle actin (α-SMA) and CD68 were carried out as previously described.

VLDL-Cholesterol secretion. After 16 h fasting, blood was collected from mice at baseline (time 0). The mice were then injected with poloxamer 407 (Sigma) intraperitoneally at a dose of

1 g/kg body weight. After 2 h, blood samples were collected and the mice were euthanized for tissue collection. Plasma cholesterol levels at times 0 and 2 h were determined as described above. The rate of VLDL- secretion was then calculated as described [44].

Immunohistochemistry. Immuno-histochemical procedures for determining smooth muscle cell actin and CD68 were as previously described[6]. For Ki67 (cell proliferation) and Caspase3 (apoptosis), immunohistochemistry was carried out by a variation of the procedure described by Tang, et al. Briefly, 10μm thick frozen aortic sections were brought to the room temperature (R.T.), fixed in 4% paraformaldehyde, permeabilized with 0.1% Triton X-100, and blocked with 5% normal goat serum and 3% bovine serum albumin. Subsequently, sections were incubated with anti-Ki-67 (1:750 dilution, abcam, Cambridge, MA) or activated caspase-3 (1:1000 dilution, abcam) together with anti-Mac-3 (1:400 dilution, B.D. Biosciences, San Jose, CA) for overnight at 40C. After washing with PBS, corresponding secondary antibodies goat anti-rabbit (Alexa Fluor® 488, abcam) and goat anti-rat (Alexa Fluor® 594, Life Technologies, Waltham, MA) were applied for 1 hour at R.T. and cover slips were mounted with fluoroshield containing DAPI (Sigma, St. Louis, MO). Sections were then visualized using a Nikon Eclipse microscope. The percent of Mac-3 positive cells that were also positive for Ki67 or Caspase3 was used as an indicator of relative proliferation or apoptosis in animals treated with control or *Nnmt* ASO

Metabolomics. Metabolomic analysis was carried out at the West Coast Metabolomics Center, University of California, Davis. Sample preparation was as follows: 30μl plasma samples were extracted with 1 ml of degassed acetonitrile: water (95:5, v/v) at –20°C, centrifuged and decanted with subsequent evaporation of the solvent to complete dryness. A clean-up step with

acetonitrile/water (1:1) removes lipids. The cleaned extract was aliquoted into two equal portions and the supernatant dried down again. Internal standards C08-C30 FAMEs wer added and the sample was derivatized usin methoxyamine hydrochloride in pyridine and subsequently by N-methyl-N-trimethylsilyltrifluoroacetamide for trimethylsilylation of acidic protons. GCTOF analysis was as follows: Plasma samples are analyzed by Agilent 6890 GC/LECO HR MS TOF equipped with GERSTEL single arm, Automated Liner Exchange (ALEX) and cold injection system (C.I.S.). Injector is set to 50°C initial temperature and programmed to reach to 270°C at 12°C/min. G.C. oven program is set to initial temperature of 50°C, held 1.0 min, to 330°C at 20°C/min, held at 330°C for 10min. Carrier gas helium flow rate was 1.0ml/min. A 30m long, 0.25mm i.d., 0.25µm film R.T.X. 5-MS column was used. Transfer line, ion source and quadrupole temperatures were set at 280°C, 250°C, and 150°C, respectively and solvent delay were adjusted to 330sec. Peak picking, alignment and identifications were performed by Binbase, an automated metabolite matching tool that uses retention index mass spectral data for identification to avoid misidentifications.

AAV-mediated Suppression of *Nnmt* Expression. Tissue-specific knockdown of *Nnmt* was achieved using AAV vectors expressing a chimeric miR-30 construct (shRNAmiR), in which the endogenous stem-loop structure was replaced with a sequence targeting *Nnmt*. A panel of 7 candidate shRNAmiRs selected from a precomputed list of predicted Sensor-based shRNA sequences was screened for efficacy in a transient transfection-based in vitro assay. Briefly, shRNAmiR expression vectors were co-transfected with a reporter consisting of a fusion between Gaussia luciferase and *Nnmt* cDNA sequences in HEK293 cells followed by luciferase activity measurements. The most efficacious shRNAmiR sequence

(ACCCTGAAGAGTAGCTACTACATAGTGAAGCCACAGATGTATGTAGTAGCTACTCT TCAGGGC) was inserted into the 3'UTR of GFP of pENN.AAV.TBG.PI.EGFP and pENN.AAV.hADP.EGFP-m vectors (Penn Vector Core, University of Pennsylvania) for liver and adipose-specific expression, respectively. AAV constructs were packaged at the Penn Vector Core as AAV8 serotype and intravenously injected at doses of 2-3 x 10^{12} genome copies per mouse.

RNA expression profiling.. Six samples per sex, tissue, and experimental treatment were selected for RNA sequencing. The samples analyzed were selected based on lesion size after 16 weeks of ASO and diet. Mice with the largest lesion area in the control group and mice with the smallest lesion area in the treatment group were selected. Genomic DNA and RNA were simultaneously isolated from 10-20 mg of whole liver tissue using Qiagen AllPrep DNA/RNA kit and protocols. 10-20 mg of frozen gonadal adipose tissue was homogenized using the Qiagen TissueLyzer and RNA was extracted using Qiazol/chloroform. RNA concentration and 260/280 ratios were measured using Nanodrop. RIN^e values were calculated by TapeStation RNA analysis. All samples prepped for sequencing had RIN^e values greater than or equal to 6.5 with an average of 8.0 across all samples.

mRNA was prepared for sequencing using KAPA's mRNA HyperPrep kit for Illumina sequencing platforms by a PerkinElmer Janus Automated workstation. Final libraries were sequenced with 50-bp single end reads on an Illumina HiSeq4000. Adapter sequences were removed from reads using Cutadapt. Trimmed reads were mapped to the mm10 reference genome using the STAR aligner. Adipose samples had an average coverage of 14.7 million reads with a mappability of 83.19% and liver samples had an average coverage of 16.5 million reads

with a mappability of 79.99%. Differential expression between *Nnmt* and control ASOs was calculated by the R package 'DESeq2' using all 6 biological replicates.

Results

Identification of *Nnmt* as a causal gene at the mouse Chromosome 9 locus associated with atherosclerotic lesion area.

High resolution mapping of atherosclerosis in the Ath HMDP identified a locus on Chromosome 9 that was significantly associated with atherosclerosis in both male and female mice (Figure 3.1A). Previously, we and others had identified a broad region of mouse chromosome 9 associated with aortic lesions using linkage analyses of crosses between inbred strains, including an F2 intercross between strains C3H/HeJ and C57BL/6J on a hyperlipidemic (*Apoe*$^{-/-}$) background [14]. The region identified by association occurs in a large linkage disequilibrium block of about 5 Mb (at 47-52 Mb) that contains a total of 48 annotated genes (Figure 3.1B and Table 3.1). To prioritize the genes, we identified those exhibiting significant local expression quantitative trait loci (eQTL) or structural variants. Since the complete genomes of most of the strains constituting the HMDP have been sequenced, we were able to identify nonsynonymous coding variants (Table 3.1), and those predicted to have deleterious effects were identified using the PROVEAN algorithm [15]. We were able to identify genes in the locus that had gene expression levels correlated driven by the local genetic variation ("cis eQTLs"). A total of seven genes in the region exhibited significant local eQTL in female liver (Table 3.1). As discussed below, the *Nnmt* gene, encoding the enzyme nicotinamide n-methyltransferase, was chosen for further studies based on the following: First, *Nnmt* exhibits a very strong local eQTL in liver and aorta. Second, among the Chr. 9 locus genes, the expression of *Nnmt* in liver and aorta was most strongly correlated with atherosclerosis. Third, when the *Nnmt* transcript levels were included as a covariate when calculating the association of the Chr.9 locus with atherosclerosis, the association was greatly reduced.

To directly test the impact of *Nnmt* gene expression on atherosclerosis, we treated hyperlipidemic mice with *Nnmt* antisense or control oligonucleotides (ASO) for 16 weeks on a high fat, high cholesterol diet. The ASOs previously modulated *Nnmt* expression in both liver and adipose tissue in the context of diet-induced obesity. Our experiments used the same genetic and dietary drivers to induce hypercholesterolemia as we previously described for the Atherosclerosis HMDP experiments, namely, an APOE-Leiden/CETP transgenic background in conjunction with the atherogenic diet. Specifically, male and female C57BL/6J mice carrying human transgenes for ApoE-Leiden and Cholesterol Ester Transfer Protein (CETP) received weekly intraperitoneal injections of the *Nnmt* ASO or a control ASO, beginning at five weeks of age. At eight weeks of age, the mice transitioned from chow to a defined high-fat, high-cholesterol diet and consumed the diet *ad libitum* until the mice reached 24-25 weeks of age, at which time the mice were euthanized for collection of tissues (Figure 3.2A). ASO treatment reduced *Nnmt* expression in the liver by about 60% in females and 85% in males (Figure 3.2B). Plasma lipid levels were measured, and aortic lesions in the aortic root were examined for lipid deposition using oil red O staining as previously described [22]. Treatment with the *Nnmt* ASO reduced median lesion size 10- to 5-fold in both female and male mice, respectively (Figures 3.2C and 3.2D). There was no discernible effect of the ASO treatment on lesion morphology based on the composition of lesions as determined by staining for macrophages (CD68) and smooth muscle cells (alpha-smooth muscle cell actin) (Figure 3.2E).

Genetic regulation of *Nnmt* in liver and adipose is tissue dependent.

Nnmt is expressed in a variety of tissues, including liver, adipose, and arteries [16,17]. Gene expression was previously measured in HMDP strains from liver, adipose, aorta, and muscle on

chow, high fat/high sucrose (High Fat), high fat/high cholesterol (Atherosclerosis) diets. We examined the association between genetic variation (SNPs) and *Nnmt* expression (eQTLs) in these datasets and performed correlations between transcript abundances to identify the extent to which *Nnmt* expression is correlated with the expression of other genes in the same tissue. We found that *Nnmt* expression in liver was largely determined by a local eQTL on chromosome 9 (p=1E-25), with a singular lead SNP (rs33700043) explaining 30-70% of the variance across all liver datasets (Figure 3.3A). In contrast, in all except chow-fed males *Nnmt* expression showed no evidence of *cis*-regulation by rs33700043, suggesting that adipose *Nnmt* expression cannot explain the chromosome 9 association.

We calculated the contribution of the cis-component of *Nnmt* gene expression on atherosclerosis by correlating lesion area and the median value for each allele at the SNP with the strongest cis-eQTL in aorta and liver. By examining the nearby SNP with the greatest association with expression, we assumed that genetic variation at this locus was causal for variation in gene expression. We found a significant relationship with bicor values greater than 0.4 and p-values less than 1.6E-05 (Figures 3.3B and 3.3C). In liver and aorta the reference allele led to a higher expression of *Nnmt* which was significantly correlated with greater lesion area. These data suggest that increased *Nnmt* expression in liver and aorta is caused by local (chromosome 9) genetic variation and positively correlated with lesion area.

Nnmt expression in the HMDP is significantly correlated with clinical traits, plasma lipids, and plasma metabolites.

Previous studies with the atherosclerosis HMDP quantified the expression of thousands of transcripts in liver and aorta and performed correlation analyses on expression levels and

metabolite levels within- and between-tissues [6]. We observed significant correlations with *Nnmt* expression in liver and aorta and lesion area (Figure 3.4). In addition to significant associations with lesion area, *Nnmt* expression is significantly negatively correlated with body weight, liver weight, and plasma cholesterol and triglyceride in males.

In metabolomic screening of plasma from females of the Atherosclerosis HMDP, we observed significant correlations between the expression of *Nnmt* in aorta or liver and plasma metabolites from the urea cycle, ornithine and arginine (Figure 3.4). Previous studies in adipose showed that *Nnmt* influences polyamine flux in adipose tissue and inhibition of *Nnmt* leads to an increase in polyamine flux [9]. In both aorta and liver datasets from the Atherosclerosis HMDP, *Nnmt* expression is negatively correlated with plasma ornithine and positively correlated with plasma arginine. Arginine is known to influence vascular function through the production of nitric oxide (NO) and the production of polyamines necessary for cellular proliferation [18]. We observed significant positive correlations between *Nnmt* transcript abundance and arginosuccinate synthetase, *Ass1,* a step in the urea/citrulline-NO cycle (Figure 3.5A).

We examined correlations between *Nnmt* expression in liver or aorta and the expression of genes in key pathways known to be relevant to atherosclerosis susceptibility or NNMT function such as LDL oxidation, NAD metabolism, inflammation, glycolysis, and mitochondrial respiration. (Figure 3.5A). NNMT is a methyltransferase which utilizes S-adenosylmethionine (SAM) as a substrate to methylate NAM, thereby influencing the cellular carbon pool and one carbon metabolism. We observed significant correlations between tissue *Nnmt* levels and the expression of one-carbon metabolism genes in liver and aorta (Figure 3.5A). The Sirtuin family of proteins (*Sirt1-7*) are NAD+ dependent enzymes involved in the deacetylation of proteins in the nucleus and mitochondria and are known as downstream targets of NNMT function. The

substrate of NNMT, nicotinamide, is known to directly inhibit SIRT activity, while previously published studies modulating the expression of *Nnmt* identified a link between the product of NNMT, MNAM, and the stabilization of SIRT1 protein in the liver [8,20]. Located in the nucleus, SIRT1 is known to regulate protein synthesis, lipogenesis, gluconeogenesis, and bile acid homeostasis in the liver [21]. In the Atherosclerosis HMDP, hepatic *Sirt1* expression was not significantly correlated with any clinical traits. SIRT3 is a mitochondrial Sirtuin involved in deacetylation of proteins involved in fatty acid metabolism. Compared to *Sirt1, Sirt3* expression in the liver was more significantly correlated with plasma cholesterol traits and liver mass, as well as the expression of target nuclear receptors, LXR, SREBP, PGC1a, PPARα, and FOXO1 (Figure 3.5B).

Nnmt knockdown has a significant impact on body mass, adiposity, liver mass insulin levels and plasma metabolites.

We observed that 16 weeks of ASO treatment led to reduced average total body fat as determined by NMR and gonadal fat pad weight (Figure 3.2G). As previously shown, ASO treatment had a substantial effect on body fat [9]. The effect on body composition was considerably larger in males (Figure 3.2F). Both sexes showed a significant increase in liver weight with ASO treatment (Figure 3.2H). The levels of liver cholesterol and triglycerides were not significantly affected by ASO treatment, although there was a trend toward increased levels which may partially explain the increased liver weights observed (Figures 3.2I and 3.2J).

***Nnmt* ASO effect on plasma metabolites, insulin and lipids.**

Polar metabolite analysis of the plasma showed that *Nnmt* knockdown decreased levels of the product of NNMT, methylnicotinamide (MNAM), and increased levels of plasma nicotinamide (NAM) levels in male mice (Figures 3.6A and 3.6B). ASO treatment did not have a significant effect on plasma glucose levels (Figure 3.6C), but it did markedly reduce insulin levels in males but not females (Figure 3.6D). The *Nnmt* ASO also reduced plasma apoB-containing lipoproteins (LDL and VLDL-cholesterol) while there was no significant effect on HDL-cholesterol levels (Figures 3.6E and 3.6F). Correlations between plasma LDL and VLDL values and lesion area within control or *Nnmt* ASO groups were significantly positively correlated (p-value $\leq$ 0.001) (Figure 3.10D). Fast Protein Liquid Chromatography (FPLC) analysis of plasma from ASO and control animals confirmed the impact ASO treatment had in reducing LDL/VLDL cholesterol (Figure 3.6G). The *Nnmt* ASO treatment did not significantly affect lipoprotein secretion as judged by plasma triglyceride accumulation following Triton injection, suggesting that lipoprotein turnover was affected.

Plasma NAM levels do not explain effects of ASO knockdown on atherosclerosis.

Circulating levels of nicotinamide can influence tissue-wide NAD+ salvage, as nicotinamide is a substrate for NAMPT, the enzyme that converts nicotinamide into nicotinamide mononucleotide (NMN), the precursor to NAD+. Therefore, we tested whether circulating NAM levels could explain the effect of NNMT expression on atherosclerosis.

We previously performed mass-spectrometry based untargeted metabolomic analysis on a subset of plasma from the female Atherosclerosis HMDP study [6]. Because we observed such strong correlation between *Nnmt* expression in different tissues and clinical traits, we were interested in determining whether the substrate of NNMT, NAM was also correlated with

cardiometabolic risk parameters. Unlike expression of *Nnmt* in the liver or aorta, circulating NAM levels were not correlated with any clinical, lipid, glucose, or insulin traits, save for plasma HDL levels (Figure 3.7). This suggests that the circulating levels of the substrate nicotinamide are unlikely to significantly mediate effects on atherosclerosis.

To further examine the relationship of circulating NAM and atherosclerosis, we supplemented the drinking water of female *Ldlr-/-* mice with either NAM or β-NMN (500mg/kg/day) while consuming a Western style diet *ad libitum* for 12 weeks [33] (Figure 3.8A). This treatment did not significantly reduce lesion area, body mass, adiposity, or plasma glucose in the mice (Figures 3.8B, 3.8C, 3.8D). The β-NMN group had significantly reduced LDL and VLDL cholesterol after 12 weeks, while the nicotinamide group also trended towards a decrease (Figure 3.8E). The nicotinamide treatment group exhibited a higher level of plasma insulin, which may be due to slightly increased adiposity compared to control (Figures 3.8D and 3.8G). These results suggest that circulating NAD+ precursors may underlie changes in cholesterol and insulin homeostasis but not atherosclerosis.

Plasma levels of MNAM do not explain the effect of ASO knockdown on atherosclerosis.

The product of NNMT, MNAM, has been identified to be elevated in a number of pathologies, including vascular disease [10,30,31]. To test whether the MNAM directly mediates the effect of *Nnmt* on atherosclerosis, we incorporated MNAM into the diet as previously described, and fed *Ldlr-/-* mice *ad libitum* for 16 weeks [32] (Figure 3.9A). Because *Nnmt* knockdown decreased atherosclerosis and plasma MNAM, we hypothesized that the consumption of dietary MNAM would increase plasma MNAM levels and contribute to increased atherosclerosis. However, we observed that treated mice showed a modest reduction (33%, p=0.023) in lesion

area (Figure 3.9B). The mice on the MNAM diet were overall leaner after 16 weeks as quantified by average body mass and by adiposity (Figures 3.9C and 3.9D). We also observed that between the two groups, the average daily food intake per mouse was decreased on the MNAM diet, potentially underlying some of the metabolic and morphological differences compared to the control group (Figure 3.9E). There was no significant impact on plasma cholesterol, although there was a trend toward increased plasma glucose and decreased insulin (Figures 3.9F, 3.9G, and 3.9H).

Identifying tissues significantly impacted by *Nnmt* ASO.

We performed quantitative PCR analysis on 11 different tissues collected from chow-fed animals to assess basal levels of *Nnmt* expression. The tissues with the highest expression of *Nnmt* were liver, white adipose, brown adipose, and adrenal tissues (Figure 3.10A). Quantitative PCR was able to validate *Nnmt* knockdown in tissues with the highest expression such as liver and adipose but did not detect a significant change in expression within tissues with low basal expression such as peritoneal cells or skeletal muscle (Figure 3.10B).

. To test whether the ASO impacts expression in the vasculature, we flushed the inside of the dissected aorta of chow-fed animals with lysis buffer to collect RNA from the predominantly interior endothelial cell fraction [23]. Additionally, we homogenized the remaining aorta, which predominantly contained smooth muscle cells and fibroblasts, and separately, the adventitial fat surrounding the vessel to isolate from each fraction. By quantitative PCR analysis, *Nnmt* expression did not significantly decrease in all three vascular tissue fractions following five weeks of ASO treatment (Figure 3.10C).

Knockdown of *Nnmt* affects metabolic pathways in the liver.

As expected, we observed that *Nnmt* ASO knockdown led to a substantial decrease in NNMT protein compared to control in liver. As previously observed, *Nnmt* knockdown increased SIRT1protein in liver, and we observed that it also increased SIRT3 protein. (Figure 3.11A). SIRT1 is located in the nucleus and regulates transcription factors and nuclear receptors which are involved in lipid and glucose homeostasis. Of the known SIRT1 nuclear targets, we observed a significant 20-30% decrease in the expression of *Nr1h4*, which encodes the farnesoid-x-receptor, or FXR (Figure 3.11B). FXR regulates genes in the liver involved in bile acid synthesis, transfer, and uptake as well as influences the metabolism of carbohydrates and lipids [24]. To further investigate tissue-wide changes underlying the effects of ASO treatment, we performed RNA sequencing from whole liver tissue from mice treated with ASO for 16 weeks. Following differential expression analysis by DESeq2[25], we used WebGestalt [26] to annotated the differentially expressed genes (FDR < 0.05) into relevant gene ontology categories and mouse phenotype pathways. The most enriched category that was changed by ASO treatment was the 'epoxygenase P450 pathway', with 25-50% of the category members significantly downregulated by knockdown (Figures 3.11C and 3.11D). Genes in this category include the *Cyp2c* gene family as well as *Cyp2e1*, the main enzymes involved liver arachidonic acid metabolism [27]. Arachidonic acid is a membrane phospholipid that can be further metabolized into bioactive signaling molecules, called eicosanoids, which are known to be integral in in the inflammation and pathogenesis of vascular and liver diseases [28,29]. In addition to P450 enzymes, we also observed a significant downregulation of lipid and fatty acid metabolism pathways, including the *Acot* family of Acyl-CoA thioesterase genes. *Acot* genes are involved in mitochondrial trafficking of fatty acids *de novo* lipogenesis and gluconeogenesis.

Knockdown of either liver- or adipose-specific *Nnmt* expression does not confer resistance to atherosclerosis.

Nnmt is most strongly expressed in liver and adipose tissue, although under different regulatory control mechanisms. To determine if the observed impact of *Nnmt* inhibition derives from liver or adipose, we created adeno-associated virus (AAV) constructs designed to express shRNAs targeting *Nnmt* under the control of promoters specific to these tissues (thyroxine-binding globulin (TBG) for liver and adiponectin (ADP) for adipose tissue. C57BL/6J mice carrying human transgenes for ApoE-Leiden and CETP were injected with AAV at doses of ~3E12 genome equivalents of adipose-targeted AAV and ~2E12 genome equivalents of the liver targeted AAV). Control mice received AAV expressing shRNA for luciferase under the control of the same promoters. At two weeks post-injection, the mice were placed on the high fat, high cholesterol diet for an additional 15 weeks and then euthanized to collect tissues. (Figure 3.12A) The liver-specific shRNA AAV caused a ~35% reduction in females expression and a 60% reduction in males, while the adipose-specific caused a ~30% reduction in females and a 75% reduction in males (Figure 3.12B). While AAV shRNA knockdown of *Nnmt* expression was similar in degree to the knockdown seen with ASO, AAV shRNA knockdown showed no significant impact on lesion area (Figure 3.12C), plasma VLDL/LDL cholesterol (Figure 3.12F), plasma glucose (Figure 3.12G), or body weight (Figure 3.12D). Plasma metabolite analysis identified no significant changes in the levels of plasma NAM or MNAM, consistent with the hypothesis that both liver nor adipose play an essential role in modulating atherosclerosis through plasma metabolites (Figure 3.7).

We injected adipose- or liver-targeted AAV for *Nnmt* into a second murine model of atherosclerosis, LDL receptor null (*Ldlr-/-*) mice (Figure 3.13A). In this model, hepatic AAV shRNA knockdown again showed no significant impact on lesion area, plasma VLDL/LDL cholesterol, plasma triglycerides, or body weight (Figure 3.13B, 3.13C, 3.13D, and 3.13F). However, atherosclerotic lesion area and plasma VLDL/LDL cholesterol levels observed in control *Ldlr*-/- animals were significantly higher than those observed in the Leiden/CETP transgenic animals used for ASO experiments. Consequently, lesion area and plasma lipid traits may be less susceptible to modulation by hepatic *Nnmt* expression levels in *Ldlr*-/- animals.

However, AAV shRNA suppression of *Nnmt* expression in adipose tissue significantly decreased lesion area and plasma levels of VLDL/LDL cholesterol and triglycerides (Figures 3.13D and 3.13F). These results strongly suggested that modulation of *Nnmt* expression in adipose tissue may impact atherosclerosis and plasma lipids observed in ASO-treated mice, although as discussed above adipose Nnmt expression is unlikely to explain the chromosome 6 atherosclerosis association. The reduction in lesion area associated with AAV shRNA knockdown of *Nnmt* expression in adipose was much less than that seen in the ASO experiments, although the percent reduction in plasma cholesterol is similar (Figure 3.13B). This reduction may reflect the lesion area differences between *Ldlr*-/- animals and Leiden/CETP transgenic animals, or there may be other tissues that contribute to the response to ASO.

We performed mass-spectrometry based quantification of NNMT plasma metabolites from whole-body ASO and tissue-specific AAV *Nnmt* knockdown animals. While we observed that the adipose-AAV treated mice had similar increases in plasma NAM compared to ASO, the AAV-treated mice did not have the same extent of MNAM knockdown in the plasma (Figure

3.14). This suggests that the tissue-specific effect of the AAV on plasma lipids and metabolites is not as strong as the ASO.

Nnmt knockdown influences apoptosis and proliferation of inflammatory cells involved in lesion formation.

We were unable to recapitulate the magnitude of effect by ASO knockdown by tissue-specific genetic modulation or metabolite supplementation, so we hypothesized that the ASO mechanism exhibited local action in the aorta and directly influenced cells within the developing lesion, particularly macrophages. We performed immunohistochemistry on aortic root lesions from ASO-treated females to quantify the percentage of proliferating and apoptotic cells *in vivo* after 16 weeks of atherogenic diet, as previously described [34]. Three hours before sacrifice, we injected intraperitoneal EdU to label actively dividing cells within the plaque. After sacrifice, we stained aortic root sections with DAPI, anti-Cd68, and anti-EdU to identify all proliferating and non-proliferating macrophages. Post-imaging, we quantified the average percentage of EdU+ macrophages present in the lesion (Figure 3.15A). As an additional independent measurement of cellular proliferation, we stained a separate section with anti-Ki67 instead of EdU (Supplemental Figure 6B). To observe apoptosis in the aorta, we used TUNEL staining to identify cells undergoing apoptosis at the time of sacrifice (Figure 3.15C). After removing an outlier from the treatment group (Figure 3.16A), we identified a significant decrease in EdU+ Cd68+ cells by *Nnmt* knockdown (Figure 3.15B). Subsequently, we saw a trend towards a greater proportion of TUNEL+ macrophages in *Nnmt* treated sections (Figure 3.15D). These data suggest that the ASO has a direct effect on the proliferation of macrophages within the vessel wall.

Discussion

Human GWAS of hundreds of thousands of subjects have identified over 100 loci significantly associated with atherosclerosis, many containing well-known candidates and others containing only novel genes. In the latter instance, it has proved challenging to identify the causal gene and determine the mechanism involved, and altogether the identified loci explain a small fraction of disease heritability, indicating that many genetic factors remain to be identified [35]. We and others have sought to identify genes contributing to atherosclerosis using mouse animal models, which have the advantages that environmental factors can be controlled and relevant tissues can be studied [36]. We previously carried out a GWAS in a set of 100 diverse inbred strains of mice and identified a genetic locus on Chromosome 9 affecting atherosclerosis susceptibility in males and females. We selected *Nnmt* as a strong candidate and now report a functional analysis of its effects on atherosclerosis and related traits. Our results using *Nnmt* knockdown *in vivo* with an ASO suggest that *Nnmt* is a causal gene underlying the differences in susceptibility, exhibiting a very substantial 10-fold effect on lesion size in both males and females. The effect does not appear to be mediated by circulating levels of NAM, the substrate of the enzyme, or MNAM, the product.. There was a significant reduction in LDL/VLDL levels, but the effect was very modest in males. Tissue specific knockdown of the enzyme in liver or adipose had modest effects on lesion development. We conclude that NNMT expression in another cell type relevant to atherosclerosis is primarily responsible.

Nnmt was chosen as a high priority candidate at the chromosome 9 locus since its expression varied considerably across the HMDP strains and was regulated in the liver by a local cis-eQTL, and its expression levels correlated with atherosclerosis. Conditioning on liver *Nnmt* levels significantly reduced the association of atherosclerosis of the chromosome 9

locus but did not eliminate it, suggesting that there may be additional genetic variation at the locus affecting atherosclerosis. In this regard, we note that there was substantial overall variation in lesion development across the HMDP strains (well over 100-fold) and that the significant association loci explain a tiny fraction of this overall variance, consistent with the existence of many, perhaps hundreds, of underlying genes, most with very modest effects [6]. This polygenicity is similar to the genetic architecture of CAD susceptibility in human populations [1].

ASO knockdown in hyperlipidemic mice revealed a dramatic, approximately 10-fold suppression of aortic lesions and accompanied a decrease of about 30-40 percent in plasma VLDL/LDL cholesterol levels. Lipoprotein secretion, synthesis, and uptake were not significantly affected, suggesting that the decrease in LDL/VLDL-cholesterol was due to reduced clearance. It is unlikely that the reduction in LDL/VLDL-cholesterol was entirely responsible for the dramatic decrease in atherosclerosis in ASO-treated mice. Because the liver plays the dominant role in VLDL production, we anticipated that liver-specific knockdown of *Nnmt* might produce a similar reduction in the production of plasma VLDL/LDL cholesterol, but we did not observe this reduction. System-wide knockdown of *Nnmt* also reduced obesity in atherogenic mice, but knockdown in adipose specifically did not significantly affect adiposity or plasma glucose. One hypothesis we explored to explain the differences between whole-body ASO and tissue specific AAV was the extent to which genetic manipulation across multiple or singular tissues influenced levels of circulating NAM and MNAM. Plasma metabolite analysis identified significant downregulation of plasma NAM and MNAM by ASO but did not find the same extent of change when knockdown occurred in either liver or adipose.

Variation in the levels of local and circulating nicotinamide influence the levels of circulating NAD+ and NADP+. Here, we validated a previously reported mechanistic decrease

of SIRT1, a NAD+ dependent deacetylase, in the liver by *Nnmt* ASO. Our data is the first to report the levels of SIRT1 following ASO treatment under atherogenic conditions. Knocking down *Nnmt* increased the levels of nicotinamide, thereby promoting the degradation of SIRT1. The expression of SIRT1 nuclear receptor target genes, such as FXR, was also additionally significantly downregulated in *Nnmt* ASO treated animals. The enrichment of P450 enzymes in significantly downregulated genes provide further evidence of downstream changes due to fluctuations in liver NADP+ levels as caused by ASO. The ASO exhibits a significant effect on homeostatic mechanisms in the liver, shown here to be mediated by nuclear and mitochondrial sirtuins, and P450 enzymes which collectively influence everything from cell division to inflammation and gluconeogenesis.

There is previous evidence that NNMT, NAM, and MNAM may impact cardiovascular disease. Liu *et al*. found higher levels of circulating MNAM, the product of NNMT, in patients with cardiovascular disease [10]. Previous studies found that plasma levels of MNAM increased in mice with atherosclerosis and administration of MNAM to *Ldlr*/*Apo*e double knockout mice suppressed lesion formation [32]. Jiang *et al*. report a dose-dependent decrease in lesion area of ApoE-deficient mice in response to MNAM in the diet [30,37]. Our findings in feeding MNAM to hyperlipidemic mice suggest that MNAM is not pro-atherogenic and is likely to be protective, consistent with recently reported results, although we note that its inclusion in the diet reduced food intake and body fat [32] . Additional *in vitro* studies in peritoneal macrophages suggest that MNAM could work as an antioxidant and inhibit ROS production, directly altering immune phenotypes associated with atherosclerosis [38].

Similar mechanistic studies to understand MNAM function have been conducted to investigate the role of NAM in protection against atherosclerosis. NAM administration to

Ldlr/Apoe double knockout mice was protective against lesion development with a two-fold reduction in lesion area, whereas treatment of NAM or β- NMN in our humanized hyperlipidemic mouse model did not significantly impact lesion area size [38]. The mouse model used by Mateuszuk et al. was not fed a high fat high cholesterol diet but instead was genetically predisposed to spontaneous plaque development. The authors also reported no change in plasma cholesterol with NAM treatment postulating that NAM does not affect lesions area through altering plasma lipids. We did observe a decrease in plasma LDL and VLDL cholesterol with β-NMN treatment, suggesting that circulating NAD+ precursors may in part influence cholesterol homeostasis via biogenesis and metabolic pathways in the liver.

Taken together, the AAV- and metabolite supplementation studies showed that the effect of the *Nnmt* ASO could not be reduced to function in a singular tissue, nor was the effect predominantly mediated by levels of circulating metabolites. We hypothesized that the ASO exerted an effect on proliferation and apoptosis of cells within the lesion, directly impacting the severity and progression of atherosclerosis [34]. Quantification of proliferative and apoptotic markers in lesion sections identified lesions of *Nnmt* ASO treated mice exhibited reduced macrophage proliferation and increased apoptosis. The specific mechanism underlying the ASO effect on the proliferation of macrophages remains unknown. One hypothesis is that the ASO directly affects the survival of macrophages in the lesion. Despite low basal expression of *Nnmt* in the vascular tissues under chow conditions, we could not rule out that the ASO was influencing the expression of *Nnmt* within cells during the development of the plaque. An additional hypothesis could be that the ASO has a direct effect on the vascular cells of the aorta. We plan to perform immunostaining for NNMT in lesions from ASO treated mice to explore the localization of NNMT expression in the cell types of the aorta.

Figures

Figure 3.1. *Nnmt* is a candidate gene at a locus on chromosome 9 associated with atherosclerotic lesion area. (A) Manhattan plot of the p-values associated with lesion area in females across the Atherosclerosis HMDP. (B) Locus Zoom view of the associated region on chromosome 9. (C) Heat map depicting the bicor coefficient between *Nnmt* transcript levels and clinical traits in the Atherosclerosis HMDP. * p-value $\leq$ 0.05, **p-value $\leq$ 0.01, ***p-value $\leq$ 0.001

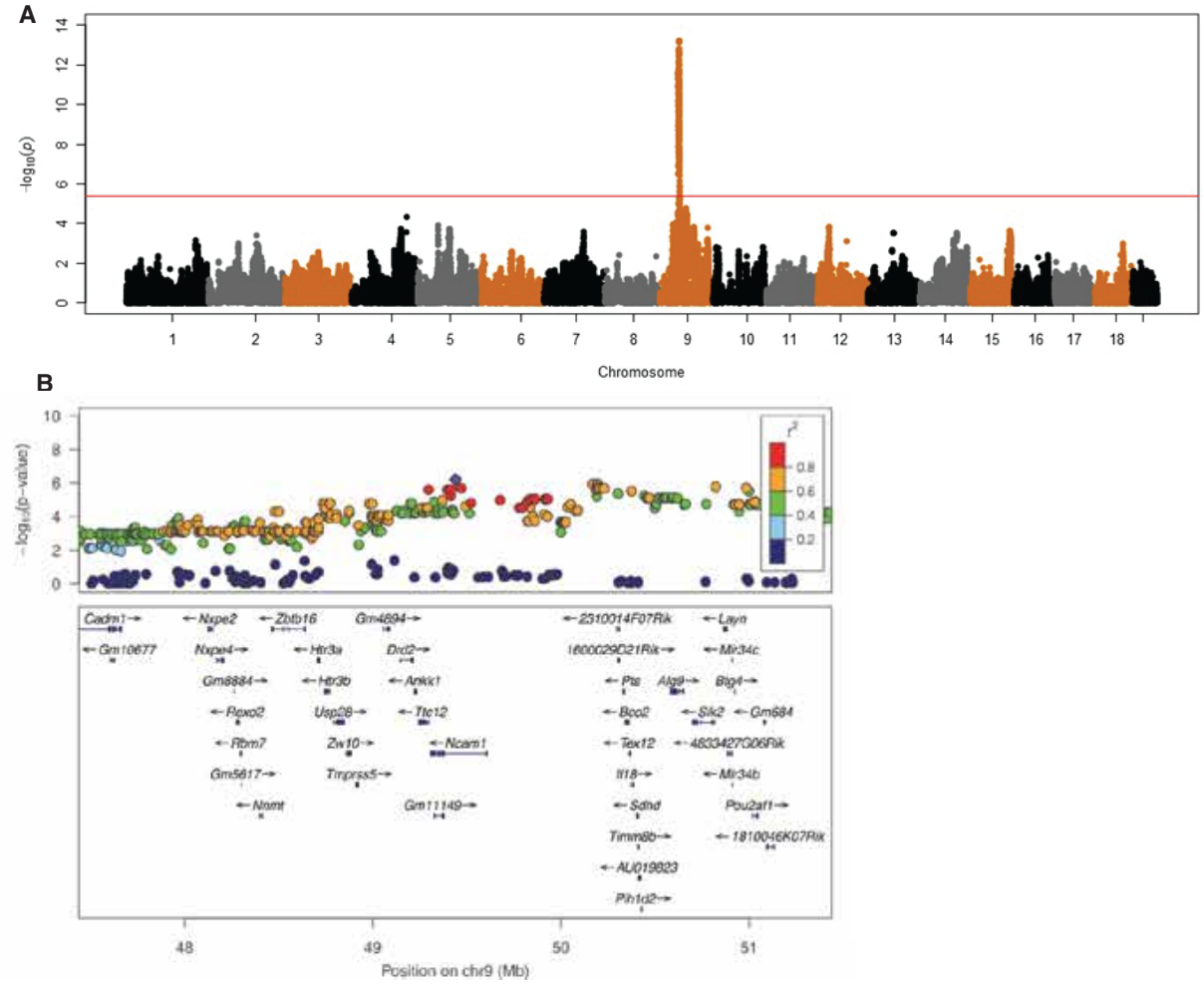

Figure 3.2. Knockdown of *Nnmt* by ASO decreases atherosclerosis and lowers plasma lipids. (A) Hyperlipidemic C57BL/6J.*Apoe*-Leiden, human CETP transgenic mice were treated with an *Nnmt* or control ASO for 16 weeks. (B) Expression of *Nnmt* in liver and adipose tissues in male (M-) or female (F-) mice treated with ASO. (C and D) Aortic lesion area in females and males was measured at 60 μm intervals beginning the base of the tricuspid valve. Average lesion area over a total distance of 540μm. (E) After CD68 and αS.M.A. staining, plaque composition did not appear to differ by *Nnmt* ASO treatment. (F) Body mass changes between *Nnmt* and control ASO groups. (G) Adiposity as determined by the proportion of gonadal fat mass to total mass. (H) Liver mass was increased in *Nnmt* ASO treated animals when normalized to total body weight. (I and J) This increase was not explained by increases in liver TG or total cholesterol.

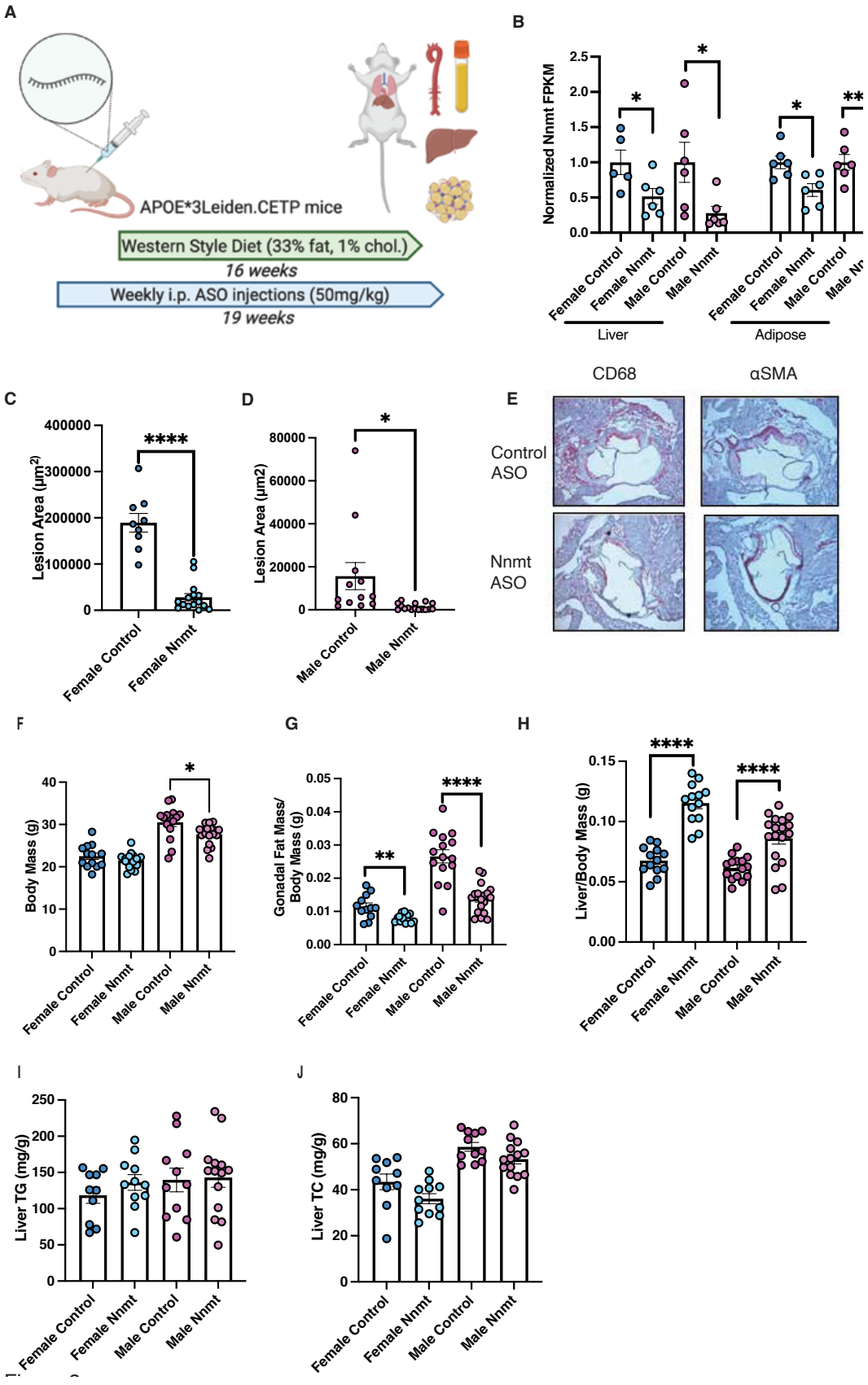
A
APOE*3Leiden.CETP mice
Western Style Diet (33% fat, 1% chol.)
16 weeks
Weekly i.p. ASO injections (50mg/kg)
19 weeks
B
Normalized Nnmt FPKM
Female Control
Female Nnmt
Male Control
Male Nnmt
Liver
Adipose
C
Lesion Area (µm²)
Female Control
Female Nnmt
D
Lesion Area (µm2)
Male Control
Male Nnmt
E
CD68
αSMA
Control ASO
Nnmt ASO
F
Body Mass (g)
G
Gonadal Fat Mass/ Body Mass (g)
H
Liver/Body Mass (g)
I
Liver TG (mg/g)
J
Liver TC (mg/g)

Figure 3.3. Genetic evidence for cis-regulation of *Nnmt* in liver and aorta. (A) The x-axis represents the variance in *Nnmt* expression that is explained by the lead SNP on chromosome 9, rs33700043. The y-axis represents the number of transcripts that are significantly correlated (p≤1E-4) with *Nnmt* in the same tissue. (B and C) Correlations between lesion area and the cis-component of *Nnmt* expression in aorta and liver from the atherosclerosis HMDP.

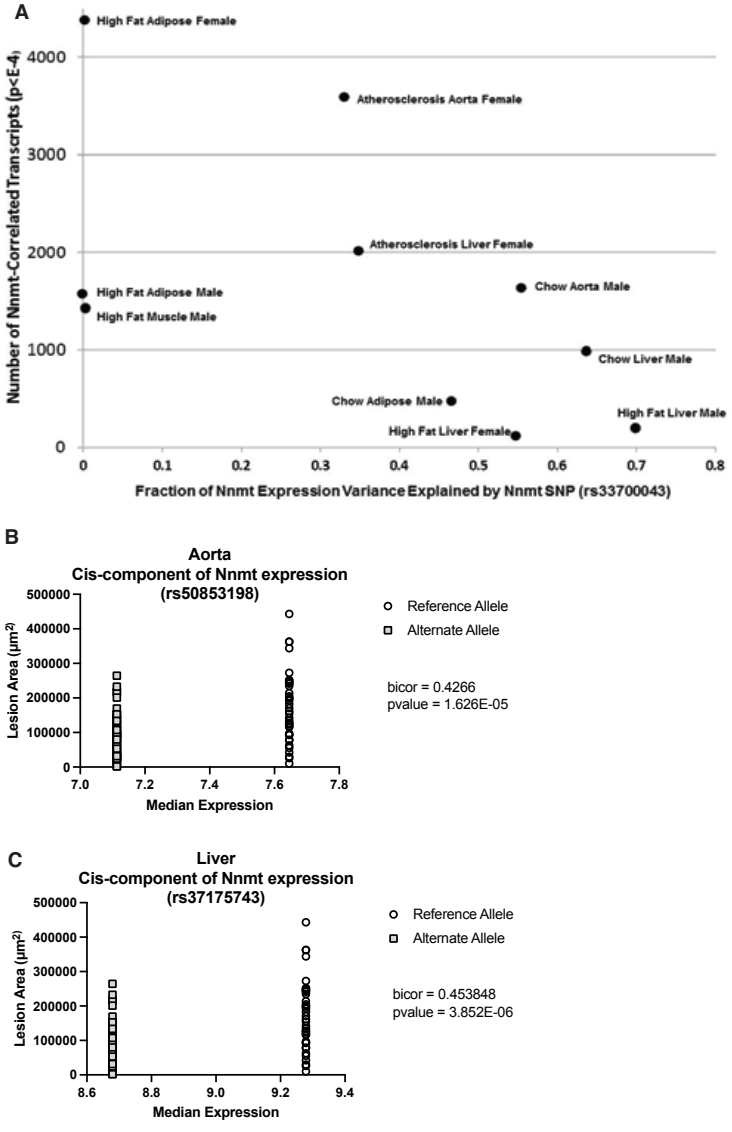

Figure 3.4. Correlations of *Nnmt* expression and clinical traits in the atherosclerosis HMDP. Heat map depicting the bicor coefficient between *Nnmt* transcript levels and clinical traits in the Atherosclerosis HMDP. * p-value $\leq$ 0.05, **p-value $\leq$ 0.01, ***p-value $\leq$ 0.001

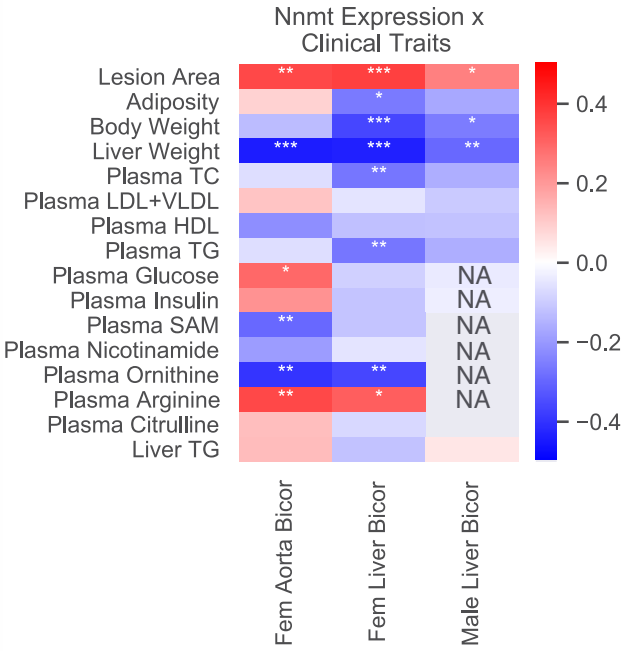

Figure 3.5. Gene expression correlations in the HMDP. The expression of *Nnmt* was correlated with the expression of genes in pathways that are relevant to atherosclerosis, methylation, N.A.D. metabolism, and mitochondrial function (A). The correlation of *Sirt1* and *Sirt3* gene expression with clinical traits and metabolic transcription factors (B). The correlation of the plasma levels of NNMT substrate, NAM, with (C) clinical traits suggest that nicotinamide is not correlated with lesion area in the Ath HMDP. * p-value $\leq$ 0.05, **p-value $\leq$ 0.01, ***p-value $\leq$ 0.001

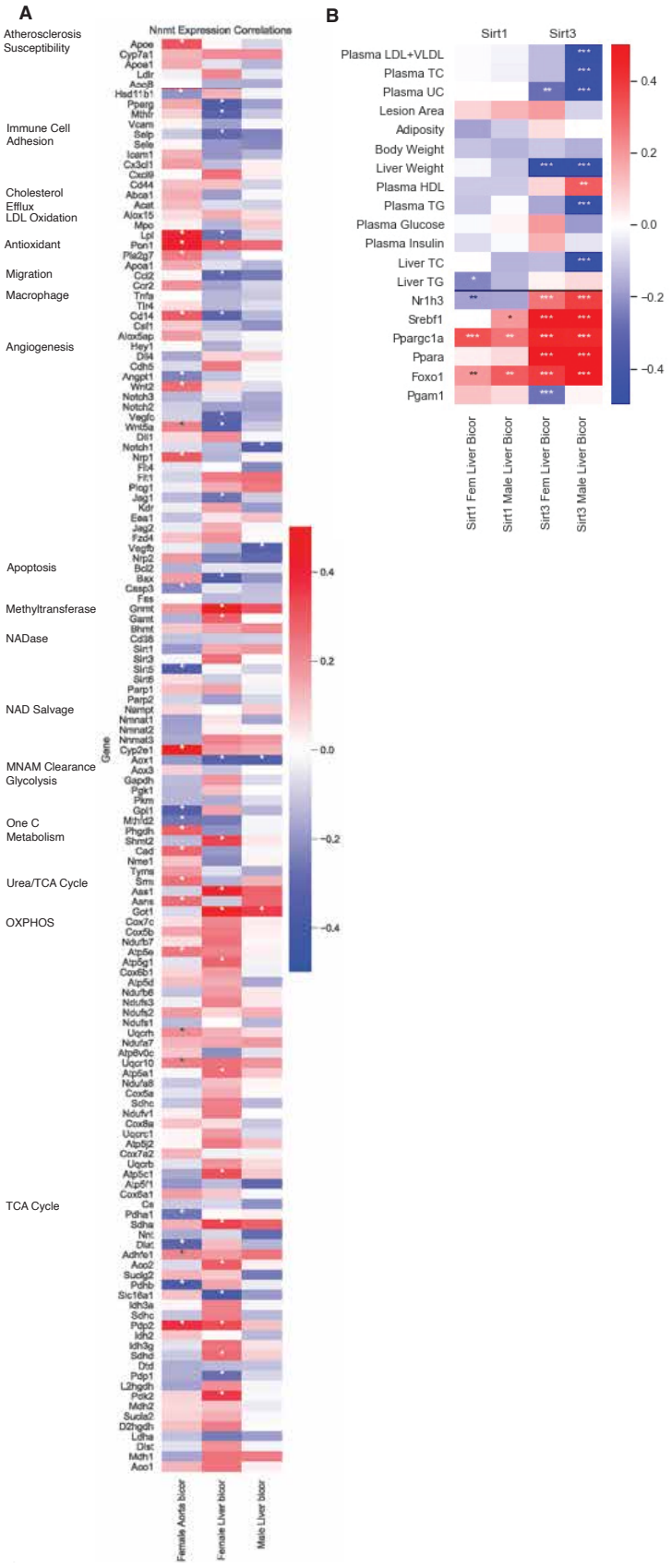
A
Nnmt Expression Correlations
Atherosclerosis Susceptibility
Immune Cell Adhesion
Cholesterol Efflux
LDL Oxidation
Antioxidant
Migration
Macrophage
Angiogenesis
Apoptosis
Methyltransferase
NADase
NAD Salvage
MNAM Clearance
Glycolysis
One C Metabolism
Urea/TCA Cycle
OXPHOS
TCA Cycle
Gene
Female Aorta bicor
Female Liver bicor
Male Liver bicor
0.4
0.2
0.0
−0.2
−0.4
B
Sirt1
Sirt3
Plasma LDL+VLDL
Plasma TC
Plasma UC
Lesion Area
Adiposity
Body Weight
Liver Weight
Plasma HDL
Plasma TG
Plasma Glucose
Plasma Insulin
Liver TC
Liver TG
Nr1h3
Srebf1
Ppargc1a
Ppara
Foxo1
Pgam1
Sirt1 Fem Liver Bicor
Sirt1 Male Liver Bicor
Sirt3 Fem Liver Bicor
Sirt3 Male Liver Bicor
0.4
0.2
0.0
−0.2
−0.4

Figure 3.6. Effect of *Nnmt* expression knockdown on metabolic traits.

Mass spectrometry analysis of plasma metabolites showed an increase in the NNMT substrate nicotinamide (A) and decrease in metabolite methylnicotinamide(B). *Nnmt* knockdown had a significant effect on plasma insulin (D) but not glucose (C). Measurements of plasma ApoB containing lipoproteins (E and F) Gel filtration chromatography analysis of plasma lipoproteins in females for total cholesterol (G).

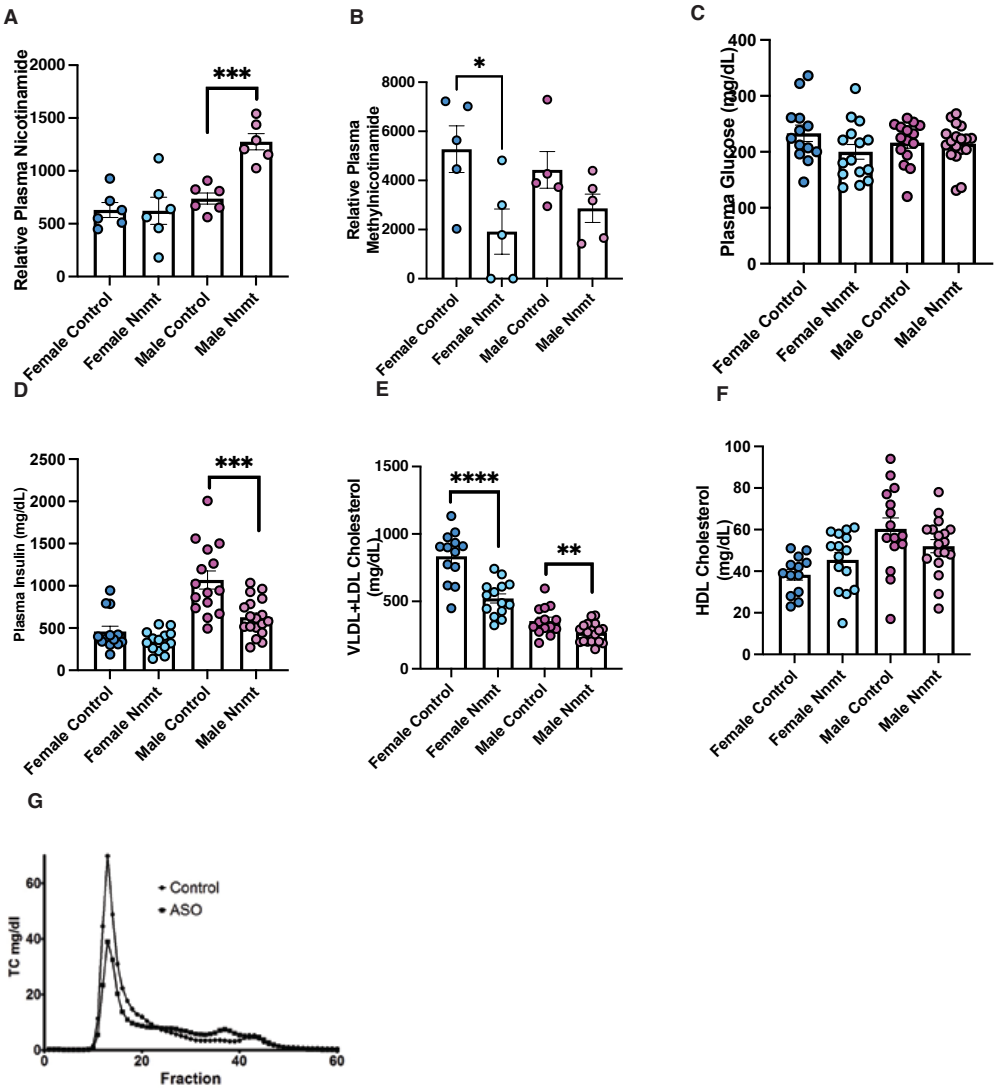

Figure 3.7. Plasma nicotinamide correlations in the HMDP. The expression of *Nnmt* was correlated with plasma nicotinamide measurements suggest that circulating nicotinamide is not correlated with lesion area in the Ath HMDP.

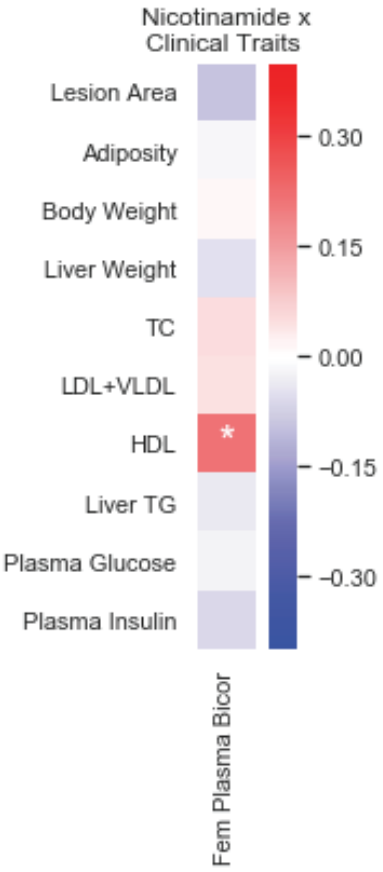

Figure 3.8. NAM supplementation in drinking water. (A) Female *Ldlr-/-* mice were supplemented with NAD+ precursors, NAM and β-NMN via drinking water (500mg/kg/day) for 14 weeks concurrent with a 12 week Western-style diet. (B-F) Drinking water supplementation did not reduce lesion area, body mass, adiposity, or plasma glucose. (D) Average LDL and VLDL cholesterol values were decreased by β-NMN. (G) NAM treatment significantly increased the levels of plasma insulin.

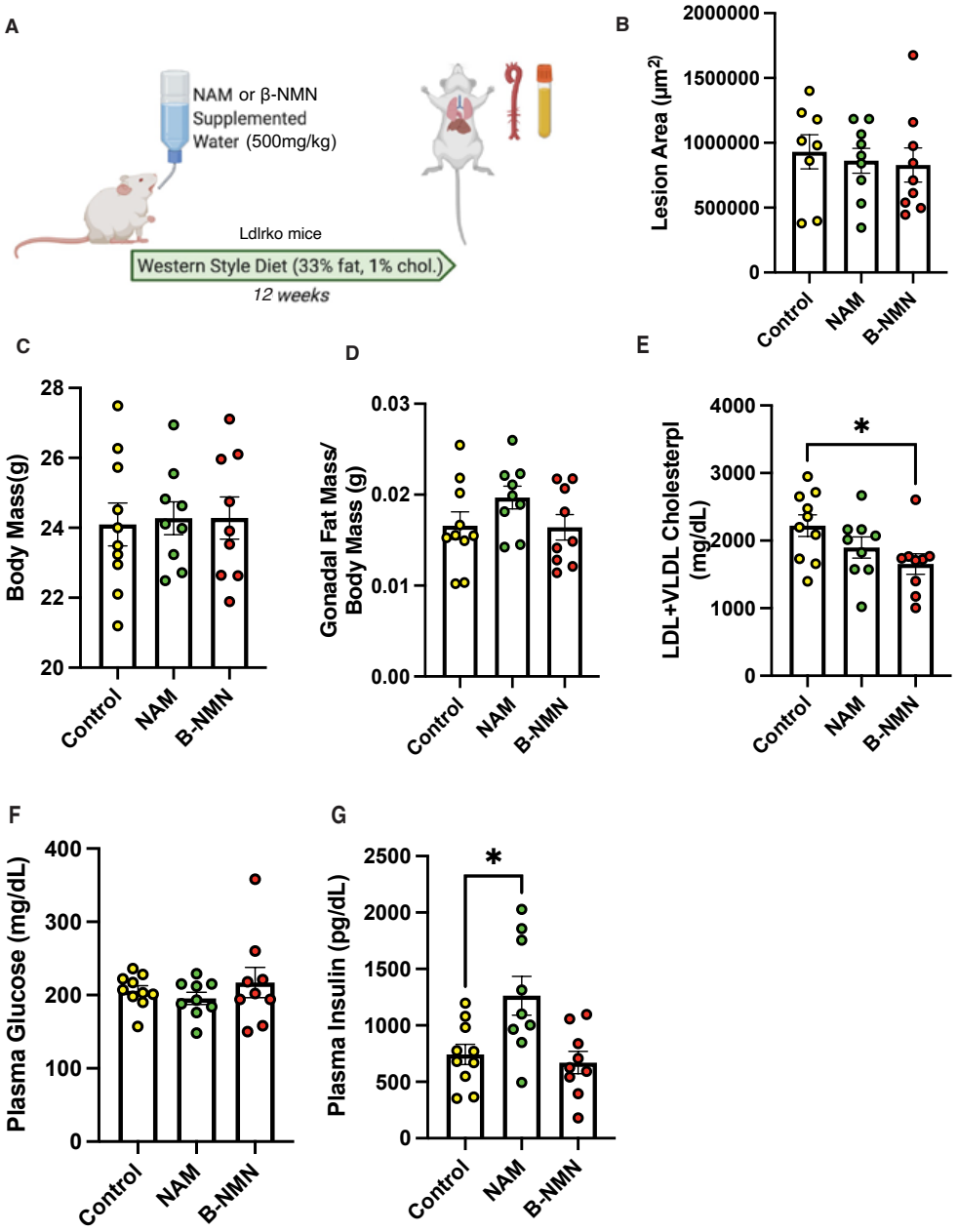
A
NAM or β-NMN
Supplemented
Water (500mg/kg)
Ldlrko mice
Western Style Diet (33% fat, 1% chol.)
12 weeks
B
Lesion Area (µm²)
2000000
1500000
1000000
500000
0
Control
NAM
B-NMN
C
Body Mass(g)
28
26
24
22
20
D
Gonadal Fat Mass/ Body Mass (g)
0.03
0.02
0.01
0.00
E
LDL+VLDL Cholesterpl (mg/dL)
4000
3000
2000
1000
0
*
F
Plasma Glucose (mg/dL)
400
300
200
100
0
G
Plasma Insulin (pg/dL)
2500
2000
1500
1000
500
0
*

Figure 3.9. Effect of exogenous dietary MNAM on atherosclerotic lesion area. (A) Male *Ldlr*-/-animals were fed a Western style diet containing 1% MNAM. (B) Average lesion area per histological section were modestly reduced compared with controls receiving Western diet without MNAM. (C-E) Body mass, adiposity, and average daily food intake were decreased by MNAM feeding. (F-H) Plasma VLDL + LDL was unchanged although there was a trend toward increased glucose ($p=0.0922$) and decreased insulin ($p= 0.0763$).

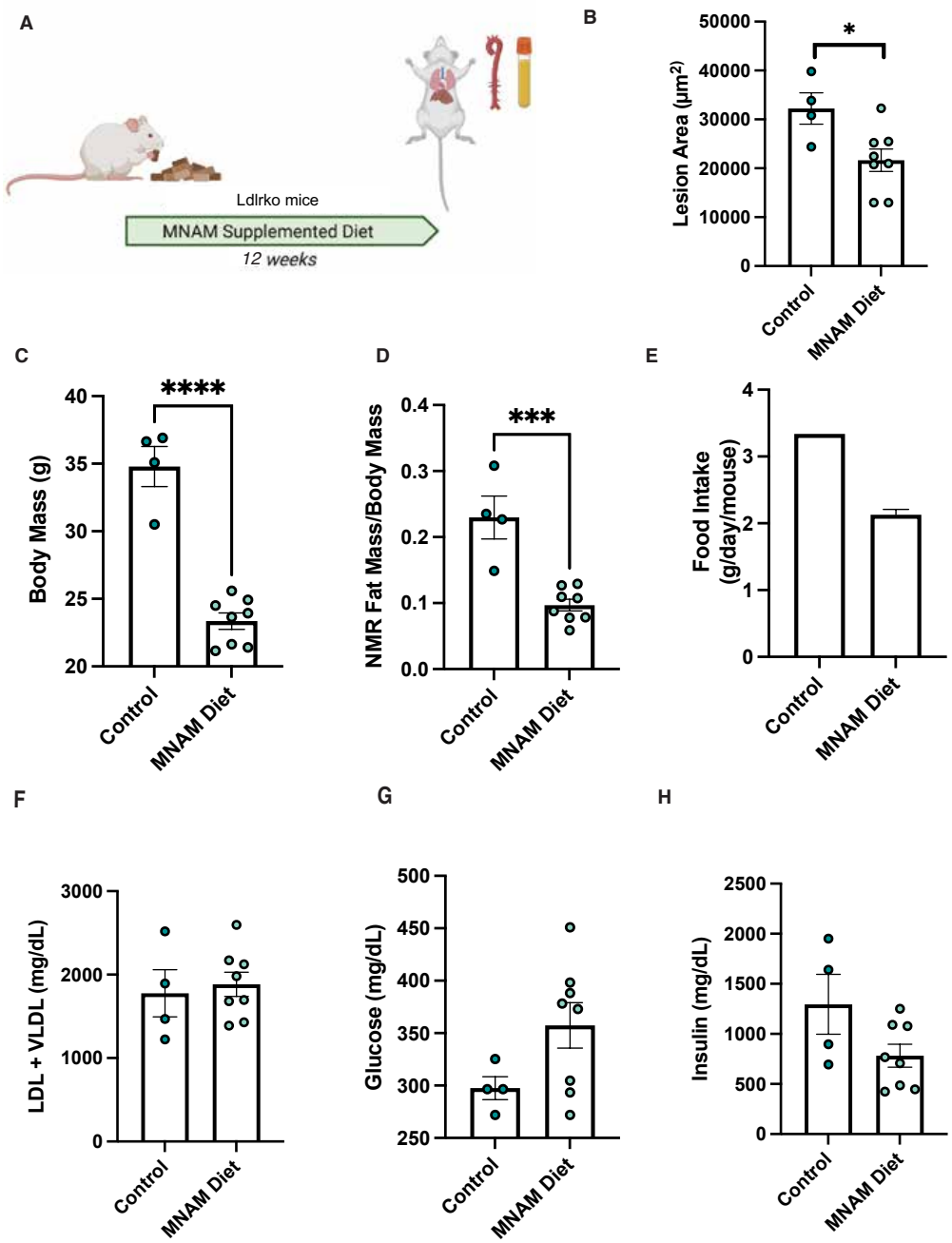
A
Ldlrko mice
MNAM Supplemented Diet
12 weeks
B
Lesion Area (μm²)
50000
40000
30000
20000
10000
0
*
Control
MNAM Diet
C
Body Mass (g)
40
35
30
25
20
****
Control
MNAM Diet
D
NMR Fat Mass/Body Mass
0.4
0.3
0.2
0.1
0.0
***
Control
MNAM Diet
E
Food Intake (g/day/mouse)
4
3
2
1
0
Control
MNAM Diet
F
LDL + VLDL (mg/dL)
3000
2000
1000
0
Control
MNAM Diet
G
Glucose (mg/dL)
500
450
400
350
300
250
Control
MNAM Diet
H
Insulin (mg/dL)
2500
2000
1500
1000
500
0
Control
MNAM Diet

Figure 3.10 *Nnmt* ASO knockdown. (A) Expression of *Nnmt* by qPCR across 11 tissues in chow-fed conditions. (B) The expression of *Nnmt* by qPCR following 16 weeks ASO treatment in adipose, liver, peritoneal macrophages, and gastrocnemius. 5 weeks of IP Nnmt ASO injections does not significantly decrease gene expression in aortic adventitia, smooth muscle cells, or endothelial cells. Female mice (n=6/treatment) were injected weekly with either control or *Nnmt* ASO Isolated aortas were flushed with Qiazol and pooled (n=3 animals/sample; 2 samples/treatment). Adventitia and the aorta post-flush were homogenized in Qiazol and pooled (n=2 mice/sample; 3 samples/treatment). *Nnmt* gene expression was normalized to the geometric mean of Eif2a and Rpl13a. (C) Paired two-tailed t-tests were performed between groups to test for statistical significance. (D) Correlations between plasma LDL+VLDL levels and lesion area in control- and *Nnmt*- ASO treated animals.

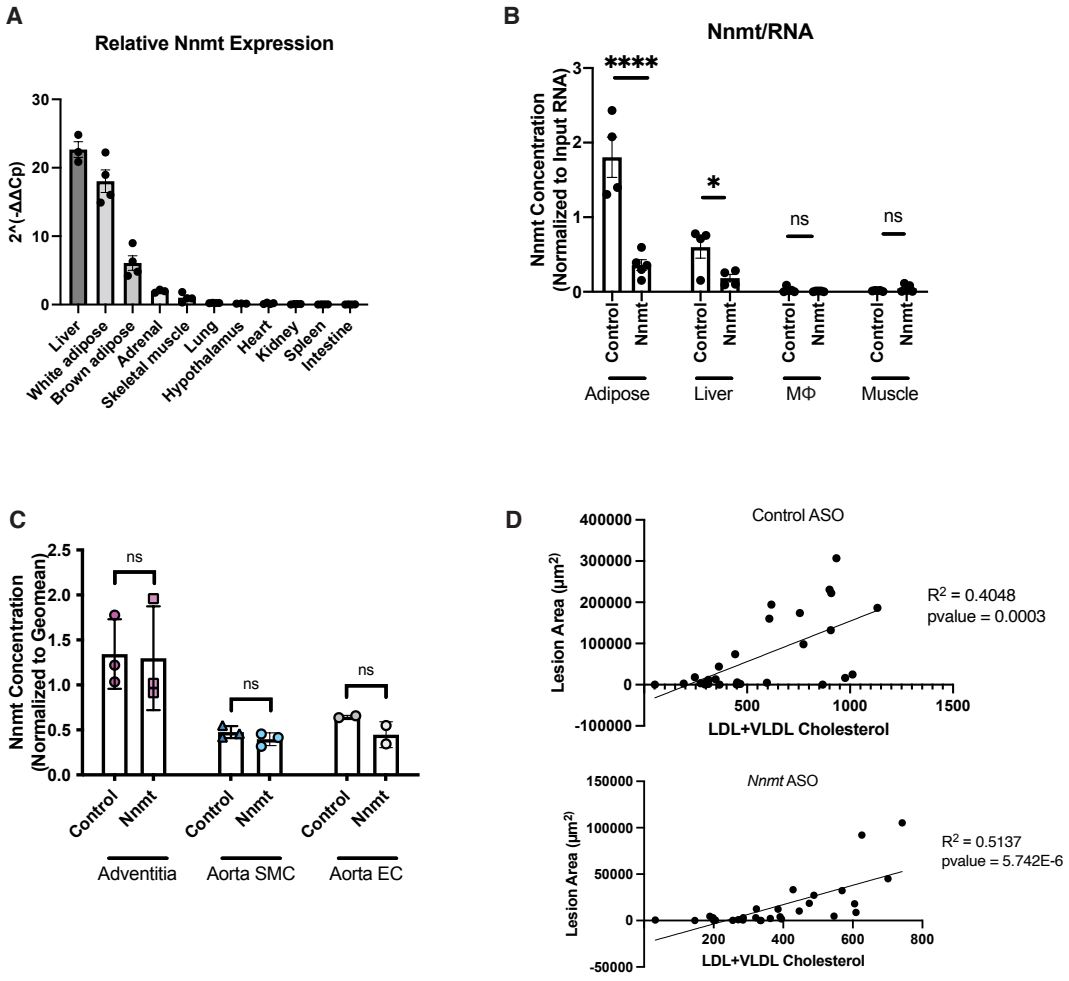
A
Relative Nnmt Expression
2^(-ΔΔCp)
Liver
White adipose
Brown adipose
Adrenal
Skeletal muscle
Lung
Hypothalamus
Heart
Kidney
Spleen
Intestine
B
Nnmt/RNA
Nnmt Concentration (Normalized to Input RNA)
****
*
ns
ns
Control
Nnmt
Adipose
Liver
MΦ
Muscle
C
Nnmt Concentration (Normalized to Geomean)
ns
ns
ns
Adventitia
Aorta SMC
Aorta EC
D
Control ASO
Lesion Area (μm²)
R² = 0.4048
pvalue = 0.0003
LDL+VLDL Cholesterol
Nnmt ASO
R² = 0.5137
pvalue = 5.742E-6

Figure 3.11. ASO mechanisms in the liver. (A) Western blots for NNMT, SIRT1, SIRT3, and B-actin in the livers of ASO treated females. (B) Heatmap of the log2 fold change in *Sirt1* target genes by *Nnmt* ASO. (C and D) WebGestalt enrichment of transcripts differentially regulated by *Nnmt* knockdown. Enrichment ratios, which represent the number of genes per annotation observed in the data divided by the number expected by chance from the annotation set using an FDR. is shown on the x-axis. Annotation terms are shown on the y-axis, followed by the number of observed transcripts in the data and the total number of transcripts included in the annotation gene set FDR values are reported on the bar for each respective term.

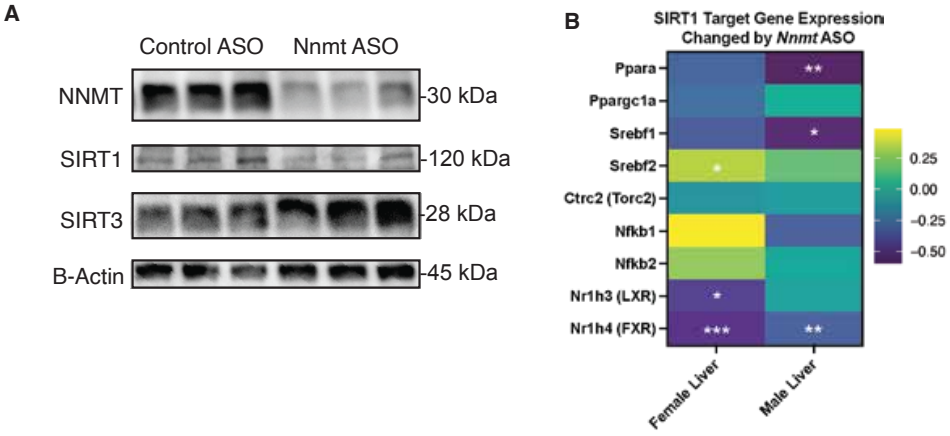
A
Control ASO
Nnmt ASO
NNMT
SIRT1
SIRT3
B-Actin
30 kDa
120 kDa
28 kDa
45 kDa
B
SIRT1 Target Gene Expression
Changed by Nnmt ASO
Ppara
Ppargc1a
Srebf1
Srebf2
Ctrc2 (Torc2)
Nfkb1
Nfkb2
Nr1h3 (LXR)
Nr1h4 (FXR)
0.25
0.00
−0.25
−0.50
Female Liver
Male Liver

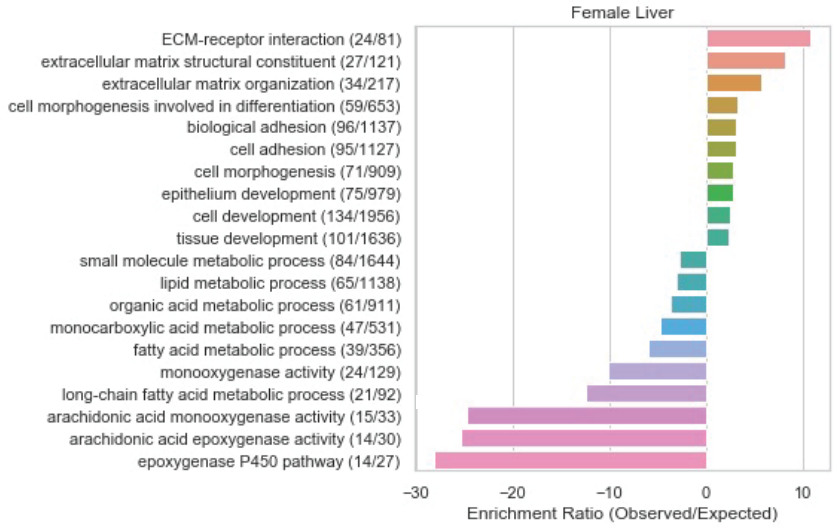
C
Female Liver
ECM-receptor interaction (24/81)
extracellular matrix structural constituent (27/121)
extracellular matrix organization (34/217)
cell morphogenesis involved in differentiation (59/653)
biological adhesion (96/1137)
cell adhesion (95/1127)
cell morphogenesis (71/909)
epithelium development (75/979)
cell development (134/1956)
tissue development (101/1636)
small molecule metabolic process (84/1644)
lipid metabolic process (65/1138)
organic acid metabolic process (61/911)
monocarboxylic acid metabolic process (47/531)
fatty acid metabolic process (39/356)
monooxygenase activity (24/129)
long-chain fatty acid metabolic process (21/92)
arachidonic acid monooxygenase activity (15/33)
arachidonic acid epoxygenase activity (14/30)
epoxygenase P450 pathway (14/27)
−30
−20
−10
0
10
Enrichment Ratio (Observed/Expected)

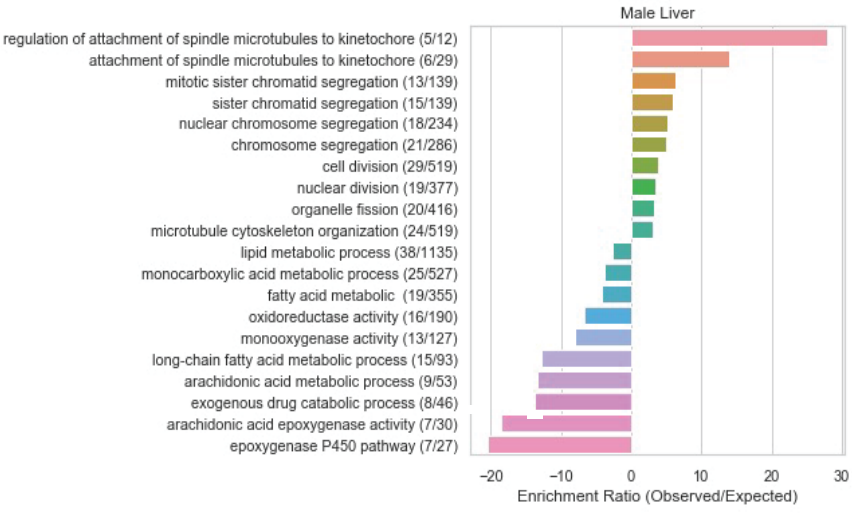
D
Male Liver
regulation of attachment of spindle microtubules to kinetochore (5/12)
attachment of spindle microtubules to kinetochore (6/29)
mitotic sister chromatid segregation (13/139)
sister chromatid segregation (15/139)
nuclear chromosome segregation (18/234)
chromosome segregation (21/286)
cell division (29/519)
nuclear division (19/377)
organelle fission (20/416)
microtubule cytoskeleton organization (24/519)
lipid metabolic process (38/1135)
monocarboxylic acid metabolic process (25/527)
fatty acid metabolic (19/355)
oxidoreductase activity (16/190)
monooxygenase activity (13/127)
long-chain fatty acid metabolic process (15/93)
arachidonic acid metabolic process (9/53)
exogenous drug catabolic process (8/46)
arachidonic acid epoxygenase activity (7/30)
epoxygenase P450 pathway (7/27)
−20
−10
0
10
20
30
Enrichment Ratio (Observed/Expected)

Figure 3.12. Tissue-specific AAV knockdown of *Nnmt.* (A) Apoe*Leiden mice were treated with AAV and fed a western style diet for 15 weeks. (B) Apoe*Leiden mice receiving AAV expressing liver- or adipose- directed shRNA for *Nnmt* showed about a 50% reduction in Nnmt mRNA levels compared to mice receiving control virus expressing shRNA for luciferase. (C-E) Atherosclerotic lesion area, body mass, and adiposity were unaffected. (F and G) Plasma VLDL+LDL cholesterol and glucose were also not changed by liver- or adipose- knockdown of *Nnmt*.

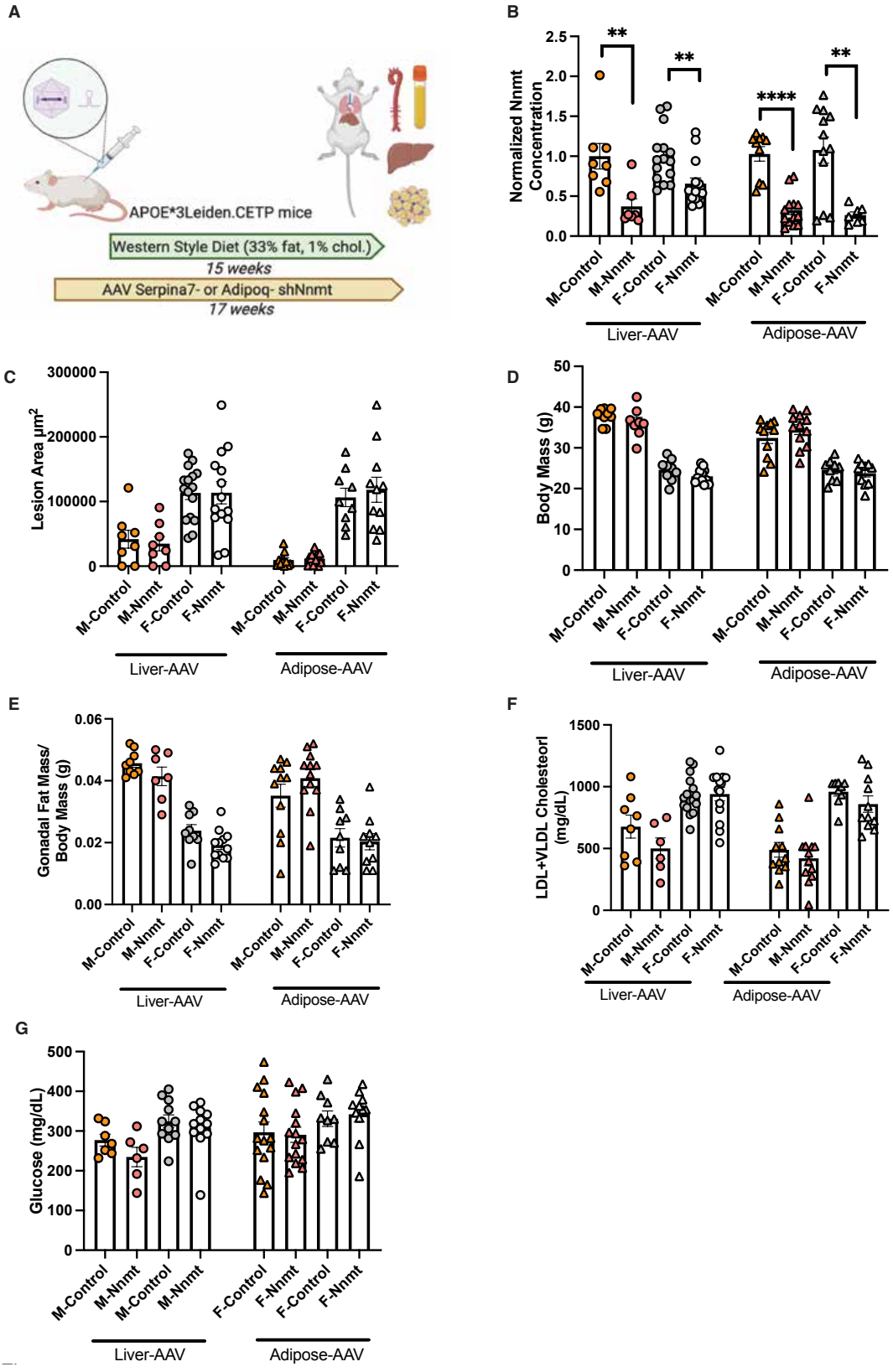
A
APOE*3Leiden.CETP mice
Western Style Diet (33% fat, 1% chol.)
15 weeks
AAV Serpina7- or Adipoq- shNnmt
17 weeks
B
Normalized Nnmt Concentration
2.5
2.0
1.5
1.0
0.5
0.0
**
**
****
**
M-Control
M-Nnmt
F-Control
F-Nnmt
Liver-AAV
Adipose-AAV
C
Lesion Area µm2
300000
200000
100000
0
D
Body Mass (g)
50
40
30
20
10
0
E
Gonadal Fat Mass/ Body Mass (g)
0.06
0.04
0.02
0.00
F
LDL+VLDL Cholesterol (mg/dL)
1500
1000
500
0
G
Glucose (mg/dL)
500
400
300
200
100
0

Figure 3.13. *Ldlr-/-* AAV experiments. (A) *Nnmt* expression in knockdown target tissues. (B) Lesion area. (C) Body mass. (D-F) Plasma VLDL+LDL, HDL, and TG.

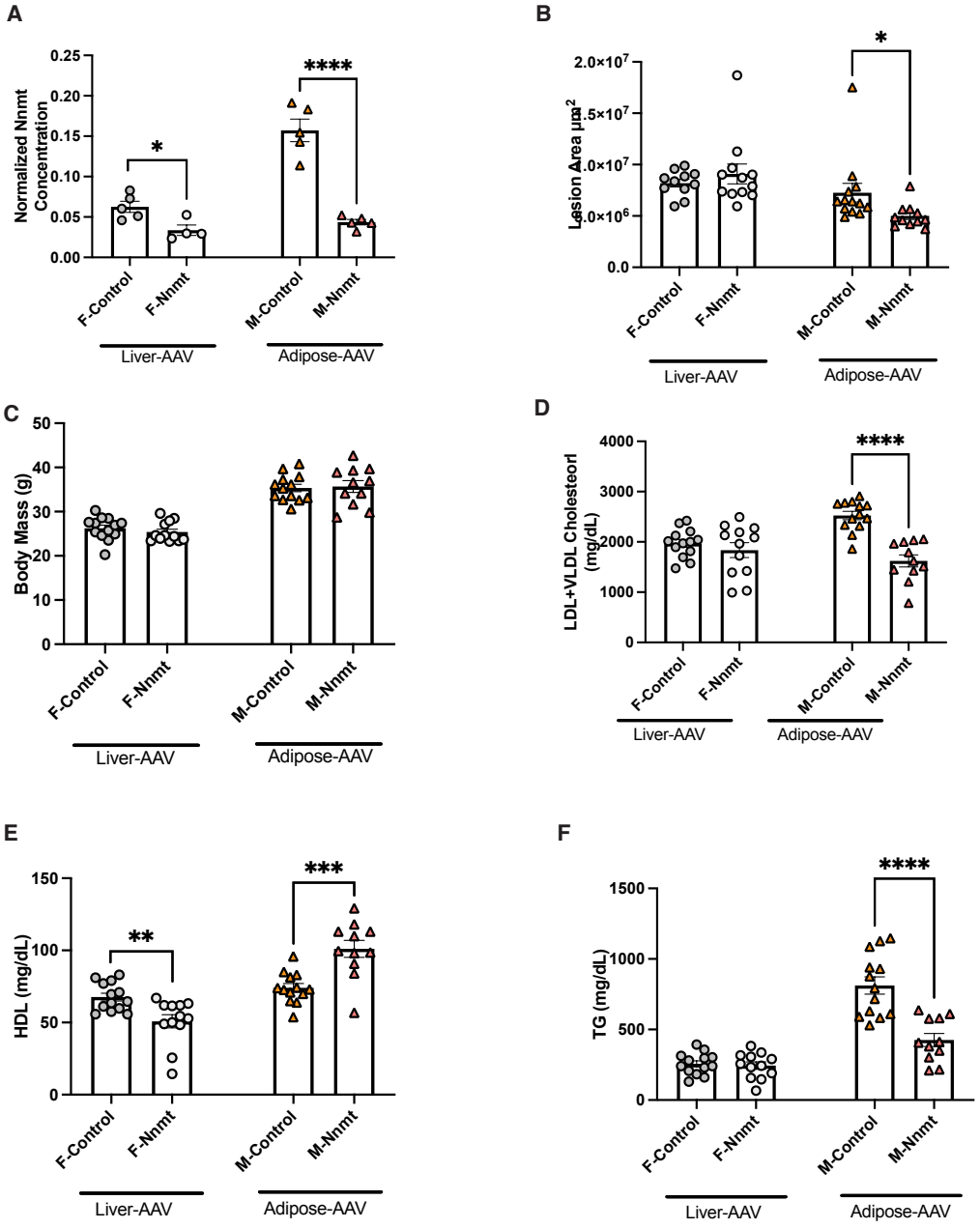

Figure 3.14. Plasma metabolites in ASO vs. tissue specific AAV. Relative plasma concentrations of nicotinamide (A) and methylnicotinamide (B) in ASO vs. liver- and adipose-specific AAV knockdown CETP-Leiden females.

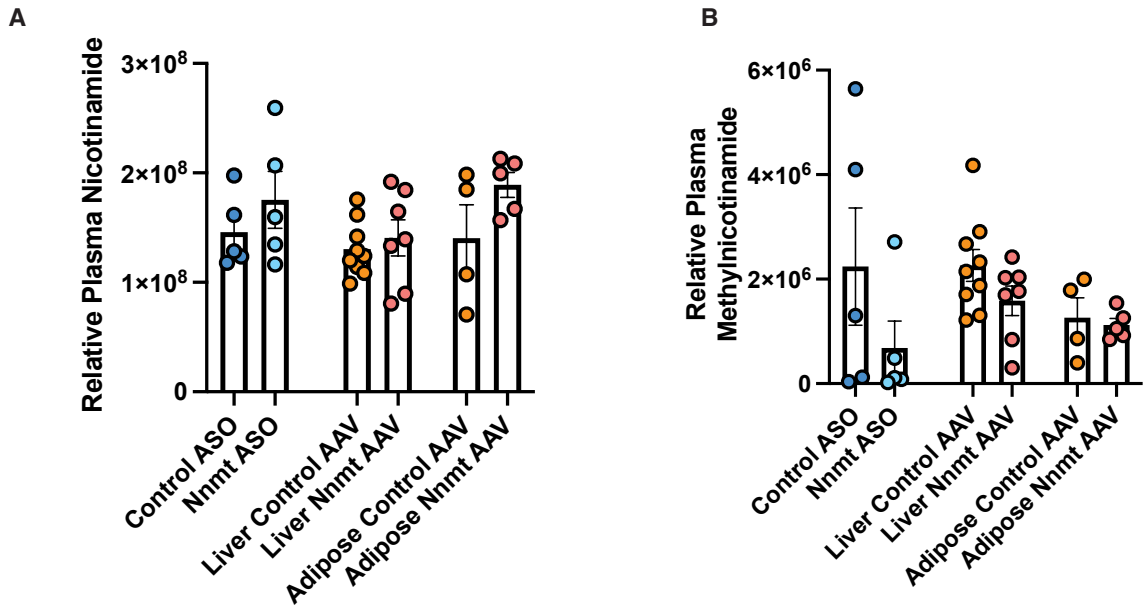

Figure 3.15. Quantification of proliferating and apoptotic cells in the vessel wall. EdU was injected I.P. into ASO-treated females 3 hours before sacrifice. Aortic root sections were stained for DAPI (blue), anti-Cd68 (red), and anti-EdU (green) (A). Quantification of the proportion of proliferating EdU+ macrophages (B). Aortic root sections stained with DAPI, anti-Cd68 (red), and TUNEL (green) (C). Quantification of the proportion of apoptotic, TUNEL + macrophages (D).

A

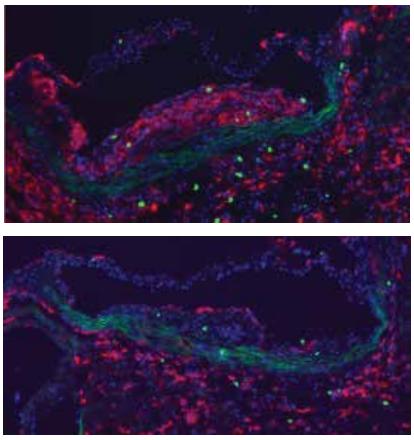

B

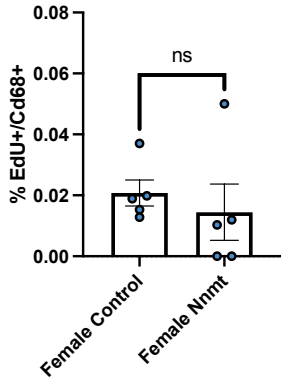
0.08
0.06
0.04
0.02
0.00
% EdU+/Cd68+
ns
Female Control
Female Nnmt

C

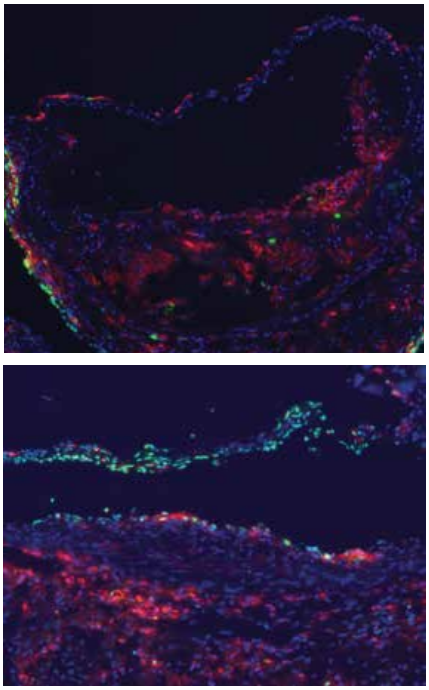

D

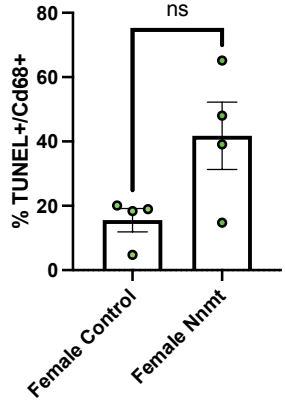
80
60
40
20
0
% TUNEL+/Cd68+
ns
Female Control
Female Nnmt

Figure 3.16. Staining for macrophage proliferation and apoptosis. Proportion of EdU+ macrophages with the *Nnmt* group outlier included (A). The outlier was removed for final analyses following the Grubbs outlier check (alpha = 0.05). Quantitation of Ki67+ Cd68+ cells in lesions, the outlier value from (A) is included (B).

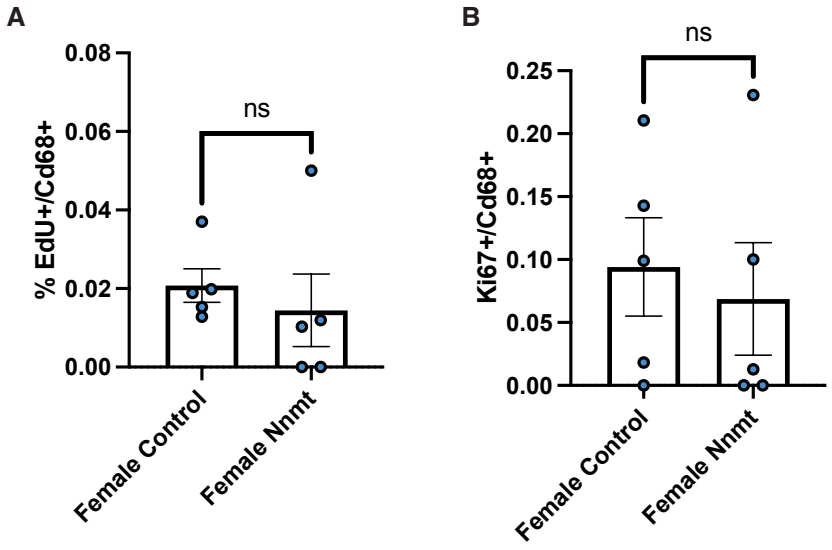

Table 3.1 Cis eQTLs in Chromosome 9 Atherosclerosis Locus

Supplemental Table 1: Cis eQTLs in Chromosome 9 Atherosclerosis Locus							
Symbol	Base Position	CM	Name	cis-eQTL -log_pval	Non-Synonymous SNP	Bi-Correlation with Lesion Area	Correlation pvalue
Cadm1	47,530,173	25.83	cell adhesion molecule 1	5.53		-0.0356	0.73219
Nxpe2	48,318,006	26.38	neurexophilin and PC-esterase domain family, member 2		5		
Nxpe4	48,362,041	26.39	neurexophilin and PC-esterase domain family, member 4		4		
Gm39335	48,452,085		predicted gene 39335				
Rexo2	48,468,514	26.42	RNA exonuclease 2	5.75		-0.0591	0.56918
Rbm7	48,488,709	26.43	RNA binding motif protein 7				
Gm5617	48,495,345	26.43	predicted gene 5617				
Nnmt	**48,591,877**	**26.45**	**nicotinamide N-methyltransferase**	**10.87**		**0.3740**	**0.00019**
Zbtb16	48,654,311	26.47	zinc finger and BTB domain containing 16				
Htr3a	48,899,214	26.53	5-hydroxytryptamine (serotonin) receptor 3A				
Htr3b	48,935,008	26.54	5-hydroxytryptamine (serotonin) receptor 3B				
Usp28	48,985,385	26.56	ubiquitin specific peptidase 28				
Zw10	49,055,581	26.58	zw10 kinetochore protein				
Tmprss5	49,081,260	26.59	transmembrane protease, serine 5 (spinesin)				
Gm4894	49,268,572	26.6	predicted gene 4894				
Drd2	49,340,662	26.72	dopamine receptor D2				
Ankk1	49,415,222	26.83	ankyrin repeat and kinase domain containing 1		2		
Ttc12	49,436,963	26.83	tetratricopeptide repeat domain 12		1		
Ncam1	49,502,136	26.83	neural cell adhesion molecule 1				
Plet1	50,494,525	27.71	placenta expressed transcript 1				
Pts	50,521,618	27.73	6-pyruvoyl-tetrahydropterin synthase				
Bco2	50,533,087	27.74	beta-carotene oxygenase 2	12.91		0.2998	0.00317
Tex12	50,557,148	27.75	testis expressed gene 12				
Il18	50,575,273	27.75	interleukin 18				
Sdhd	50,596,340	27.75	succinate dehydrogenase complex, subunit D				
Timm8b	50,603,901	27.75	translocase of inner mitochondrial membrane 8B				
AU019823	50,605,240	27.75	expressed sequence AU019823				
Pih1d2	50,617,321	27.75	PIH1 domain containing 2				
Dlat	50,634,633	27.75	dihydrolipoamide S-acetyltransferase		1		
Dixdc1	50,662,752	27.75	DIX domain containing 1				
2310030G06Rik	50,739,691	27.75	RIKEN cDNA 2310030G06 gene	6.02		-0.3363	0.00086
Hspb2	50,751,072	27.75	heat shock protein 2		1		
Cryab	50,752,758	27.75	crystallin, alpha B		1		
Fdxacb1	50,768,236	27.75	ferredoxin-fold anticodon binding domain 1		2	-0.0167	0.87230
1110032A03Rik	50,762,828	27.75	RIKEN cDNA 1110032A03 gene	8.89	1		
Alg9	50,775,019	27.75	asparagine-linked glycosylation 9	12.33		-0.0104	0.92040
Ppp2r1b	50,845,301	27.75	protein phosphatase 2, regulatory subunit A, beta				
Sik2	50,892,801	27.75	salt inducible kinase 2				
Layn	51,056,780	27.79	layilin				
4833427G06Rik	51,081,313	27.81	RIKEN cDNA 4833427G06 gene				
Btg4	51,116,001	27.84	B cell translocation gene 4				
Gm32742	51,130,307	27.84	predicted gene 32742		1		
Pou2af1	51,213,690	27.95	POU domain, class 2, associating factor 1				
Gm684	51,270,258	28.02	predicted gene 684				
1810046K07Rik	51,318,385	28.05	RIKEN cDNA 1810046K07Rik gene		1		
Arhgap20	51,765,337	28.62	Rho GTPase activating protein 20				
Fdx1	51,943,307	28.62	ferredoxin 1				
Rdx	52,047,150	28.62	radixin				

References

1. Brænne, I. *et al.* Prediction of Causal Candidate Genes in Coronary Artery Disease Loci. *Arterioscler. Thromb. Vasc. Biol.* **35**, 2207–2217 (2015).
2. CARDIoGRAMplusC4D Consortium *et al.* Large-scale association analysis identifies new risk loci for coronary artery disease. *Nat. Genet.* **45**, 25–33 (2013).
3. Bennett, B. J. *et al.* A high-resolution association mapping panel for the dissection of complex traits in mice. *Genome Res.* **20**, 281–290 (2010).
4. Yalcin, B. & Flint, J. Association studies in outbred mice in a new era of full-genome sequencing. *Mamm. Genome* **23**, 719–726 (2012).
5. Lusis, A. J. *et al.* The Hybrid Mouse Diversity Panel: a resource for systems genetics analyses of metabolic and cardiovascular traits. *J. Lipid Res.* **57**, 925–942 (2016).
6. Bennett, B. J. *et al.* Genetic Architecture of Atherosclerosis in Mice: A Systems Genetics Analysis of Common Inbred Strains. *PLoS Genet.* **11**, e1005711 (2015).
7. Erbilgin, A. *et al.* Transcription Factor Zhx2 Deficiency Reduces Atherosclerosis and Promotes Macrophage Apoptosis in Mice. *Arterioscler. Thromb. Vasc. Biol.* **38**, 2016–2027 (2018).
8. Hong, S. *et al.* Nicotinamide N-methyltransferase regulates hepatic nutrient metabolism through Sirt1 protein stabilization. *Nat. Med.* **21**, 887–894 (2015).
9. Kraus, D. *et al.* Nicotinamide N-methyltransferase knockdown protects against diet-induced obesity. *Nature* **508**, 258–262 (2014).
10. Liu, M. *et al.* Serum N1-Methylnicotinamide is Associated With Coronary Artery Disease in Chinese Patients. *J. Am. Heart Assoc.* **6**, e004328.

11. Chlopicki, S. *et al.* 1-Methylnicotinamide (MNA), a primary metabolite of nicotinamide, exerts anti-thrombotic activity mediated by a cyclooxygenase-2/prostacyclin pathway. *British Journal of Pharmacology* vol. 152 230–239 (2007).
12. Mayer, E. L., Jacobsen, D. W. & Robinson, K. Homocysteine and coronary atherosclerosis. *J. Am. Coll. Cardiol.* **27**, 517–527 (1996).
13. Cui, Y. *et al.* Downregulation of nicotinamide N-methyltransferase inhibits migration and epithelial-mesenchymal transition of esophageal squamous cell carcinoma via Wnt/β-catenin pathway. *Mol. Cell. Biochem.* **460**, 93–103 (2019).
14. Wang, S. S. *et al.* Mapping, genetic isolation, and characterization of genetic loci that determine resistance to atherosclerosis in C3H mice. *Arterioscler. Thromb. Vasc. Biol.* **27**, 2671–2676 (2007).
15. Choi, Y. & Chan, A. P. PROVEAN web server: a tool to predict the functional effect of amino acid substitutions and indels. *Bioinformatics* **31**, 2745–2747 (2015).
16. Lonsdale, J. *et al.* The Genotype-Tissue Expression (GTEx) project. *Nat. Genet.* **45**, 580–585 (2013).
17. Tabula Muris Consortium *et al.* Single-cell transcriptomics of 20 mouse organs creates a Tabula Muris. *Nature* **562**, 367–372 (2018).
18. Barbul, A. Arginine: biochemistry, physiology, and therapeutic implications. *JPEN J. Parenter. Enteral Nutr.* **10**, 227–238 (1986).
19. Kamat, J. P. & Devasagayam, T. P. Nicotinamide (vitamin B3) as an effective antioxidant against oxidative damage in rat brain mitochondria. *Redox Rep.* **4**, 179–184 (1999).

20. Guan, X., Lin, P., Knoll, E. & Chakrabarti, R. Mechanism of inhibition of the human sirtuin enzyme SIRT3 by nicotinamide: computational and experimental studies. *PLoS One* **9**, e107729 (2014).
21. García-Rodríguez, J. L. *et al.* SIRT1 controls liver regeneration by regulating bile acid metabolism through farnesoid X receptor and mammalian target of rapamycin signaling. *Hepatology* **59**, 1972–1983 (2014).
22. Mehrabian, M. *et al.* Influence of the apoA-II gene locus on HDL levels and fatty streak development in mice. *Arterioscler. Thromb.* **13**, 1–10 (1993).
23. McDonald, A. I. *et al.* Endothelial Regeneration of Large Vessels Is a Biphasic Process Driven by Local Cells with Distinct Proliferative Capacities. *Cell Stem Cell* **23**, 210-225.e6 (2018).
24. Kemper, J. K. Regulation of FXR transcriptional activity in health and disease: Emerging roles of FXR cofactors and post-translational modifications. *Biochim. Biophys. Acta* **1812**, 842–850 (2011).
25. Love, M. I., Huber, W. & Anders, S. Moderated estimation of fold change and dispersion for RNA-seq data with DESeq2. *Genome Biol.* **15**, 550 (2014).
26. Liao, Y., Wang, J., Jaehnig, E. J., Shi, Z. & Zhang, B. WebGestalt 2019: gene set analysis toolkit with revamped UIs and APIs. *Nucleic Acids Res.* **47**, W199–W205 (2019).
27. Rifkind, A. B., Lee, C., Chang, T. K. H. & Waxman, D. J. Arachidonic acid metabolism by human cytochrome P450s 2C8, 2C9, 2E1, and 1A2: Regioselective oxygenation and evidence for a role for CYP2C enzymes in arachidonic acid epoxygenation in human liver microsomes. *Arch. Biochem. Biophys.* **320**, 380–389 (1995).

28. Shoieb, S. M., El-Ghiaty, M. A., Alqahtani, M. A. & El-Kadi, A. O. S. Cytochrome P450-derived eicosanoids and inflammation in liver diseases. *Prostaglandins Other Lipid Mediat.* **147**, 106400 (2020).

29. Maciejewska, D. *et al.* Metabolites of arachidonic acid and linoleic acid in early stages of non-alcoholic fatty liver disease--A pilot study. *Prostaglandins Other Lipid Mediat.* **121**, 184–189 (2015).

30. Domagala, T. B. *et al.* Nitric oxide production and endothelium-dependent vasorelaxation ameliorated by N1-methylnicotinamide in human blood vessels. *Hypertension* **59**, 825–832 (2012).

31. Mateuszuk, L. *et al.* Anti-atherosclerotic effects of 1-methylnicotinamide (MNA) in ApoE/LDLR-/-mice: a comparison with nicotinic acid. *J. Pharmacol. Exp. Ther.* **356**, 24 (2016).

32. Mateuszuk, L. *et al.* Antiatherosclerotic Effects of 1-Methylnicotinamide in Apolipoprotein E/Low-Density Lipoprotein Receptor–Deficient Mice: A Comparison with Nicotinic Acid. *J. Pharmacol. Exp. Ther.* **356**, 514–524 (2016).

33. Williams, P. A. *et al.* Vitamin B3 modulates mitochondrial vulnerability and prevents glaucoma in aged mice. *Science* **355**, 756–760 (2017).

34. Sinha, S. K. *et al.* Local M-CSF (macrophage colony-stimulating factor) expression regulates macrophage proliferation and apoptosis in atherosclerosis. *Arterioscler. Thromb. Vasc. Biol.* **41**, 220–233 (2021).

35. Erdmann, J., Kessler, T., Munoz Venegas, L. & Schunkert, H. A decade of genome-wide association studies for coronary artery disease: the challenges ahead. *Cardiovasc. Res.* **114**, 1241–1257 (2018).

36. von Scheidt, M. *et al.* Applications and Limitations of Mouse Models for Understanding Human Atherosclerosis. *Cell Metab.* **25**, 248–261 (2017).

37. Jiang, N. *et al.* N-methylnicotinamide protects against endothelial dysfunction and attenuates atherogenesis in apolipoprotein E-deficient mice. *Mol. Nutr. Food Res.* **60**, 1625–1636 (2016).

38. Biedroń, R. *et al.* 1-Methylnicotinamide and nicotinamide: two related anti-inflammatory agents that differentially affect the functions of activated macrophages. *Arch. Immunol. Ther. Exp.* **56**, 127–134 (2008).

39. Hedrick, C. C., Castellani, L. W., Warden, C. H., Puppione, D. L. & Lusis, A. J. Influence of mouse apolipoprotein A-II on plasma lipoproteins in transgenic mice. *J. Biol. Chem.* **268**, 20676–20682 (1993).

40. Puppione, D. L. & Charugundla, S. A microprecipitation technique suitable for measuring alpha-lipoprotein cholesterol. *Lipids* **29**, 595–597 (1994)

41. Millar, J. S., Cromley, D. A., McCoy, M. G., Rader, D. J. & Billheimer, J. T. Determining hepatic triglyceride production in mice: comparison of poloxamer 407 with Triton WR-1339. *J. Lipid Res.* **46**, 2023–2028 (2005)

Chapter 4: Characterization of non-alcoholic fatty liver disease (NAFLD) development in resistant and susceptible mouse models by RNA-sequencing

Introduction

Non-alcoholic fatty liver disease (NAFLD) is the most prevalent liver disorder in the population [1]. It is estimated that 20-30% of the population in Western countries are affected by NAFLD [2]. Despite the high prevalence of this disease, the natural history and etiology are poorly understood. Human studies have shown that NAFLD is strongly associated with obesity, diabetes, and dyslipidemia. NAFLD is initiated by the accumulation of excess lipid in hepatocytes, which can lead to more severe phenotypes like inflammation, called non-alcoholic steatohepatitis (NASH) and fibrosis. NAFLD phenotypes are influenced by local and systemic inflammation, elevated plasma lipids and cholesterol levels, and require coordinated extracellular remodeling of tissues by vascular cells during fibrosis. These risk factors have been studied and identified as causal in mouse models of disease and in clinical human cohorts [3].

The liver is a heterogeneous tissue where 60% of the cells are comprised of hepatocytes [15]. Hepatocytes perform the major metabolic functions of the liver and the non-parenchymal cells (NPCs) like endothelial cells, macrophages, and stellate cells support liver homeostasis by influencing blood flow and inflammation. Macrovesicular steatosis, the state of increased fat accumulation, is the predominating phenotype of NAFLD in the population and is often associated with phenotypes like diet-induced obesity and Type 2 Diabetes [16]. Steatosis is the first stage of NAFLD and can be reversed by restoring caloric flux and increasing insulin sensitivity [17]. However, progression to more severe phenotypes like inflammation and liver fibrosis, clinically characterized as nonalcoholic steatohepatitis (NASH), are more difficult to reverse by comparison [18]. Steatosis occurs predominantly in hepatocytes, which are the major functional

cell type in the liver, but progression to NASH relies on molecular changes in the non-parenchymal (NPC) cell types like endothelial cells, hepatic stellate cells macrophages, and the infiltration of circulating immune cells. Excess lipid can lead to cellular toxicity, which induces the expression of chemokines, triggering an immune response and subsequent infiltration of circulating cells. NPCs participate in NAFLD progression in several ways: Endothelial cells recruit leukocytes in the blood bypresenting adhesion molecules to on their surfaces, resident macrophages become polarized to a pro-inflammatory state, and stellate cells become activated to express pro-fibrotic chemokines, demonstrating necessary functions for NPCs in NAFLD progression.

Prevention and treatment options for NAFLD are limited [4]. Studies in human populations and animal studies indicate that genetics plays an important role in determining the susceptibility to the development of NAFLD [5,6]. The heritability of steatosis is estimated to be ~39% after adjusting for age, sex, race, and BMI [7]. Studies in twins suggest that the heritability of fibrosis phenotypes is nearly 50% [8]. Genome-wide association studies and candidate gene approaches in mouse and human models of NAFLD have identified genes involved in NAFLD risk. The best known are *PNPLA3, TM6SF2,* and *APOB* [9–12]. These genes have been primarily implicated in fatty acid metabolism, further supporting the early role of hepatocytes in the progression to fibrosis and inflammation. Up to 70 genome-wide significant loci have been identified in human studies of NAFLD, but the cell types expressing some of these genes have not been validated [13]. Differential expression and expression QTL analyses have been previously used to identify genes associated with NAFLD, but gene expression in these studies is often measured in bulk tissue which does not provide cell type resolution of relevant cell types [14].

The Lusis lab has previously completed a genetic study using the Hybrid Mouse Diversity Panel (HMDP), a panel of 100+ diverse mouse strains, to identify genetic variation associated with atherosclerosis susceptibility and related clinical risk factors [19]. The mouse model for atherosclerosis also encompassed pathophysiological changes observed in human NAFLD progression. Liver inflammation and fibrosis were induced by breeding strains onto a transgenic hyperlipidemic background accompanied by 16 weeks of a high fat, high cholesterol Western style diet. It was observed that this experimental design also induced liver inflammation and fibrosis in some strains. Novel candidate genes for atherosclerosis and liver fibrosis traits were identified using genetic mapping approaches [14].

Recent advances in single cell RNA-sequencing methods allow for the quantification of mRNA transcripts of thousands of individual cells, which allow for the identification of subpopulations of cells along with their unique gene expression profiles [20–23]. The generation of these data will provide an atlas to validate the relevant cell types of previously identified candidate genes. The generation of cell type profiles in liver under pathological conditions can also be leveraged to estimate the proportions of each representative cell type in bulk tissue. Here, we use single cell and bulk RNA-sequencing to identify cell type and genetic changes during NAFLD progression in a subset of genetically susceptible and resistant mouse strains. In this chapter, we selected a three inbred mouse strains exhibiting low to high liver fibrosis phenotypes for longitudinal studies. We plan to expand on the analyses presented here with still forthcoming data including liver histology, lipid, and metabolite analysis for each strain. We will then integrate these various data to validate and follow up any changes observed by gene expression analysis.

Methods

NPC isolation and whole cell sequencing. We were interested in identifying the cell types present in the different strains during the development of fibrosis. Specifically, we were interested in the identification of non-hepatocyte cells, collectively called non-parenchymal cells (NPC). Initially, we began with livers from C57BL/6J and 129/SvJ animals on diet for 12 weeks, as well as livers from B6 mice on diet for 8 weeks. To enrich for the NPC fraction, shortly after sacrifice, we perfused the livers with PBS through the left ventricle. We then dissected the livers and used the Miltenyi MACS mouse Liver Dissociation Kit to isolate the NPCs (Order# 130-105-807). Once the NPC pellet was isolated, we counted and stained for viability using 7-AAD (1:20). We then sorted 7-AAD negative cells using a BD FACSAria cell sorter set with a 70µm nozzle. We targeted 10,000 live cells for sequencing using the 10X Genomics Chromium Single Cell 3' Solution System.

Analysis of single-cell data.

Bulk RNA sequencing of whole frozen liver. We isolated RNA from whole liver using 20-30mg of tissue homogenized using a BeadRuptor bead mill homogenizer in 1mL of Qiazol extraction buffer. We then centrifuged the homogenate for 30 seconds at 10,000 rpm to clear the supernatant. We then used the supernatant with the Direct-zol RNA miniprep kit (Zymo Research cat# R2072 with on-column DNase extraction to complete RNA isolation.

Nuclei isolation from whole frozen liver. We also isolated nuclei for 10X 3' RNA library preparation. We used frozen liver samples from the three strains collected at 0, 8, and 12 weeks.

To isolate nuclei, we diced 20-30 milligrams of frozen tissue on a glass slide until thoroughly broken up. We then used this tissue with the Invent Biosciences Minute Detergent-Free nuclei isolation kit. We counted the final nuclei using Trypan blue and a hemocytometer. We pooled three strains together from the same time point into one library targeting a total of 10,000 nuclei. After pooling, we counted the cellular concentration of the pool before GEM generation.

Strain identity was determined post sequencing using the DMUXLET method based on known genotype information. Reads were demultiplexed and aligned to mouse genome mm10 using STAR. Digital transcript count matrices were generated using 10X Cell Ranger application. Datasets were integrated and normalized using scTransform in R with the Seurat library package. Distinct cell populations were identified by annotating the uniquely most differentially expressed genes as well as localization of known cell type markers.

RNA-sequencing and Analysis. We sequenced the whole liver samples in two batches. The C57BL/6J samples were submitted for sequencing in June of 2020 and the other strains were sequenced in August 2021. All the samples were sequenced on an Illumina NovaSeq for 100 cycles (2x50bp). We quantified and aligned the transcripts using the R package Kallisto. We also calculated Transcripts Per Million (TPM). To identify differential genes during progression we normalized the replicate TPM values to the 0 time point in the C57BL/6J strain.

HMDP correlations. We previously performed bicorrelation analysis between liver gene expression values as measured by microarray and the measurements of liver fibrosis area using the bicorr function in the R package WGCNA.

Results

Single cell sequencing of NPCs profiles for resident and infiltrating immune cells

The 100+ strains comprising the Atherosclerosis HMDP capture over 500-fold variation in liver fibrosis area. The liver fibrosis phenotypes were measured after 16 weeks of a high fat, high cholesterol diet. To pursue mechanistic studies related to progression prior to the 16-week time point, we selected a subset of three strains spanning resistant to moderately susceptible, and susceptible phenotypes (Figure 4.1). Within this subset of strains, the resistant strain, 129/SvJ, had an average of 0.41% fibrosis area, whereas the C57BL/6J and had BxD19/TyJ had average areas of 1.73% and 3.43%, respectively. We sacrificed a cohort of animals from the representative strains at 8 weeks of age, which served as a baseline, 2 weeks on the high fat, high cholesterol diet as well as 4, 8, 12, and 16 weeks on the diet.

We previously showed that cell major changes in the liver become detectable by qPCR analysis beginning around 8 weeks in C57BL/6J mice [14]. Genes involved in inflammatory cell infiltration (*F4/80* and *Ccl2*) and stellate cell activation and fibrogenesis (*Col1a1*) progressively increased. To identify all the NPCs present in the liver at this time point, we isolated NPCs from C57BL/6J and 129/SvJ mice after 12 weeks of diet for single cell RNA-sequencing. Previous profiling of the C57BL/6J time course identified critical changes in the expression of inflammatory genes at 8 weeks, so we additionally profiled NPCs from this time point for our analyses. Following UMAP clustering of individual cells, we were able to identify clusters of vascular cells, resident immune cells, and infiltrating/circulating immune cells in addition to a small cluster of hepatocytes (Figure 4.2).

Within the immune cells, we identified subsets of liver macrophages initially described by Seidman et al. including resident Kupffer cells, monocyte-derived macrophages, and

restorative macrophages [24]. Monocyte-derived macrophages are typically proinflammatory whereas restorative macrophages are involved in the resolution of inflammation and tissue repair. We also identified subsets of other immune cells including T, NK, B, and classical and plasmacytoid dendritic cells, and neutrophils.

Once the cell types were classified, we queried the dataset to find cell types in the liver expressing candidate genes from human GWAS studies. Vujkovic et al. identified 77 GWAS loci from a cohort of 90,000 NAFLD patients [13]. Twenty two of these 77 GWAS genes were present in the NPC single-cell dataset (Figure 4.3). We observed most genes, twelve out of twenty-two, to be expressed in hepatocytes. This fits what is currently known about the functional cell types for the strongest risk genes, such as *PNPLA3,* in human genetic NAFLD studies. A set of GWAS genes including *Mertk, Crim1, Tm4sf1,* and *Flt1* were identified to be expressed in endothelial and stellate cells, key cell types involved in the progression of fibrosis [25].

Sequencing the disease progression of 3 strains

To further investigate the gene expression changes associated with NAFLD progression as well as the mechanisms underlying genetic susceptibility, we performed bulk RNA-sequencing on whole liver RNA isolated at 0, 2, 4, 8, 12, and 16 weeks from the three representative strains. Across all three datasets we identified 11,665 unique transcripts for comparative analysis. We performed principal component analysis (PCA) of the genes with an average TPM > 5 (Figure 4.4). By comparing the expression across all transcripts, PCA clusters samples together according to gene expression relatedness. PC1 explained 41.5% of the variance and appeared to be driven by progression through the time course. The baseline and earlier timepoint samples clustered together on the righthand side and moved increasingly leftward

through the later time points. It is notable that at 12 and 16 weeks, the susceptible strains C57BL/6J and BxD19/TyJ were at the very end of PC1, where the 129/SvJ strain remained toward the middle (Figure 4.4). This suggests that at these timepoints, the progression of the 129/SvJ strain is behind that of BxD19/TyJ and C57BL/6J. This suggests that there is a shared developmental trajectory between strains and mechanisms of resistance delay progression along the trajectory. PC2 explained 22.1% of the variance in expression and is reflective of strain or batch differences. The 129/SvJ and BxD19/TyJ samples technically differ from the C57BL/6J samples due to a 2 year gap between RNA isolation, library preparation, and sequencing. These libraries were also sequenced to a greater depth. Future explorations with these data may warrant the application of approaches such as COMBAT regression to determine if mitigation of technical variation would reduce the variance explained by PC2.

Identifying progression-associated changes in gene expression

We removed lowly expressed genes and then normalized the expression within groups to the average value of the C57BL/6J baseline group. We identified a subset of 72 genes with 10-to-150-fold increases expression in one time point compared to baseline (Figure 4.5). As anticipated, the greatest changes in gene expression compared to baseline occurred in the susceptible strains, C57BL/6J and BxD19/TyJ during the later stages of progression, 12 and 16 weeks. These were the groups that were furthest away from the 0-week baseline by PCA. Using WebGestalt, we performed over-representation analysis with the 72 genes, annotating the genes to gene ontology (GO) and mammalian phenotype ontology categories. We identified significant enrichment (FDR < 5E-6) for gene sets associated with extracellular regions and phenotypes involved in altered susceptibility to bacterial infections. The genes with the highest fold change

in expression, greater than 100x the level at baseline, were *Ly6d* and *Lcn2*. *Ly6d* is a gene expressed in lymphocyte development, and the observed increase suggested a greater prevalence of these cell types or massive upregulation of expression during later stages of progression. *Lcn2* is a lipocalin gene involved in the recruitment of neutrophils. These enrichments on an individual gene and categorical basis presumably reflect the inflammatory and fibrotic mechanisms involved in NAFLD progression in susceptible strains.

We identified a smaller subset of genes that were upregulated only in 129/SvJ mice which may be involved in resistance to fibrosis. Such genes include members of the major urinary protein (*Mup)* family; *Mup1, Mup9,* and *Mup5*. The *Mup* genes are highly polymorphic between inbred mouse strains and belong to a category of lipocalin proteins. The *Mup* family are secreted transport proteins involved in pheromone communication and metabolism. Liver *Mup1* expression decreases under obese and diabetic conditions and expression of recombinant MUP1 protein attenuated glucose intolerance and insulin resistance in mice [26]. Expression of recombinant MUP1 protein also reduced the expression of lipogenesis genes in the liver [27]. These data validate that the genetic variation in 129/SvJ compared to C57BL/6J and BxD19/TyJ strains is responsible for higher basal expression *Mup* genes in the liver. We also identified a gene *Abhd1*, alpha beta hydrolase domain 1, which is upregulated in 129/SvJ but lowly expressed in the other two strains. Knockdown experiments of *Abhd1* in rodent and human models have identified a role in protection from oxidative stress [28]. Taken together, these changes in the 129/SvJ strain suggest that the genetic mechanisms involved in NAFLD protection may be related to metabolic adaptation to the Western diet; potentially through improved glucose parameters, decreased lipogenesis, and decreased oxidative stress.

Identifying cell types associated with progression-associated expressed genes

We queried the expression of the 72 highly differentially expressed genes in our dataset of gene expression profiles generated from NPCs to identify relevant cell types involved (Figure 4.6). Forty-four of the 72 genes were present in the NPC single-cell dataset. As suggested by the literature, the gene with the greatest fold change, *Ly6d,* was primarily expressed in the lymphocytes, with the highest expression in B cell and T cell clusters [29]. *Ly6d* was also expressed in plasmacytoid dendritic cells, a cell type that produces large amounts of type I interferons and pro-inflammatory cytokines [30].

The other highly upregulated gene in susceptible strains, *Lcn2*, was found to be expressed in neutrophils (the cell type where the gene was initially identified in the literature) as well as in epithelial and smooth muscle cells. *Lcn2* has been suggested to mediate the epithelial-mesenchymal transition (EMT) in epithelial cells during hepatocellular carcinoma [31]. Clinical studies in humans showed that gene expression and protein levels of *Lcn2* were significantly positively correlated with NASH [32]. When HEPG2 cells were treated with cytokines, the levels of *Lcn2* expression increased [32]. For this reason, *Lcn2* has been suggested as biomarker for NAFLD progression, and our results support this.

Twenty of the 44 genes were primarily expressed in macrophage cell types. The three subtypes (Kupffer, monocyte derived, and restorative) had similar gene expression profiles, while Kupffer cells had uniquely high expression of two genes, *Lpl* and *Cd5l*. *Cd5l* has been reported to promote the survival and phagocytic activity of macrophages during liver inflammation [33]. *Lpl*, lipoprotein lipase, is a gene expressed by macrophages in the liver involved in the hydrolysis of triglycerides. *Lpl* expression has been shown to be upregulated in response to TNFα, and overexpression of hepatic *Lpl* causes steatosis and insulin resistance [34,35].

Correlations of differentially expressed genes in the HMDP

Sixty eight out of the 77 differentially expressed genes were present in the liver expression data generated from the liver fibrosis HMDP study. Previously, we performed correlation analyses between transcript abundance and clinical traits such as liver and plasma lipids and liver fibrosis [14]. Sixty-three genes exhibited significant correlations (bicor p-value < 0.05) with liver fibrosis area in a panel of 100+ strains (Figure 4.7). Most of the significantly correlated genes, 54 out of 63, were positively correlated with fibrosis. Given that most of the initial differentially expressed genes were primarily identified in just 3 strains to be highly expressed under pro-fibrotic conditions, these significant correlations in 100 strains validate the observation that these genes are involved in fibrosis progression and severity.

Single-nuclei sequencing from whole liver identifies hepatocyte and NPC types

As an additional approach to survey cellular heterogeneity associated with NAFLD progression, we performed single-nuclei RNA-sequencing from frozen liver tissue isolated at 0, 8, and 12 weeks of progression. Unlike the single-cell dataset where the population of cells was first depleted of hepatocytes, the relative proportion of hepatocytes to non-hepatocytes more accurately reflected the true composition in the liver. We identified the cell type clusters using previously defined hepatocyte and NPC expression profiles [23]. We identified primarily hepatocytes, but also captured NPCs like epithelial, macrophage, and vascular cells (Figure 4.8). Within the hepatocyte cluster, we were able to observe zonation between periportal and pericentral hepatocytes.

Discussions

To better understand the molecular changes involved in the progression of NAFLD phenotypes, from steatosis to NASH and from NASH to fibrosis, we conducted a longitudinal study profiling gene expression change in genetically resistant and susceptible mouse strains. We generated gene expression profiles from whole liver at 6 different time points of progression. We leveraged the effect of genetic variation between inbred mouse strains and compared the gene expression trajectories between a fibrosis resistant, moderately susceptible, and highly susceptible strains over the course of 16 weeks. We preformed bulk sequencing on whole liver tissue as well as single-cell and single-nuclei sequencing at an important inflection point in progression, between 8 and 12 weeks and were able to capture a diverse population of resident and immune cells. The benefit of this approach was the robustness of bulk RNA sequencing to observe system-wide changes coupled with the resolution of individual cell type expression profiles. An example of applying such a resource was the identification of cell types that expressed candidate genes from GWAS studies in humans[13]. In the future, we plan to use these data to follow up on our own candidate genes from previous key driver and Mergeomics analysis [36–38].

Through our analyses we showed that genetically diverse mouse strains shared a similar trajectory of NAFLD development that explains 40% of the variance in gene expression. However, each strain moves along this trajectory at different rates. For example, PCA showed that the susceptible strain, BxD19/TyJ, had substantial gene expression changes along this axis between 0 and 2 weeks and between 12 and 16 weeks. Comparatively, the gene expression profile of the resistant strain progressed slower than BxD19/TyJ, with the 8 week sample resembling the state of the susceptible strain after only 2 weeks. After 16 weeks, the resistant

strain had only progressed far enough along to resemble a susceptible mouse between 8 and 12 weeks.

Gene expression differences in the resistant strain, 129/SvJ reflect potential mechanisms involved in delaying the progression to more inflammatory and fibrotic phenotypes. The 129/SvJ strain was observed to have 10-fold higher expression of the gene *Abhd1* than the susceptible strains. *Abhd1* was identified in an additional HMDP as well as in a Diversity Outbred study to be associated with circulating levels of lysophosphatidylcholines (lysoPCs) [39,40]. Overexpression of *Abhd1* in the hepatocytes leads to an increase in lysoPCs and PCs [40]. In human studies lysoPCs are negatively associated with steatosis [41]. The mechanism proposed for this association is a lysoPC enrichment for HDL cholesterol particles, which are known to be negatively associated with liver fat content. Mechanisms involved in NAFLD susceptibility include activation of resident macrophages and Kupffer cells, to increase expression of *Lpl* and *Cd5l*, which leads to increased liver triglyceride accumulation and inflammation.

This project, as it is presented here, is still incomplete. Future directions include leveraging the single nuclei cell type profiles to deconvolute the time course bulk gene expression data as well as the liver microarray HMDP dataset to quantify the proportion of cell types present. Previous attempts to use the NPC single cell gene expression profiles to deconvolute whole liver data yielded poor results due to the high proportion of hepatocytes in whole liver, and relatively low resolution in the single cell data. Additionally, with the bulk RNA sequencing data we can subset the differentially expressed genes into their respective cell types and perform correlations between cell types to identify any crosstalk between resident and inflammatory cells across different time points. We also plan to validate the cell type differences observed here through bulk or single-cell analysis by histology. This study will provide an

integrated data resource to understand genetic, cellular, and molecular perturbations underlying NAFLD progression and inform the discovery of biomarkers and disease therapy targets.

Figures

Figure 4.1 Distribution of liver fibrosis area in the atherosclerosis HMDP.

Between 101 strains in the atherosclerosis HMDP we observed a 500-fold change (0.01% to 5.8%) in liver fibrosis area. For further analysis, we selected 3 strains which were resistant (green), moderately susceptible (yellow), and highly susceptible (red) to liver fibrosis in our model.

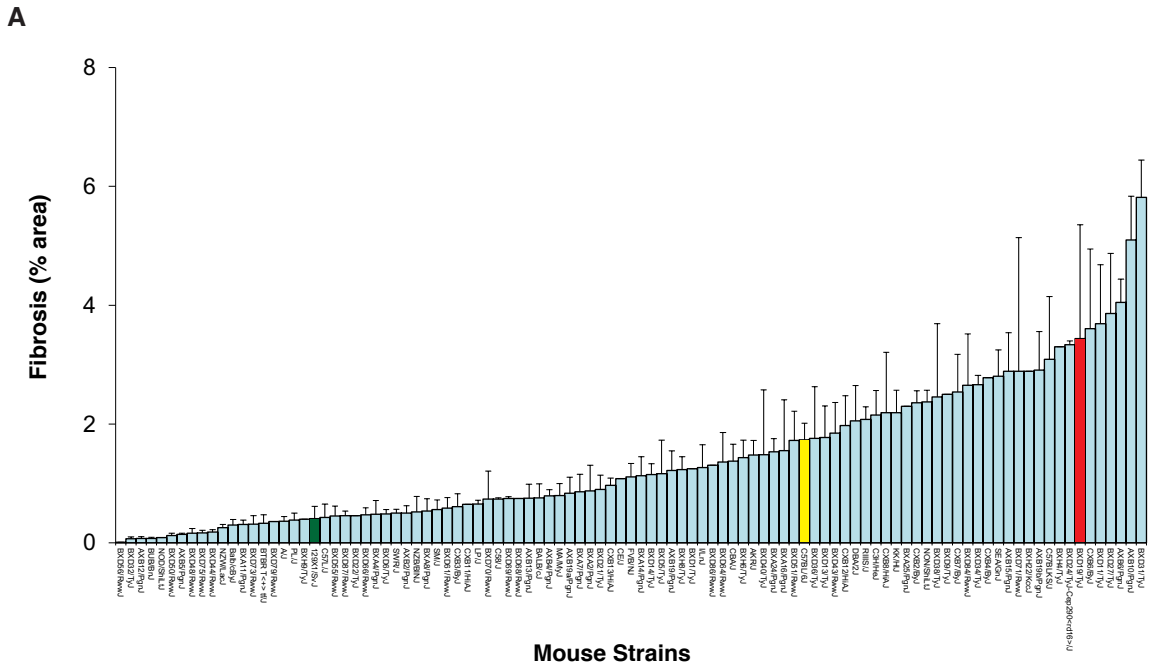

Figure 4.2 Non-parenchymal cell types in C57BL/6J and 129/SvJ.

UMAP clustering visualization of representative NPC cell types at 8 and 12 week from C57BL/6J and 129/SvJ livers. N = 2 animals per strain/time point. Each dot represents a single cell, color coded by cell type. DC; dendritic cells, NK; natural killer cells.

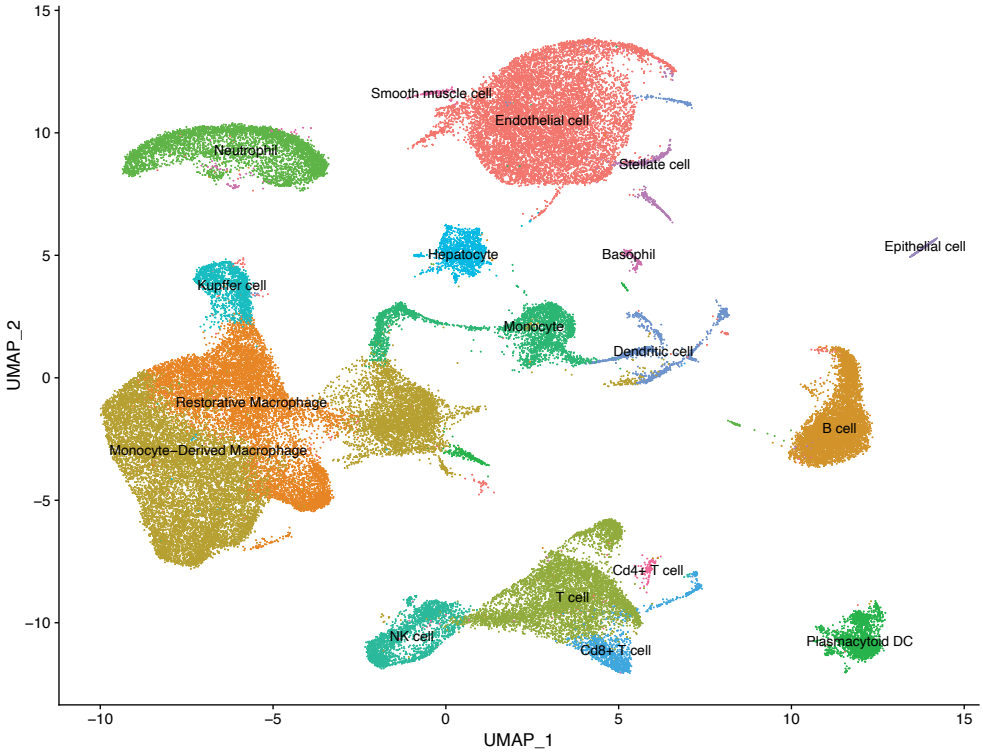

Figure 4.3 Human GWAS candidate gene expression in NPC populations.

Twenty-two out of 77 loci identified as genome-wide significant in human NAFLD GWAS cohorts were observed in our NPC single cell dataset. Each cell type cluster was down sampled to 100 cells and queried for the expression level for each of the twenty two loci. Each column represents 100 representative cells from an identified cell type. Yellow lines indicate higher relative expression of the gene within a representative cell and black indicates no or low expression.

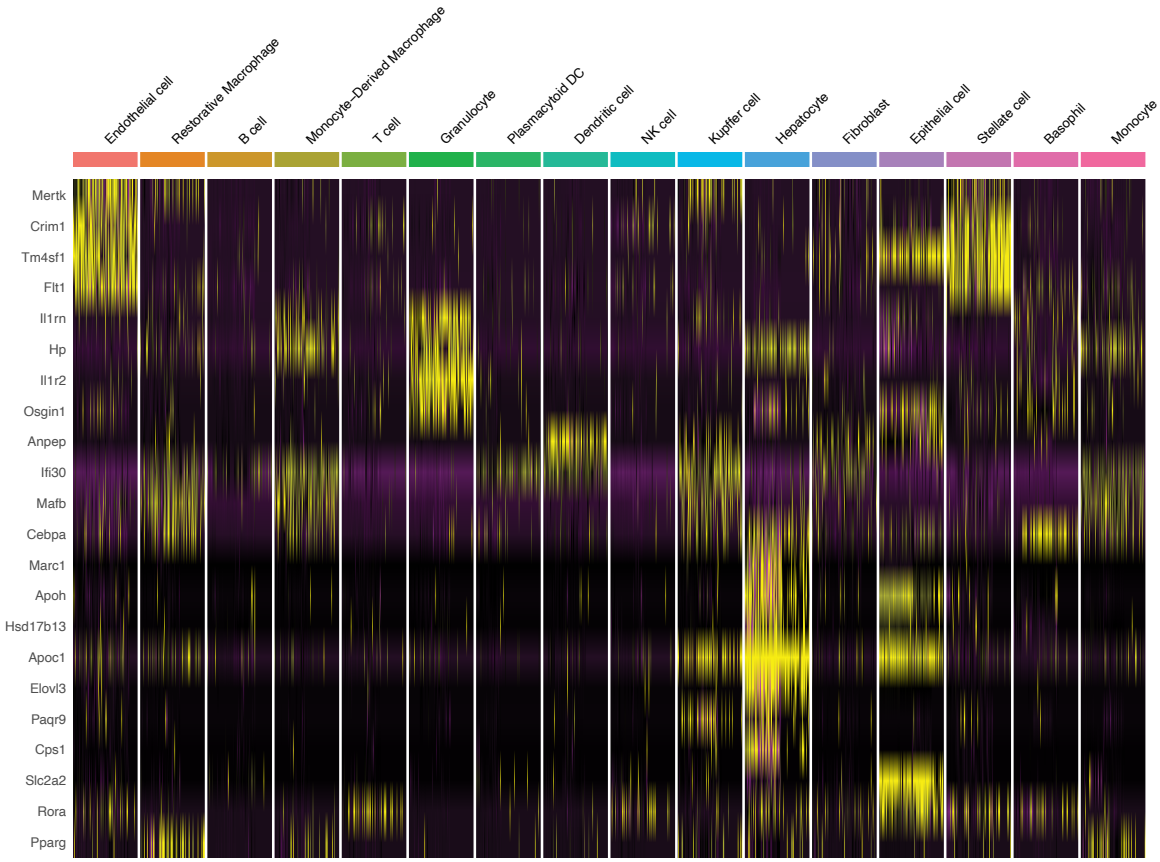

Figure 4.4 Principal component analysis of time course samples.

Principal component analysis (PCA) using the most abundant genes with an average TPM ≥ 5 across all samples. Each dot represents the average expression for a particular strain and time point. C57BL6/J mice had three samples per time point group and the 129/SvJ and BxD19/TyJ strains had 4 samples per time point group. The green dots represent 129/SvJ mice, yellow represent C57BL/6J, and red represent BxD19/TyJ. The label above each dot denotes the strain and time point in weeks. Strain abbreviations on the graph: 129 (129/SvJ), B6 (C57BL/6J), BxD (BxD19/TyJ).

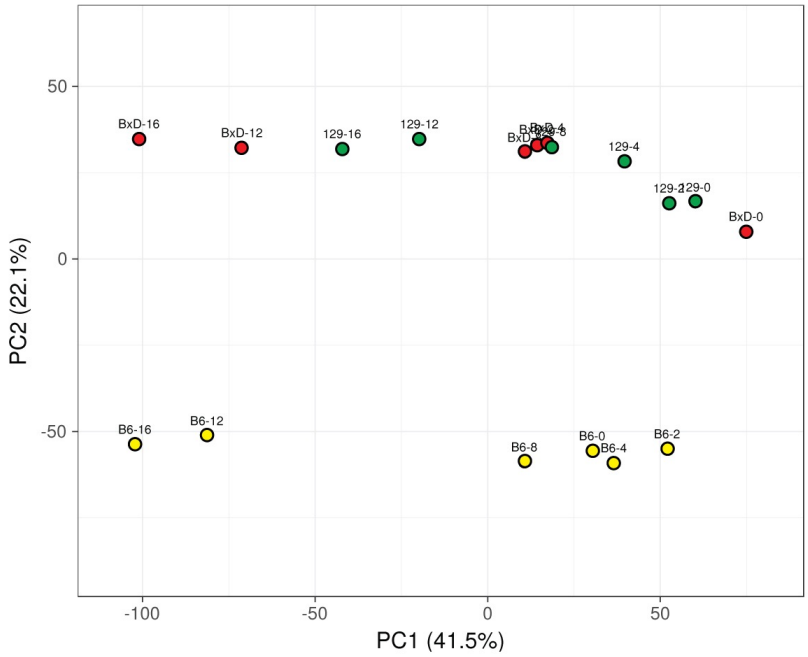

Figure 4.5 Differentially expressed genes in the NAFLD time course across 3 strains.

Heatmap depicting the expression fold change of 72 selected genes across strain and time point normalized to C57BL/6J 0 weeks (C57BL/6J 0 Week Chow = 1). The average TPM for the each group was normalized to the TPM of C57BL/6J 0 weeks. Scale bar on right represents corresponding fold change with red values representing highly induced gene expression compared to baseline. Each row is a separate gene and each column represents the normalized group average fold change.

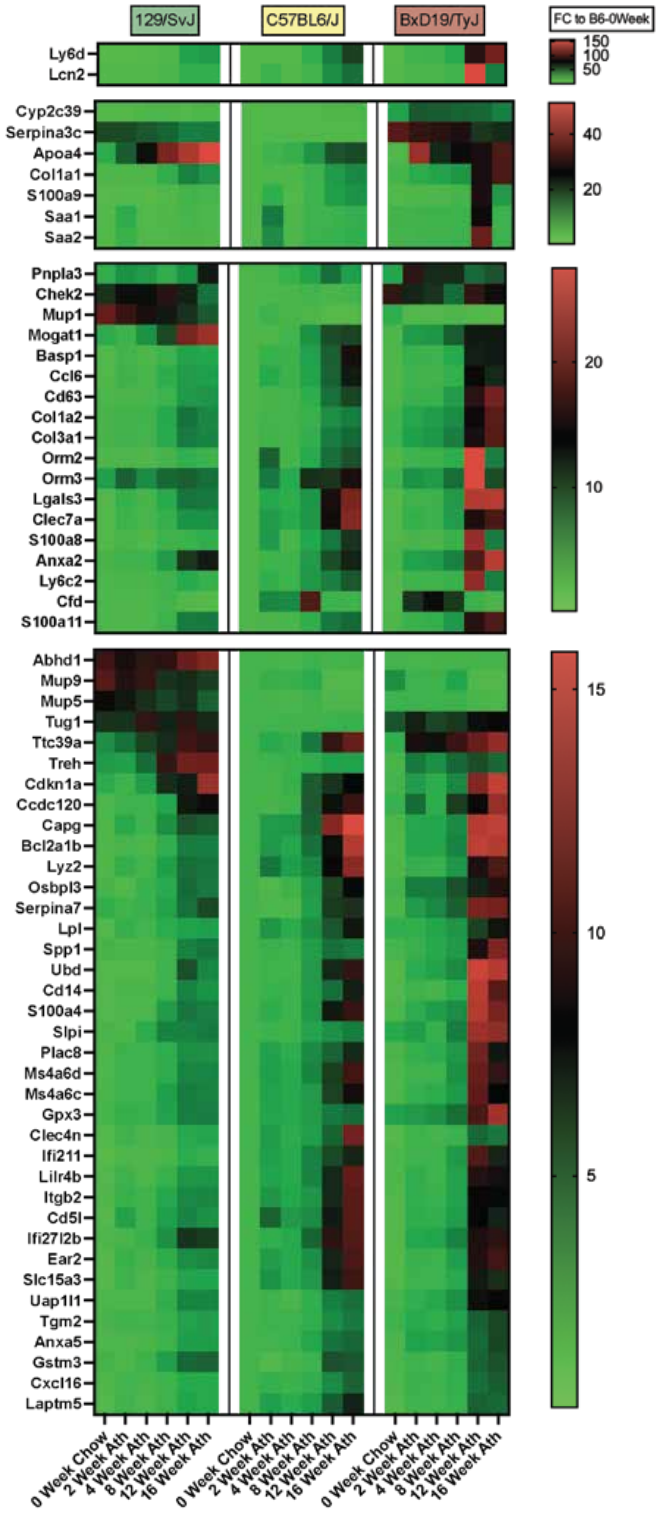
129/SvJ
C57BL6/J
BxD19/TyJ
FC to B6-0Week
150
100
50
Ly6d
Lcn2
40
20
Cyp2c39
Serpina3c
Apoa4
Col1a1
S100a9
Saa1
Saa2
20
10
Pnpla3
Chek2
Mup1
Mogat1
Basp1
Ccl6
Cd63
Col1a2
Col3a1
Orm2
Orm3
Lgals3
Clec7a
S100a8
Anxa2
Ly6c2
Cfd
S100a11
15
10
5
Abhd1
Mup9
Mup5
Tug1
Ttc39a
Treh
Cdkn1a
Ccdc120
Capg
Bcl2a1b
Lyz2
Osbpl3
Serpina7
Lpl
Spp1
Ubd
Cd14
S100a4
Slpi
Plac8
Ms4a6d
Ms4a6c
Gpx3
Clec4n
Ifi211
Lilr4b
Itgb2
Cd5l
Ifi27l2b
Ear2
Slc15a3
Uap1l1
Tgm2
Anxa5
Gstm3
Cxcl16
Laptm5
0 Week Chow
2 Week Ath
4 Week Ath
8 Week Ath
12 Week Ath
16 Week Ath

Figure 4.6 Differentially expressed time course genes in NPC populations.

We surveyed the genes identified in **Figure 4.5** for expression in the 8 and 12 week NPC single cell reference dataset. 44 out of 72 were present in the NPC dataset. Each row represents one of the 44 genes and each column represents the normalized gene expression values of 100 representative cells from that cell type.

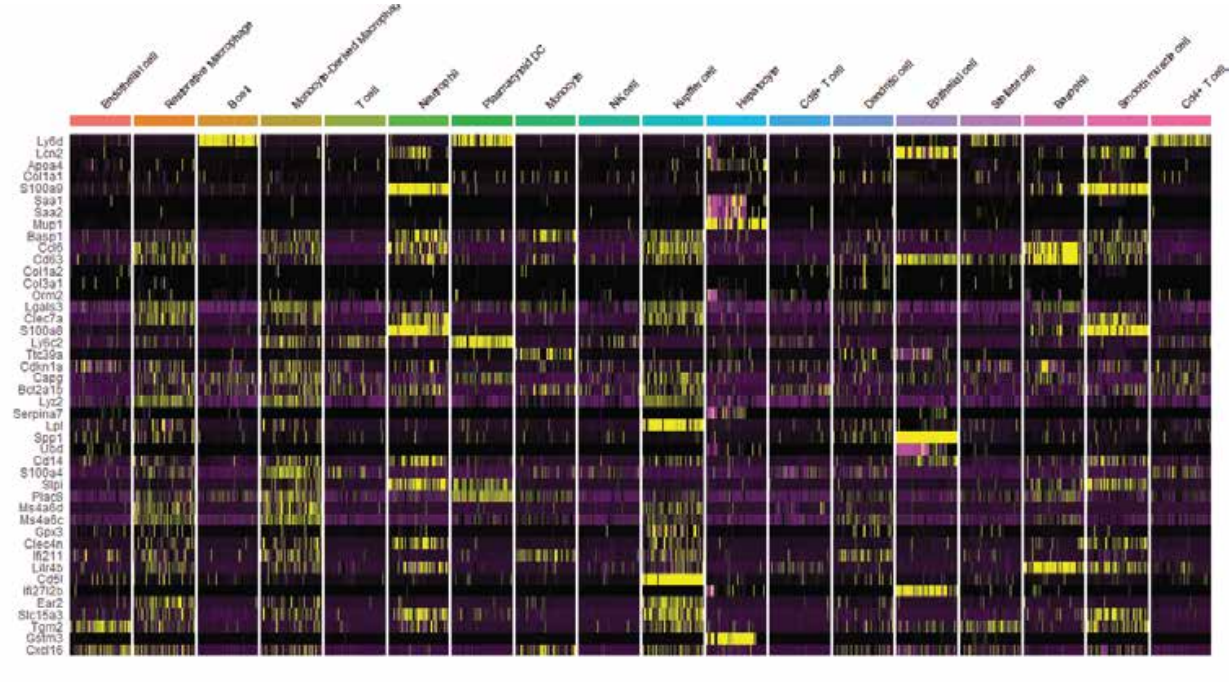

Figure 4.7 Correlations of differentially expressed time course genes with liver fibrosis in the atherosclerosis HMDP.

Sixty-three genes surveyed in **Figure 4.5** were measured in microarray analyses from liver RNA isolated from the atherosclerosis HMDP. Normalized expression values for the each of the 101 strains were correlated with average strain fibrosis area using bicorrelation from the WGCNA package. The color of the cell represents the bicorrelation coefficient between the expression value of each gene and total liver fibrosis area. * denotes a p-value $\leq$ 0.05; ** p-value $\leq$ 0.01, *** p-value $\leq$ 0.001.

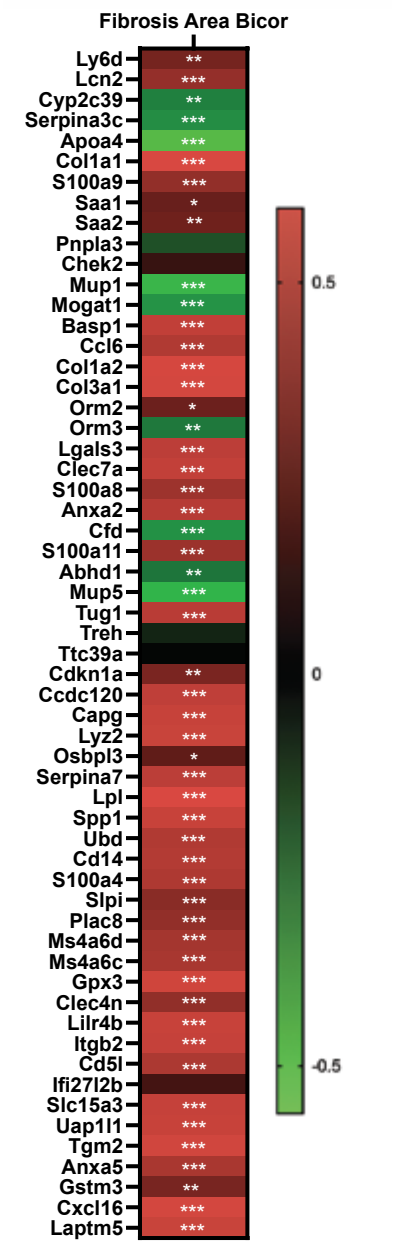
Fibrosis Area Bicor
Ly6d
Lcn2
Cyp2c39
Serpina3c
Apoa4
Col1a1
S100a9
Saa1
Saa2
Pnpla3
Chek2
Mup1
Mogat1
Basp1
Ccl6
Col1a2
Col3a1
Orm2
Orm3
Lgals3
Clec7a
S100a8
Anxa2
Cfd
S100a11
Abhd1
Mup5
Tug1
Treh
Ttc39a
Cdkn1a
Ccdc120
Capg
Lyz2
Osbpl3
Serpina7
Lpl
Spp1
Ubd
Cd14
S100a4
Slpi
Plac8
Ms4a6d
Ms4a6c
Gpx3
Clec4n
Lilr4b
Itgb2
Cd5l
Ifi27l2b
Slc15a3
Uap1l1
Tgm2
Anxa5
Gstm3
Cxcl16
Laptm5
0.5
0
-0.5

Figure 4.8 Hepatic cell type clusters identified by single-nuclei sequencing.

UMAP clustering of representative liver cell types from 0-, 8-, and 12-week nuclei across all three strains. Nuclei from whole liver were isolated from 2 animals per strain at each time point. Each dot represents a single nucleus, color coded by cell type. SMC; smooth muscle cells, EC; endothelial cell.

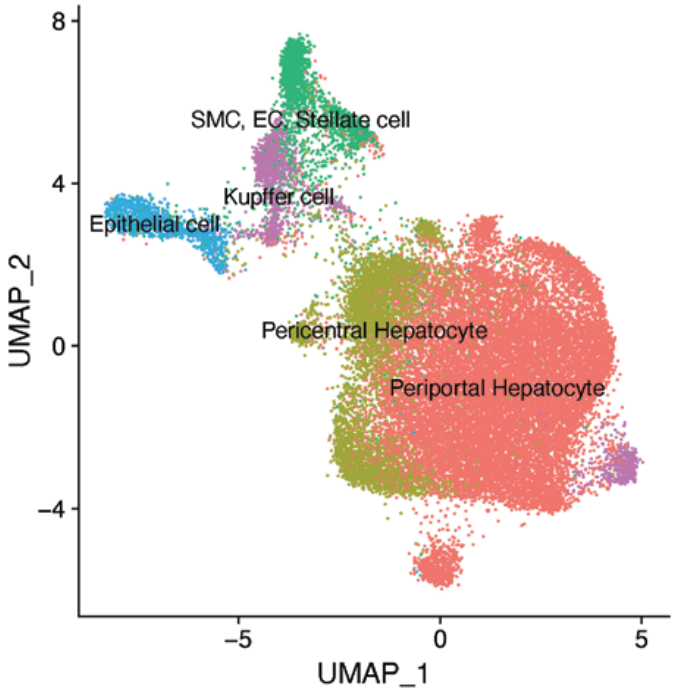

References

1. Younossi, Z. M. *et al.* The economic and clinical burden of nonalcoholic fatty liver disease in the United States and Europe. *Hepatology* **64**, 1577–1586 (2016).
2. Vernon, G., Baranova, A. & Younossi, Z. M. Systematic review: the epidemiology and natural history of non-alcoholic fatty liver disease and non-alcoholic steatohepatitis in adults. *Aliment. Pharmacol. Ther.* **34**, 274–285 (2011).
3. Moylan, C. A. *et al.* Hepatic gene expression profiles differentiate presymptomatic patients with mild versus severe nonalcoholic fatty liver disease. *Hepatology* **59**, 471–482 (2014).
4. Sanyal, A. J., Neuschwander-Tetri, B. A. & Tonascia, J. End points must be clinically meaningful for drug development in nonalcoholic fatty liver disease. *Gastroenterology* **150**, 11–13 (2016).
5. Anstee, Q. M., Daly, A. K. & Day, C. P. Genetic modifiers of non-alcoholic fatty liver disease progression. *Biochim. Biophys. Acta* **1812**, 1557–1566 (2011).
6. Day, C. P. Non-alcoholic steatohepatitis: metabolic syndrome of the liver. in *Pathogenesis and Clinical Practice in Gastroenterology* 171–185 (Springer Netherlands, 2008).
7. Schwimmer, J. B. *et al.* Heritability of nonalcoholic fatty liver disease. *Gastroenterology* **136**, 1585–1592 (2009).
8. Loomba, R. *et al.* Heritability of hepatic fibrosis and steatosis based on a prospective twin study. *Gastroenterology* **149**, 1784–1793 (2015).
9. Pirazzi, C. *et al.* Patatin-like phospholipase domain-containing 3 (PNPLA3) I148M (rs738409) affects hepatic VLDL secretion in humans and in vitro. *J. Hepatol.* **57**, 1276–1282 (2012).

10. Huang, Y., Cohen, J. C. & Hobbs, H. H. Expression and characterization of a PNPLA3 protein isoform (I148M) associated with nonalcoholic fatty liver disease. *J. Biol. Chem.* **286**, 37085–37093 (2011).
11. Dongiovanni, P. *et al.* Transmembrane 6 superfamily member 2 gene variant disentangles nonalcoholic steatohepatitis from cardiovascular disease. *Hepatology* **61**, 506–514 (2015).
12. Cefalù, A. B. *et al.* A novel APOB mutation identified by exome sequencing cosegregates with steatosis, liver cancer, and hypocholesterolemia. *Arterioscler. Thromb. Vasc. Biol.* **33**, 2021–2025 (2013).
13. Vujkovic, M. *et al.* A genome-wide association study for nonalcoholic fatty liver disease identifies novel genetic loci and trait-relevant candidate genes in the Million Veteran Program. *medRxiv* 2020–2012 (2021).
14. Hui, S. T. *et al.* The genetic architecture of diet-induced hepatic fibrosis in mice. *Hepatology* **68**, 2182–2196 (2018).
15. Godoy, P. *et al.* Recent advances in 2D and 3D in vitro systems using primary hepatocytes, alternative hepatocyte sources and non-parenchymal liver cells and their use in investigating mechanisms of hepatotoxicity, cell signaling and ADME. *Arch. Toxicol.* **87**, 1315–1530 (2013).
16. EASL–EASD–EASO Clinical Practice Guidelines for the management of non-alcoholic fatty liver disease. *J. Hepatol.* **64**, 1388–1402 (2016).
17. Schuster, S., Cabrera, D., Arrese, M. & Feldstein, A. E. Triggering and resolution of inflammation in NASH. *Nat. Rev. Gastroenterol. Hepatol.* **15**, 349–364 (2018).
18. Marra, F. & Svegliati-Baroni, G. Lipotoxicity and the gut-liver axis in NASH pathogenesis. *J. Hepatol.* **68**, 280–295 (2018).

19. Bennett, B. J. *et al.* Genetic Architecture of Atherosclerosis in Mice: A Systems Genetics Analysis of Common Inbred Strains. *PLoS Genet.* **11**, e1005711 (2015).
20. Ramachandran, P. *et al.* Resolving the fibrotic niche of human liver cirrhosis at single-cell level. *Nature* **575**, 512–518 (2019).
21. MacParland, S. A. *et al.* Single cell RNA sequencing of human liver reveals distinct intrahepatic macrophage populations. *Nat. Commun.* **9**, 4383 (2018).
22. Halpern, K. B. *et al.* Paired-cell sequencing enables spatial gene expression mapping of liver endothelial cells. *Nat. Biotechnol.* **36**, 962–970 (2018).
23. Halpern, K. B. *et al.* Single-cell spatial reconstruction reveals global division of labour in the mammalian liver. *Nature* **542**, 352–356 (2017).
24. Seidman, J. S. *et al.* Niche-specific reprogramming of epigenetic landscapes drives myeloid cell diversity in nonalcoholic steatohepatitis. *Immunity* **52**, 1057-1074.e7 (2020).
25. Trépo, E. & Valenti, L. Update on NAFLD genetics: From new variants to the clinic. *J. Hepatol.* **72**, 1196–1209 (2020).
26. Zhou, Y., Jiang, L. & Rui, L. Identification of MUP1 as a regulator for glucose and lipid metabolism in mice. *J. Biol. Chem.* **284**, 11152–11159 (2009).
27. Hui, X. *et al.* Major urinary protein-1 increases energy expenditure and improves glucose intolerance through enhancing mitochondrial function in skeletal muscle of diabetic mice. *J. Biol. Chem.* **284**, 14050–14057 (2009).
28. Lord, C. C., Thomas, G. & Brown, J. M. Mammalian alpha beta hydrolase domain (ABHD) proteins: Lipid metabolizing enzymes at the interface of cell signaling and energy metabolism. *Biochim. Biophys. Acta* **1831**, 792–802 (2013).

29. Pontén, F., Jirström, K. & Uhlen, M. The Human Protein Atlas--a tool for pathology. *J. Pathol.* **216**, 387–393 (2008).

30. Dress, R. J. *et al.* Plasmacytoid dendritic cells develop from Ly6D+ lymphoid progenitors distinct from the myeloid lineage. *Nat. Immunol.* **20**, 852–864 (2019).

31. Wang, Y.-P. *et al.* Lipocalin-2 negatively modulates the epithelial-to-mesenchymal transition in hepatocellular carcinoma through the epidermal growth factor (TGF-beta1)/Lcn2/Twist1 pathway. *Hepatology* **58**, 1349–1361 (2013).

32. Auguet, T. *et al.* Liver lipocalin 2 expression in severely obese women with non alcoholic fatty liver disease. *Exp. Clin. Endocrinol. Diabetes* **121**, 119–124 (2013).

33. Haruta, I. *et al.* Association of AIM, a novel apoptosis inhibitory factor, with hepatitis via supporting macrophage survival and enhancing phagocytotic function of macrophages. *J. Biol. Chem.* **276**, 22910–22914 (2001).

34. Enerbäck, S., Semb, H., Tavernier, J., Bjursell, G. & Olivecrona, T. Tissue-specific regulation of guinea pig lipoprotein lipase; effects of nutritional state and of tumor necrosis factor on mRNA levels in adipose tissue, heart and liver. *Gene* **64**, 97–106 (1988).

35. Kim, J. K. *et al.* Tissue-specific overexpression of lipoprotein lipase causes tissue-specific insulin resistance. *Proc. Natl. Acad. Sci. U. S. A.* **98**, 7522–7527 (2001).

36. Blencowe, M., Karunanayake, T., Wier, J., Hsu, N. & Yang, X. Network Modeling Approaches and Applications to Unravelling Non-Alcoholic Fatty Liver Disease. *Genes* **10**, (2019).

37. Kurt, Z. *et al.* Tissue-specific pathways and networks underlying sexual dimorphism in non-alcoholic fatty liver disease. *Biol. Sex Differ.* **9**, 46 (2018).

38. Chella Krishnan, K. *et al.* Integration of Multi-omics Data from Mouse Diversity Panel Highlights Mitochondrial Dysfunction in Non-alcoholic Fatty Liver Disease. *Cell Syst* **6**, 103-115.e7 (2018).

39. Parker, B. L. *et al.* An integrative systems genetic analysis of mammalian lipid metabolism. *Nature* **567**, 187–193 (2019).

40. Linke, V. *et al.* A large-scale genome–lipid association map guides lipid identification. *Nature Metabolism* **2**, 1149–1162 (2020).

41. Orešič, M. *et al.* Prediction of non-alcoholic fatty-liver disease and liver fat content by serum molecular lipids. *Diabetologia* **56**, 2266–2274 (2013).

Discussion

The Hybrid Mouse Diversity Panel (HMDP) is a systems genetics resource that was developed to investigate the genetic, epigenetic, transcriptomic, and metabolomic basis of metabolic traits like obesity, atherosclerosis, and liver disease [1]. My dissertation work investigated three different research questions related to genetic and epigenetic processes involved in obesity, atherosclerosis, and non-alcoholic fatty liver disease. Through this body of work I explored the epigenetic consequences of obesity and weight loss, the metabolic mechanisms of a novel atherosclerosis candidate gene, and the genetic mechanisms involved in the development of progressive liver disease. Together, these works inform the dynamics of disease progression in mouse models and identified future potential targets for therapeutics.

Responses to a high fat, high sucrose (HFHS) diet vary greatly among inbred strains of mice. In **Chapter 2** we sought to examine the epigenetic (DNA methylation) changes underlying these differences as well as variation in weight loss when switched to a low-fat chow diet. We surveyed DNA methylation from livers of 45 inbred mouse strains fed a HFHS diet for 8 weeks using reduced-representation bisulfite sequencing (RRBS). We observed a total of 1,045,665 CpGs of which 83 candidate sites were significantly associated with HFHS diet. Many of these CpGs correlated strongly with gene expression or clinical traits such as body fat percentage and plasma glucose. Five inbred strains were then studied in the context of weight loss to test for evidence of epigenetic "memory". The mice were first fed a HFHS diet for 6 weeks followed by a low-fat chow diet for 4 weeks. Four of the five strains returned to initial levels of body fat while one strain, A/J, retained almost 50% of the fat gained. A total of 36 of the HFHS diet responsive CpGs exhibited evidence of persistent epigenetic modifications following weight normalization, including CpGs near the genes *Scd1* and *Cdk1*. Our study identifies DNA

methylation changes in response to a HFHS diet challenge that revert more slowly than overall body fat percentage in weight loss and provides evidence for epigenetic mediated "memory".

We previously carried out a Genome-Wide Association Study (GWAS) for atherosclerotic lesions in the Hybrid Mouse Diversity Panel (HMDP), a set of 100 diverse inbred strains of mice. In **Chapter 3** we report the analysis of a candidate gene, nicotinamide N-methyltransferase gene (*Nnmt*), in a locus on mouse chromosome 9 associated with lesion size in both males and females. Antisense oligonucleotide (ASO) inhibition of *Nnmt* expression reduced median atherosclerosis lesion area by 10-fold in male and female mice on a hyperlipidemic background. This was accompanied by a decrease in proliferation and increase in apoptosis of lesional macrophages. Knockdown of NNMT also resulted in significant decreases in plasma levels of low density and very-low-density lipoprotein (LDL/VLDL) cholesterol, but these were very modest in males. Dietary supplementation of the NNMT substrate, nicotinamide (NAM), or product, N-methylnicotinamide (MNAM), did not recapitulate the protective effect of ASO treatment. Tissue-specific knockdown of *Nnmt* in liver or adipose tissues, the tissues expressing highest levels of NNMT, using shRNA and viral delivery had little or no effects on lesions or LDL/VLDL. Together, these results suggested that the primary mechanism of *Nnmt* ASO is not mediated through metabolic tissues with the highest expression of *Nnmt,* nor by changes in the circulating levels of NNMT metabolites.

Nonalcoholic fatty liver disease (NAFLD) is a complex spectrum of phenotypes that begins with fat accumulation in hepatocytes and can progress to inflammation, fibrosis, and cirrhosis. The progression of NAFLD is multi-factorial and is influenced by genetic variation, metabolic dysregulation, activation of profibrotic cell types, and tissue composition changes by the infiltration of immune cells. Previous HMDP studies in our lab identified 100-fold variation

in liver fibrosis area across 100 unique hyperlipidemic mouse strains. In **Chapter** 4 we selected a subset of strains that encompass low, moderate, and severe liver fibrosis phenotypes to monitor gene expression changes over a time course of 16 weeks. We were interested in further investigating the mechanisms that contribute to resistance or susceptibility to inflammation and fibrosis. RNA sequencing analysis of liver across six time points identified genes expression changes in susceptible strains involved in the transition from steatosis to steatohepatitis. Using single cell RNA-sequencing data generated from non-parenchymal cells, we were able to identify the relevant cell types expressing the progression-associated genes. Many of the highly upregulated genes were predominantly expressed in lymphocytes, macrophages, and neutrophils. In the HMDP study, most of the upregulated genes identified were confirmed to be positively correlated with fibrosis. We also identified protective mechanisms in the resistant strain that may attenuate fibrosis development by improving metabolic parameters in the liver through antioxidant and glucose sensitizing functions. These genes were also found to be negatively correlated with fibrosis area in the HMDP. Together these data comprise a resource of molecular and cellular changes associated with different stages of fibrosis in mice to better understand the underlying mechanisms and genetic factors.

For each topic, many follow-up questions remain. In our studies of obesity, weight loss, and NAFLD, many of the adiposity and steatosis phenotypes observed are known to be reversible. Future inquiry might ask what role does genetic variation and epigenetic memory play in the reversal of such traits? Such answers could form the basis for improved disease diagnostics and therapeutics. Regarding our studies on the candidate gene *Nnmt*, the direct mechanisms related to atherosclerosis risk remain unknown. Studies suggest that upregulation of *Nnmt* expression is reactive to metabolic dysregulation and is necessary to protect the liver and

vasculature from stress[2], but we were unable to explain why knockdown of *Nnmt* gene expression is protective against atherosclerosis. To further investigate potential mechanisms, studies of *Nnmt* knockdown must be isolated to cell types in the vasculature or lesion. In conclusion, the collection of HMDP studies from the Lusis lab represents a rich repository of data encompassing many levels of genomic and clinical measurements related to complex metabolic phenotypes from which hypotheses about diseases like obesity, atherosclerosis, and NAFLD can be tested.

References

1. Ghazalpour, A. *et al.* Hybrid mouse diversity panel: a panel of inbred mouse strains suitable for analysis of complex genetic traits. *Mamm. Genome* **23**, 680–692 (2012).
2. Campagna, R. *et al.* Nicotinamide N-methyltransferase in endothelium protects against oxidant stress-induced endothelial injury. *Biochim. Biophys. Acta Mol. Cell Res.* **1868**, 119082 (2021).